Theses

9-18-2006

Thin/cambered/reflexed airfoil development for micro-air vehicles at Reynolds numbers of 60,000 to 150,000

Michael Reid

Follow this and additional works at: https://repository.rit.edu/theses

THIN/CAMBERED/REFLEXED AIRFOIL DEVELOPMENT FOR MICRO-AIR VEHICLES AT REYNOLDS NUMBERS OF 60,000 TO 150,000

By

MICHAEL R. REID

A Thesis Submitted in Partial Fulfillment of the Requirement

for Master of Science in Mechanical Engineering

Approved by:

Department of Mechanical Engineering Committee

Dr. Jeffery Kozak – Thesis Advisor   _____

Dr. Agamemnon Crassidis   _____

Dr. Kevin Kochersberger   _____

Dr. Edward Hensel – Dept. Representative   _____

Rochester Institute of Technology

Rochester, New York 14623

September 2006

PERMISSION TO REPRODUCE THE THESIS

Title of Thesis

THIN/CAMBERED/REFLEXED AIRFOIL DEVELOPMENT FOR MICRO-AIR VEHICLES AT REYNOLDS NUMBERS OF 60,000 TO 150,000

September 2006

ABSTRACT

Previous micro-air vehicle research has addressed thin/cambered/reflexed airfoils on an application specific basis, relying heavily on the shape characteristics of previously designed airfoils. The motivation of the current research is to determine the relationship that exists between thin/cambered/reflexed airfoil performance and the defining airfoil shape parameters to improve future airfoil designs. An emphasis is placed on the effect each airfoil shape parameter has on the overall airfoil performance and the effect of the interdependence of each shape parameter. Maximum coefficient of lift, stall angle of attack, maximum coefficient of lift/coefficient of drag and the angle of attack at which it occurs are found for a variety of thin/cambered/reflexed airfoils and a number of correlations between changes in shape parameters and airfoil performance are established. Changes in C and xC cause a 40% variation of $C_{l,max}$ and 40% variation of α_{stall}. Changes in R and xR cause a 15% variation of $C_{l,max}$ with no significant variation in α_{stall}. Changes in C and xC cause a 30% variation of $C_l/C_{d,max}$ and 50% variation of $\alpha_{Cl/Cd,max}$. Changes in R and xR cause a 20% variation of $C_l/C_{d,max}$. Airfoil performance is determined using XFOIL, a two dimensional analysis code designed specifically to address airfoil boundary layer behavior at low Reynolds numbers. A comparison of XFOIL results and known wind tunnel data is presented as validation of the analysis code in addition to previously published validation studies. Wind tunnel testing performed in Rochester Institute of Technology's closed circuit low speed wind tunnel is presented for a small subset of the airfoils analyzed as a comparison of the experimental and analytic boundary layer behavior. The results showed good correlation between XFOIL predictions and wind tunnel results for Bezier airfoils with camber less than 7%.

ACKNOWLEDGEMENTS

I would like to thank my advisor Dr. Jeffery Kozak, whose laissez faire approach combined with timely interjections of personal wisdom proved invaluable. I would also like to thank the mechanical engineering faculty, who are undoubtedly responsible for what I have been able to achieve.

I would like to thank my Mother, Father, and Sister who have provided nothing but love and encouragement; they helped me maintain a positive attitude, and my sanity, throughout the entire process.

TABLE OF CONTENS

LIST OF FIGURES

NOMENCLATURE

MAV	Micro-Air Vehicle
UAV	Unmanned Air Vehicle
DARPA	Defense Advanced Research Projects Agency
UIUC	University of Illinois at Urbana Champagne
NACA	National Advisory Committee for Aeronautics
LTPT	Low Turbulence Pressure Tunnel
MCL	Mean Camber Line
ILE	Instrument Limit of Error
Re	Reynolds Number
M	Mach Number
Tu	Free-stream Turbulence Level
α	Angle of Attack
α_{stall}	Stall Angle of Attack
$\alpha_{Cl/Cd,max}$	Angle of Attack of $C_l/C_{d,max}$
C_l	2D Coefficient of Lift
$C_{l,max}$	Maximum 2D Coefficient of Lift
C_d	2D Coefficient of Drag
C_l/C_d	2D Coefficient of Lift / Coefficient of Drag
$C_l/C_{d,max}$	Maximum 2D Coefficient of Lift / Coefficient of Drag
$C_{m,\alpha}$	Pitching Moment Slope
$C_{m,0}$	Pitching Moment Intercept
C_L	3D Coefficient of Lift
C_D	3D Coefficient of Drag
C_M	3D Pitch Moment Coefficient
L/D	3D Lift/Drag
C_f	Skin Friction Coefficient
$C_{d,p}$	Pressure Drag Coefficient
C_p	Pressure Coefficient
$C_{p,inc}$	Incompressible Coefficient of Pressure

H	Boundary Layer Shape Parameter
x_s	Separation Location
x_{tr}	Transition Location
x_r	Reattachment Location
c	Chord
T	Thickness
C	Max Camber
xC	Location of Max Camber
R	Max Reflex
xR	Location of Max Reflex
AR	Aspect Ratio
N	Number of Panels
P	Panel Bunching Parameter
t	Trailing Edge/Leading Edge Panel Density Ratio
TEgap	Trailing Edge Gap
Ncrit	Critical Amplification Ratio
$X_{tr,upper}$	Upper Surface Forced Transition location
$X_{tr,lower}$	Lower Surface Forced Transition location
Vacc	Viscous Solution Acceleration Parameter
iter	Iteration Limit
init	Boundary Layer Initialization Parameter
V_{cor}	Corrected Velocity
V_{ind}	Indicated Velocity
P_0	Standard Pressure
P_a	Atmospheric Pressure

Subscripts

max	Maximum
upper	Upper Airfoil Surface
lower	Lower Airfoil Surface

1 Introduction

The first section of this chapter provides background and motivation for the research presented. The second section covers previous relevant work done in the field of Micro Air Vehicle (MAV) airfoil design, development, and testing. The final section addresses the objectives of the present work.

1.1 Background and Motivation

In 1996 the Defense Advanced Research Projects Agency (DARPA) suggested a program initiative for the development and testing of MAVs. The primary goal of the program was to mature technology required for flight capable vehicles less than 0.15m in maximum linear dimension. It was the intent that these vehicles could perform over-the-hill reconnaissance missions to improve battlefield situational awareness (Mueller 2003). The program came at a time when larger unmanned air vehicles (UAV) were performing a growing role in military surveillance and reconnaissance. It was determined at that time that technology had advance to a point where aircraft on the order of 0.15m were becoming feasible.

Aircraft that are designed to meet the 0.15m requirement operate at chord Reynolds numbers (Re) below 500,000 and suffer from poor aerodynamic performance characteristics (Mueller 2003). Airfoils operating in the Re number range from 70,000 to 200,000, which represents many MAV airfoils, experience negative aerodynamic performance properties if not designed properly (Mueller 2003). Initially very little research had been done for aircraft operating at such low Re numbers, and aircraft designers turn to traditional airfoils for MAV applications. Although the airfoils were operating at off-design conditions, the large size of first generation MAV designs tolerated non-optimal airfoil performance. However, for future MAV's it was clear that more optimal airfoil operation would be required to achieve the size requirement set by DARPA.

As the field of MAVs advanced, second generation airfoils utilized work done my R. Eppler and M. Drela and their low Reynolds number airfoils design and analysis codes, Eppler code and XFOIL respectively (Mueller 2003). MAV design still suffered from the limitations of the electronic components and power systems of the time and overall system size was relatively large. The large size resulted in aircraft that operated in the upper range of what is generally considered low Re numbers, which limited the negative effects on performance.

The past five years of MAV development has seen a rapid decline in maximum size due to advancements in the electronic component and power system size and weight. This trend has increased the need for a specifically designed MAV airfoil. The progression of previous MAV airfoils suggested that thin/cambered airfoils would achieve good low Re number performance (Null, Shkarayev 2004; Pelletier, Mueller 2000). In addition, the increasing implementation of composite materials has allowed for very thin wings to become structurally feasible. In parallel with thin wing development, a new aircraft control architecture relying on morphable structures instead of mechanical links has been developed; a concept that is easily implemented into a thin wing MAV (Shkarayev, Jouse, Null, Wagner 2003; Levin, Shyy 2001).

Adaptable airfoils and morphable surfaces are areas of current MAV research and would benefit from information regarding the performance of various different thin airfoil shapes. Currently, only maximum camber has been addressed as a potential variable airfoil shape parameter but questions still remain such as; how much change in camber is required? How much change is too much? Should the location of max camber change as well? These are the types of questions answered by the survey of a wide variety of airfoil shapes presented in this thesis.

MAV technology has developed to the point where the 0.15m requirement has been achieved, however in a very limited scope. For MAV's to serve their intended purpose, the useable flight envelope must be expanded. For this to occur a detailed understanding of a wide range of airfoil shape characteristics must be achieved. The lack of a vast selection of MAV airfoils with varying performance characteristics is the motivation behind this research.

1.2 Previous Research

This section addresses relevant previous research done in the field of low Re number aerodynamics as it applies to MAV airfoil development. The first section discusses the phenomena of laminar separation bubble formation and behavior. The second section focuses on thin/cambered airfoils specifically. The final section covers methods for improving the performance of MAV airfoils. Methods for experimental testing and validation are addressed when appropriate in each section.

1.2.1 Laminar Separation Bubble Mechanics

As aircraft size decreases, chord Re number decreases; if the Re number drops below 500,000 formation of a laminar separation bubble is possible (Mueller 2003). At Re numbers below 200,000 laminar separation bubble formation becomes an important factor in the generation of lift and drag (Mueller 2003). Below 70,000, airfoil boundary layer behavior is dominated by laminar separation bubble effects (Gad-El-Hak 1989). At the critical Re number, the length of the laminar separation region is anticipated to be on the order of one chord length (Mueller 2003). A general rule was developed by Carmichael (1981) that stated the critical Re number based on the characteristic length, defined from separation to reattachment, and freestream velocity was around 50,000. Using Carmichael's rule, Gad-El-Hak (1989) made the observation that airfoils operating at a chord Re number less than 50,000 will not achieve reattachment after laminar separation. Aircraft designed to meet DARPA's 0.15m size requirement generally operate below a Re number of 200,000 and are subject to laminar separation bubble effects (Gad-El-Hak 1989). Understanding laminar separation bubble mechanics is important to explaining airfoils performance at low Re numbers.

1.2.1.1 Formation, Classification, and Effects

At low Re numbers the boundary layer on the forward section of an airfoil is highly laminar (Gad-El-Hak 1989). When the Re number drops below 500,000 the laminar boundary layer lacks the flow momentum to overcome the adverse pressure gradient on the aft section of the airfoil and separates. In general, a laminar boundary layer suffers from separation due to an inability to traverse adverse pressure gradients because of a lack of flow momentum. The separated boundary layer forms a free shear layer which is highly unstable. Transition of the laminar free shear layer to turbulent flow is caused by amplification of the Kelvin-Helmholtz vorticity, also known as inviscid instabilities, along the length of the separated region (Yarusevych, Sullivan, Kawall 2005). Reattachment of the turbulent boundary layer then becomes dependent on the energy carried into the near wall region, which prevents dissipation of the recirculating zone (Gad-El-Hak 1989). If sufficient vortex strength is achieved in the near wall region, the boundary layer is able to reattach to the airfoil surface. A detailed diagram of a laminar separation bubble, provided by Gad-El-Hak (1989), is shown in Figure 1.1.
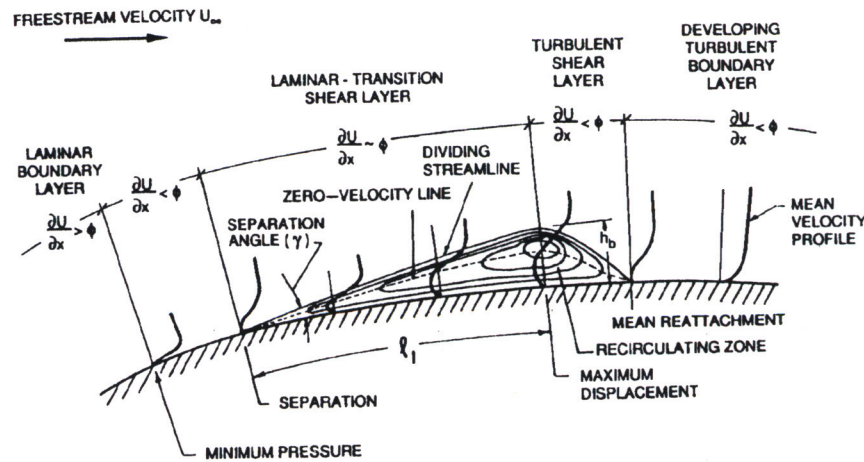
Figure 1.1: Laminar Separation Bubble (courtesy of Gad-El-Hak)

Laminar separation bubble size is directly dependent of Reynolds number. For Re numbers slightly above 50,000 a bubble that spans a majority of the chord is anticipated, with the

length of the bubble decreasing as Re number increases (Gad-El-Hak 1989). A laminar separation bubble that covers between 15-40% of the airfoil surface is referred to as a *long* bubble (Mueller 2003). *Short* bubble classification defines a bubble that is less than 15% chord. For short bubbles, the fraction of the bubble that is laminar is between 0.60 and 0.85 (Schmidt, Mueller 1989). In some cases there is an additional classification made for a laminar separation bubble that cover less than 2% of the airfoil chord, called a transition bubble. They act primarily as a laminar to turbulent trip (Brendel, Mueller 2003). Transition bubbles generally occur at Re numbers above 300,000 and are not associated with either separation bubbles that change size and location or bubbles that are present over a wide range of angle of attack (Brendel, Mueller 2003). Gad-El-Hak (1989) provides an alternate criterion for the long/short laminar separation bubble classification based on the boundary layer Re number defined by the local displacement thickness and velocity just outside the core recirculating region of flow. Boundary layer Re numbers greater than 500 signify a short bubble and less than 500 represent a long bubble (Gad-El-Hak 1989).

The long/short laminar separation bubble classification is important because each results in fundamentally different airfoil performance characteristics. Airfoils that have short bubbles are able to achieve higher lift to drag ratios (Gad-El-Hak 1989). In addition, short bubbles reduce in size and move towards the leading edge with increasing angle of attack. When the stall angle of attack is reached the short bubbles burst at the leading edge resulting in a stall behavior similar to thin airfoil stall (Gad-El-Hak 1989; Mueller 2003). Leading edge stall that results from the bursting of a short bubble is an irreversible process. Airfoils that experience leading edge stall exhibit strong hysteresis when returned to a smaller angle of attack due to the inability of the short leading edge bubble to reform. (Gad-El-Hak 1989; Boreren, Bragg 2001). In addition, leading edge stall is known to result in oscillations between periods of attached and separated flow (Greenblatt, Wygnanski 2003). The behavior of the short bubble over the operating range of angle of attack results in a linear coefficient of lift (C_l) vs. angle of attack (α) plot with the exception of a small bump that appears due to the presence of the short bubble at lower angles of attack (Gad-El-Hak 1989). Airfoils that exhibit long bubbles suffer from poor lift to drag ratios. When long bubbles are present an increase in angle of attack enlarges the bubble, which extends both upstream and downstream

(Gad-El-Hak 1989; Mueller 2003). When a long bubble extends to the trailing edge of an airfoil, stall occurs. This boundary layer behavior results in a less severe stall than in the leading edge/short bubble bursting scenario.

The increase in drag due to the presence of a laminar separation bubble, called *bubble drag*, is important in understanding the total airfoil drag performance at low Re numbers. Drag force acting on an airfoil comes from two sources; skin friction and pressure drag, which includes flow separation, and boundary layer displacement effects (Gad-El-Hak 1989). Bubble drag contributes significantly to pressure drag, specifically boundary layer displacement effects. There is also an increase in skin friction aft of the bubble due to the transition of the boundary layer; however this effect is much less than the pressure drag effects. The exact contribution of bubble drag to the total drag of an airfoil is difficult to measure, however Gopalarathnam suggests a method utilizing the shape of the chord-wise transition location (x_{tr}) vs. C_l graph, called a *transition curve* (Gopalarathnam, Broughton, McGranahan, Selig 2001). If the transition curve is shallow, meaning the transition point moves drastically with changes in C_l, the airfoil is operating with low bubble drag. This also means that the range of low bubble drag operation is shorter due to the limited range of transition location (0-1). If the transition curve is steep the bubble drag is relatively high (Gopalarathnam, et al. 2001).

The presence of a laminar separation bubble not only increases the drag of a particular airfoils but it also degrades lift generation. The effect of a short laminar separation bubble on lift generation is minimal because it only slightly diminishes the upper surface peak pressure attained by an airfoil (Gad-El-Hak 1989). For a long bubble, the region where peak pressure would normally occur is replaced by a short region of constant pressure much lower than peak pressure, resulting in a large reduction in lift. The length and location of the constant pressure region coincides with the region occupied by the laminar separation bubble. The pressure distributions for a short and long laminar separation bubble cases can be seen in Figure 1.2: Laminar Separation Bubble Pressure Distribution (courtesy of Gad-El-Hak).
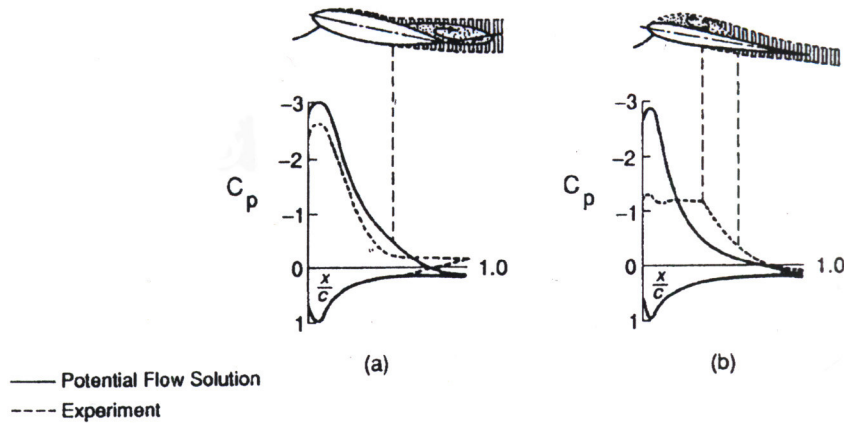
Figure 1.2: Laminar Separation Bubble Pressure Distribution (courtesy of Gad-El-Hak)

1.2.1.2 Determining Location

Determining the exact location of a laminar separation bubble is critical in understanding the behavior of different airfoils at low Reynolds numbers. There are many different methods and tools available for finding the boundary layer separation and reattachment points that define a laminar separation bubble. Experimental methods are primarily based on boundary layer visualization utilizing surface oil flow methods or the introduction of *marker* particles in the flow to make it easier to see the boundary layer mechanics. In addition, experimental devices such as hot-wire anemometers and local pressure sensors are able to measure boundary layer parameters which can then be used to resolve the location of laminar separation and reattachment. Determining laminar separation bubble location analytically is much more challenging and requires a detailed computational scheme. More details about one particular numerical solver, XFOIL, are provided in Section 1.2.4.

Utilizing an experimental study performed by Brendel and Mueller (2003), a description of the techniques used to determine the location of separation and reattachment is presented. For this particular study, smoke and hot-wire anemometer measurements were taken at a number of chordwise points along an airfoil. The smoke was created by injecting the boundary layer with titanium tetrachloride which turns into a white vapor when mixed with

7

air. The airfoil was placed between 2 splitter plates to better simulate 2D flow. Results of the boundary layer velocity profiles from both the hot-wire and smoke visualization results were used to determine where separation and reattachment occurred. By finding where lines of constant velocity in the laminar region of the separation bubble intersected the surface, a determination of the points of separation and reattachment was made.

Surface oil flow provides an additional method for determining boundary layer separation and reattachment location through insight on how the skin friction coefficient (C_f) changes along the airfoil surface. In a study conducted at The University of Illinois at Urbana-Champaign (UIUC) wind tunnel, Lyon, Selig, and Broeren (1997) utilized surface oil flow visualization to find the separation and reattachment points on various airfoils. A light oil was combine with florescent pigment and airbrushed onto the wing's surface before being mounted in the wind tunnel. The wind tunnel was run for 30 to 45 minuets with the airfoil at a constant angle of attack, at which time obvious surface oil features were visible. The point of laminar separation is characterized by a subtle change is surface oil texture. The region occupied by the laminar separation bubble is distinguished by low near surface velocities and reversed flow resulting in a small negative C_f value. This results in very little change to the surface texture for the region throughout the duration of the test.   The location of reattachment is determined from an oil accumulation line. The oil accumulation line occurs just upstream of reattachment where there is a local spike in C_f which results in the accretion of oil. An image of the surface oil flow results, showing separation, oil accumulation, and reattachment is presented in Figure 1.3.
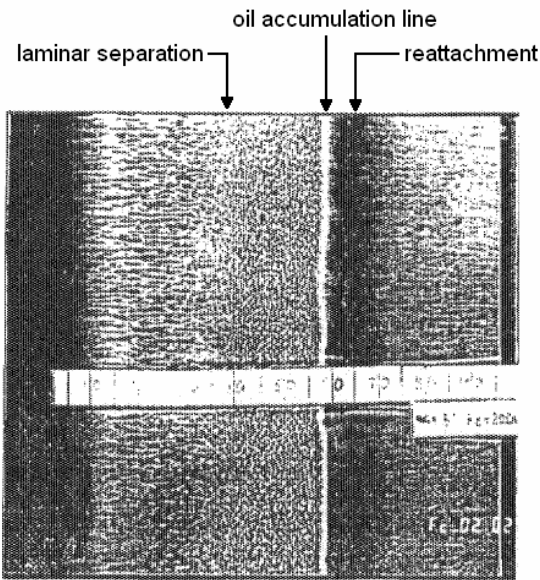
Figure 1.3: Surface Oil Flow – Example (courtesy of Lyon)

1.2.2   Airfoils at Low Reynolds Numbers

There are a number of studies that investigate the performance of airfoils at low Re numbers. Some utilize traditional airfoils, such as the NACA 4-digit series, and some utilize airfoils specifically designed or modified for low Re applications. The vast amount of data available on NACA airfoils make them ideal for initial testing and comparison studies. The field of MAV airfoil design has developed in such a way that a number of empirical characteristics for good performing low Re number airfoils have been determined. The results of those studies will be presented in the following sections as a partial survey of past and current low Re number airfoil research.

1.2.2.1 NACA 4-Digit Airfoils

An experimental study, performed by Yarusevych et al. (2001), investigated the boundary layer behavior of a NACA 0025 airfoil at Re numbers of 150,000 and 100,000. Boundary

layer separation, transition, and reattachment location was determined using upper surface pressure distribution data.   A comparison of the experimental and theoretical pressure distributions shows a substantial decrease in lift due to boundary layer separation. At Re = 150,000 a region of constant pressure signifying the presence of a laminar separation bubble is present at 0°, 5°, and 10° angle of attack. At 0° the region of constant pressure extends over 30% of the airfoil starting at mid chord. As angle of attack increases to 5° then 10° as the bubble moves upstream and decreases in size. For 5° and 10° angle of attack the location of the laminar separation bubble affects the peak suction point of the airfoil, significantly reducing lift generation. For Re = 100,000, laminar separation occurs at all 3 angles of attack resulting in large reductions of lift and increased drag. The conclusion of this study was that thick (25% chord) NACA airfoils are poor low Re number performers.

1.2.2.2 Characteristics of Low Reynolds Number Airfoils

It has been found that airfoils operating at low Re numbers benefit from reduced maximum thickness (Null, Shkarayev 2004). A comparison study of a 0.2% thickness airfoil defined by the upper surface of an S5010 airfoil to the original 10% thickness S5010 airfoil showed the thinner version achieved twice the $C_{L,max}$ as the original at a Re number of 50,000. In a separate study comparing a GOE417A airfoil with 3% thickness and a N60 airfoil with 12% thickness, the GOE417A was found to have higher lift to drag ratios (Kellogg 2004). Additionally, in a study of the Pfenninger 048 airfoil and the Eppler 61 airfoil with 4.8% and 5.63% thickness respectively the thicker Eppler airfoil was found to out perform the thinner airfoil above Re = 90,000 and the thinner Pfenninger out performed the Eppler below Re = 90,000 (Mueller 1999). An additional study show this trend continued as Re number dropped to 20,000. A comparison was also made between an S1223 airfoil with a maximum thickness of 12% and a modified S1223 with the same mean camber line but with only 6% camber. The comparison showed that the thinner airfoil was 27% more efficient than the thicker airfoil between Re = 75,000 and 300,000 (Kellogg 2004). Also, a study comparing five airfoils of varying max camber, thickness, and leading edge curvature showed that the best thin airfoil outperformed the best thick airfoil by 22% for turbulent conditions and 9%

for laminar conditions. These studies showed that thinner airfoils outperform their thicker counterparts at low Re number.

The performance of low Re number airfoils relies heavily on maximum camber. In a study performed by Null and Shkarayev (2004) a cambered plate wing design utilizing an airfoil shape defined by the top surface of an S5010 airfoil. The wing was tested at four different camber values, 3%, 6%, 9%, and 12% chord (Null, Shkarayev 2004). Re numbers of 50,000, 75,000, and 100,000 were all tested to evaluate the 3D coefficient of lift (C_L), coefficient of drag (C_D), moment coefficient (C_M), and lift to drag ratio (L/D). Unlike previously discussed studies, the test was not performed on a uniform span model separated in the wind tunnel by splitter plates to simulate 2D flow; tests were performed on a model with a circular planform and subject to large 3D tip vortex structures. The results showed that the 3% cambered wing outperformed all others in L/D, surpassing the 6% camber airfoil by 25%. The angle of attack for max L/D for the 3% camber wing was 5°. For C_L, the 3% camber airfoil shows no typical stall point. The 6%, 9%, and 12% camber airfoils show stall behavior, with the 12% having the least drastic post stall drop in C_L. The 6% camber airfoil attained the highest C_L of 1.4 at an angle of attack of 27°. Though 3D in nature the wing performance at different camber values provides insight into the 2D airfoil performance.

Thin/cambered plate airfoils do not resemble traditional airfoils; they usually have a constant thickness less than 2% chord and take their mean camber line form a traditional airfoil. In a study by Pelletier and Mueller (2000), a cambered plate airfoil with constant thickness of 1.75% cord and 4% camber following a circular mean camber line was tested and compared to a flat plate airfoil. Results for lift and drag were presented at Re = 60,000 and 140,000. The cambered plate airfoil was shown to achieve a higher coefficient of lift/coefficient (C_l/C_d) of drag than the flat plate model. C_l was reported to behave less linear at low angle of attack than the flat plate.

In a similar study Jenkins et al. (1998) tested six thin (1.5% chord) circular cambered plate airfoils with camber values ranging from 0% to 10% chord in 2% chord increments.   All airfoils were tested at Re numbers ranging from 74,000 to 100,000. The 2% camber airfoil

showed very little stall hysteresis at all Re numbers where the 4% camber show stall behavior only for higher Re numbers. Both 8% and 10% showed strong non-linearity at low angle of attack, with 10% showing a drastic increase in slope around 8%. It was found that as camber increased the maximum coefficient of lift ($C_{l,max}$) increased.

Trailing edge and leading edge geometry has been shown to have little effect on thin cambered plate wings (Pelletier, Mueller 2000). A number of testes were performed for thin airfoils with sharp, rounded, and elliptical leading and trailing edges geometries with no significant difference in lift or drag performance.

1.2.3   Methods for Improved Low Reynolds Number Performance

A number of attempts have been made to improve airfoil performance at low Reynolds numbers. Most methods involve forcing premature boundary layer transition in order to eliminate laminar separation. This concept is derived from the performance characteristics of airfoils with rough surface texture at low Re numbers. In Figure 1.4, as presented by Gad-El Hak (1989), rough airfoils begin to out perform smooth airfoils as Re number decreases below 100,000. Additional methods utilize adaptive materials that change shape to reduce the size of laminar separation bubbles. Further methods for boundary layer control, such as boundary layer suction, are not presented because of the difficulty in implementing such technology on the scale of an MAV. A number of experiments are presented that outline the benefits of each improvement method.
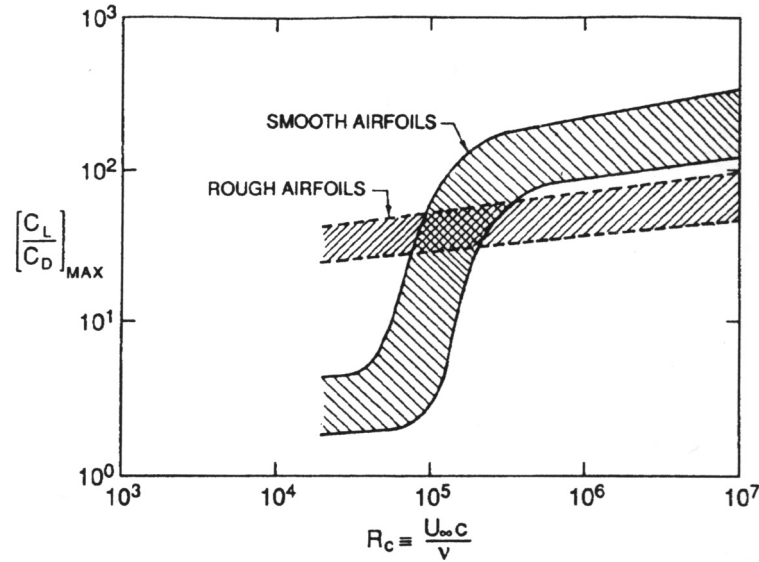
Figure 1.4: Effect of Surface Roughness (courtesy of Gad-El Hak)

A boundary layer trip is a device placed forward of the laminar separation point on an airfoil to cause the boundary layer to transition to turbulent flow. The turbulent flow, which is more resistant to separation, results in better airfoil performance (Gad-El-Hak 1989). The effect of the boundary layer trip is to reduce the overall drag by significantly reducing the bubble drag associated with a long laminar separation bubble while incurring only a slight device drag penalty (Lyon, et al. 1997). In the case of a small bubble, the drag reduction due to the elimination of the bubble and the drag addition from device drag are of the same magnitude making performance improvement negligible. This concept is illustrated in Figure 1.5 from Lyon et al (1997). The design of a boundary layer trip is difficult because it depends highly on the Re number, airfoil, and angle of attack. Boundary layer trip design is important because off design operation causes significant increases in drag. In order to determine trip effectiveness, a number of trip configurations and locations were tested at various Reynolds numbers. The conclusions were that relatively small trips produced large drag reduction, as long as the trip was before separation, and multiple trips and complex 3D trips showed no advantage over simple 2D trips (Lyon, et al. 1997). Most importantly, boundary layer trips were unable to achieve drag performance equal or better than a good designed un-tripped airfoil with no laminar separation bubble.

13
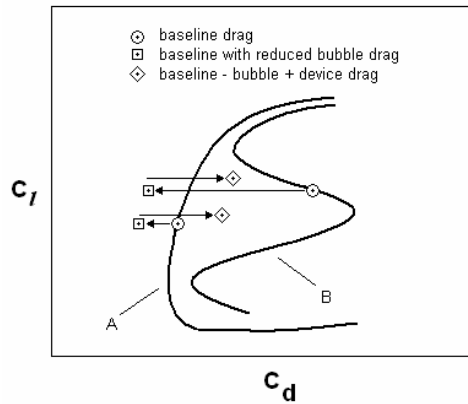
Figure 1.5: Drag Comparison of Tripped and Un-tripped Airfoils (courtesy of Lyon)

Membrane wings, also identified as adaptive wings, are designed to change shape in a predictable way in order to improve airfoil performance (Levin, Shyy 2001). Airfoils that deform during flight can also substantially improve lift and drag characteristics in unsteady flight conditions. Analysis done by Levin and Shyy (2001) utilized a CLARK-Y airfoil modeled with a massless, zero thickness membrane as an upper surface. Analysis was done using a version of XFOIL modified to allow for surface changes based on pressure distribution, local shear stress and membrane tension. Results showed that the maximum coefficient of lift ($C_{l,max}$) for the rigid and membrane airfoils were very similar. The membrane wing did prove to be less sensitive to fluctuations in Re number and had a higher average $C_{l,max}$ in unsteady conditions.

1.2.4 XFOIL

Numerical simulation of low Re number flow is very difficult due to the strong interaction of the boundary layer effects. XFOIL was developed by Mark Drela at MIT to address the problems associated with the viscous boundary layer interactions (Drela, Giles 1987; Drela 1987). The primary goal of the computational scheme was to accurately predict laminar and turbulent separated flows in order to precisely model laminar separation bubble behavior. Also an accurate transition prediction method was implemented to achieve reliable

14

reattachment location, bubble size, and associated losses (Drela, Giles 1987; Drela 1987). The feature that allows XFOIL to quickly and accurately predict low Re number flows is the simultaneous application of the global Newton-Raphson method to the coupled viscous-inviscid formulation. XFOIL has two major modes of operation, analysis and mixed inverse design. Mixed inverse design mode takes a user prescribed pressure distribution and builds an airfoil geometry that will most closely match it. This feature is of no use in the current research project and is not described in detail. The analysis mode employs user defined airfoil coordinates and solves for various boundary layer and airfoil characteristics. The analysis mode is the primary mode of operation for the current research project.

1.2.4.1 Boundary Conditions

XFOIL requires a number of boundary conditions to ensure a well posed numerical problem. In analysis mode, the airfoil surface is the defining location of the initial streamline; as the simulation progresses the surface streamline is adjusted according to the local boundary layer displacement thickness (Drela, Giles 1987; Drela 1987). The stagnation point is allowed to assume any position on the airfoil's surface so that the pressure is equal on either side (Drela 1987). The same is true with the stagnation streamline position. In the case of separated flow the stagnation streamlines aft of the airfoil are separated by the thickness of the wake displacement. The far-field boundary conditions are defined by a freestream pressure, vortex, source, and doublet. The vortex strength is derived from the Kutta-condition, the source strength from any viscous wakes, and the doublet strength from the requirement to minimize the discrete streamlines deviation from the analytic velocity potential (Drela 1987).

1.2.4.2 Transition Prediction

XFOIL uses spatial-amplification theory, derived from the Orr-Sommerfeld equation to predict laminar to turbulent transition. The method utilizes the Orr-Sommerfeld equation solved for the group of Falkner-Skan boundary layer profiles at various shape parameters (H) and unstable frequencies (Drela, Giles 1987). The solutions are then linearized for different

constant H values in order to relate them to the amplification factor, n. Transition is assumed to occur when the most unstable frequency in the boundary layer has exceeded the value e^n where n is a predetermined value, usually taken to be 9 to model the flow in a *clean* wing tunnel (Drela, Giles 1987).   Use of the e^n method is only appropriate in modeling flow where 2D Tollmien-Schlichting waves are the dominate cause of transition, which is the case in modeling low Re number airfoils (Drela 2000).

1.2.4.3 Validation

Results of a comparison study of 3 airfoils at various Re number are presented by Drela and Giles (1987) as validation of XFOIL's prediction capabilities. Analytic and experimental data is presented for LNV109A and RAE 2822 airfoils. Analysis of the LNV109A airfoil at Re = 250,000, 375,000, 500,000, and 650,000 showed good agreement with experimental results with accurate prediction of laminar separation bubble location, pressure distribution, lift, and drag. A sharp increase in drag below a C_l of 0.9 is predicted which agrees with experimental data.   Additional analysis was run for the LA203A airfoil at Re = 250,000, 375,000, and 500,000.   Analytic and experimental results were found to compare well considering the amount of noise in the data. Displacement thickness and momentum thickness were shown to agree well with experimental results, and a large jump in momentum thickness is clearly visible in both the experimental and analytical results.

An additional study was performed by Singh et al. to validate XFOIL for Re numbers between 80,000 and 300,000 (Signh, Winoto, Shah, Lim, Goh 2000).   Four airfoils were chosen because of there varying shape characteristics and readily available low Re testing data. The airfoils used in the study were the NACA0009, NACA2414, SD7037, and S1223. The NACA0009 XFOIL was shown to agree well with experimental results for Re = 80,000 and 100,000. The NACA2414, SD7037, and S1223 all showed a tendency for XFOIL to over predict lift and under predict drag consistently at all angles of attack.

1.3 Thesis Objectives

The goal of this research is not to develop the best MAV airfoil, nor is it to find the exact coefficient of lift or coefficient of drag values for a specific airfoil and flight conditions. The goal is to provide a link between combinations of geometric shape parameters and anticipated airfoil performance characteristics. The objective is to find which airfoil shapes provide high lift to drag ratios, favorable stall characteristics, achieve high C_l values, have low bubble drag, and small laminar separation bubbles. Emphasis is placed on trends in the data associated with interdependence of the airfoil shape parameters and the airfoil performance characteristics.

A group of airfoils will be analyzed using XFOIL at low Re numbers and the results will be compared to known experimental results for validation. The parameters that control XFOIL's analysis will be tested to determine which values best model known experimental data. A detailed description of the parameters is given in Section 2.3.

A method for defining constant thickness thin/cambered/reflexed airfoils will be suggested that uniquely defines airfoil shape using 5 airfoil shape parameters. The parameters are thickness (T), max camber (C), position of max camber (xC), max reflex (R), and position of max reflex (xR). Airfoils representing all possible combinations of at least 2 *T* values, 4 *C* values, 4 *xC* values, 3 *R* values, and 3 *xR* values will be generated for analysis in XFOIL.

The airfoils generated from combination of all 5 airfoil parameter values will be analyzed using XFOIL at 3 different Re numbers. The 3 Re numbers will be chosen based on the range of validated Re numbers for XFOIL with a focus on the low range values. The goal is to attain data in the Re number range of 60,000 to 200,000. Angle of attack will be varied from 0° to stall for each airfoil and Re number. The variables C_l, C_d, C_m, x_{tr} will be recorded for all angles of attack. C_l and C_d will be used to determine $C_{l,max}$, stall angle of attack (α_{stall}), $C_l/C_{d,max}$, and the angle of attack of $C_l/C_{d,max}$ ($\alpha_{Cl/Cd,max}$). The boundary layer variables, C_f, coefficient of pressure (C_p), and H will be recorded at increments of 2° angle of attack to be used in determining the laminar separation bubble region.

Wind tunnel models for 5 airfoils will be tested to determine boundary layer separation and reattachment location using surface oil flow visualization for Re numbers of 100,000 and 150,000 over a range of angles of attack determined by XFOIL's predications of boundary layer behavior. Results will be compared to the results obtained from the XFOIL simulation for validation of XFOIL. Additionally a collection of known boundary layer separation and reattachment data for an E387 airfoil will be compared to wind tunnel results and XFOIL boundary layer predictions as a validation of the experimental procedure and wind tunnel.

2 Airfoil Development

The first section of this chapter addresses the known performance characteristics of a range of airfoils at low Reynolds numbers and the driving airfoil shape parameters that lead to specific airfoil performance   The second section addresses previous low Re number airfoil designs and their origins. The third section outlines the methods available to generate thin/cambered/reflexed airfoil MCLs. The final section details how the airfoils are generated for analysis.

2.1 Desired Airfoil Performance

MAVs are plagued by poor efficiency and lift generation because of low Re number effects. Depending on the mission requirements or desired flight characteristics airfoils that exhibit high lift to drag ratios, slow stall speeds, high lift generation, or favorable pitching moment behavior are essential for success.   The following section will address each of these characteristics.

C_l/C_d is considered a measure of airfoil efficiency and the most critical parameter in determining MAV performance. A study performed at The University of Arizona showed that a variation in flight speed of 25% could be achieved through changes in airfoil camber alone (Null, Shkarayev 2004). This would mean an increase of 25% in range at the same power consumption because of changes in C_l/C_d. High C_l/C_d airfoils usually have less camber and are unable to achieve high $C_{l,max}$ values. The angle of attack that the maximum lift to drag ratio occurs at is important. Airfoils that achieve a high C_l/C_d that occurs at low angles of attack must fly faster, or carry less payload to operate at peak C_l/C_d performance. If $C_l/C_{d\ max}$ occurs at a high angle of attack the flight speed must be slower to attain high C_l/C_d performance.

$C_{l,max}$ is critical for defining the payload capacity and slow flight capabilities of a MAV. $C_{l,max}$ is an upper limit on lift generation for a particular airfoil and is usually accompanied by a high coefficient of drag (C_d) resulting in low C_l/C_d values and high power consumption requirements. In cases where an MAV's payload requires it to operate near or at $C_{l,max}$ significant thrust is required to overcome the high drag created. If surplus thrust is available at $C_{l,max}$, the larger the available payload capacity is. Slow flight capabilities are also dictated in the same way; the higher $C_{l,max}$ is the slower the MAV will be able to fly.

An important characteristic, often overlooked when considering airfoil performance, is the pitching moment coefficient (C_m). The 0.15m requirement has results in the predominance of flying wing configuration for MAV designs. In this configuration the wing must make a positive contribution to pitch stability which means the slope of the pitching moment curve ($C_{m,\alpha}$) must be *negative* (-), and C_m at $\alpha = 0°$ ($C_{m,0}$) must be *positive* (+) (Nickel, Wohlfahrt 1994). A traditional cambered airfoil cannot achieve these requirements and reflex must be added to the airfoil. Reflex is a slight upturn in the trailing edge of the airfoil that shifts the pressure distribution aft placing more upward force on the lower surface of the airfoil near the trailing edge (Nickel, Wohlfahrt 1994). The addition of reflex reduces the overall lift generation capabilities of the airfoil but is necessary for stable MAV flight.

The stall behavior of an airfoil can result in poor MAV performance if not understood and anticipated. The most advantageous stall behavior is a soft stall, where C_l does not experience a large decrease after $C_{l,max}$ is achieved. This allows the aircraft to easily recover from above stall angle of attack flight. Airfoils that exhibit soft stall behaviors are often slightly cambered and do not achieve high $C_{l,max}$ values. Airfoils with only slight camber have small adverse pressure gradients which prevent short bubble bursting stall and tend to cause gradual leading edge stall. More traditional abrupt stall behavior occurs for highly cambered airfoils that suffer from higher adverse pressure gradients and short bubble bursting leading edge stall. (Interpretation of data from Null, Shkarayev 2004; Pelletier, Mueller 2000; Jenkins, et al. 1998)

2.2 Previous Thin Airfoil Designs

There have been 2 primary methods for generating thin/cambered airfoil geometry, the first utilizes the mean camber line (MCL) or top surface of a known airfoil, the second defines a MCL using an nth order polynomial. The goal of each of these methods was to design an airfoil that met certain performance requirements. In the case of using a known airfoil the intent was that the newly created thin airfoil would have similar performance characteristics at low Re numbers as the master airfoil did at higher Re numbers. The nth order polynomial method was developed for implementation in a thin airfoil theory design optimization routine and provides more freedom in choosing airfoil shape (Albertani, et al. 2004).

A primary example of the first method is an airfoil developed by Shkarayev et al. (2004) utilizing the top surface of a modified S5010 airfoil. Modifications were made to the location of max camber in order to reduce the large negative pitching moment. The airfoil showed significant performance increase over its thicker version at low Reynolds numbers. The disadvantage of this method is that specific airfoil performance is not guaranteed. Also, as is evident in the study done by Shkarayev et al. (2004), additional changes may be necessary to achieve the exact performance required requiring numerous unplanned design iterations. Figure 2.1 shows the modified S5010-top MCL.
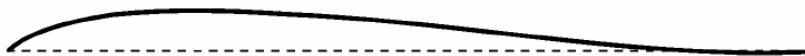
Figure 2.1: Modified S5010-top MCL (courtesy of Shkarayev)

The nth order polynomial method was developed to address the limitations of utilizing only known airfoils. Defining a MCL using a series of polynomial coefficients allowed for implementation in an optimization algorithm that utilized XFOIL's inviscid solver and thin airfoil theory (Albertani, et al. 2004). This method proved excellent in generating a good performing MAV airfoil for low Re number operation. One drawback is with the use of an inviscid solution, done to simplify the optimization. However, this is not a limitation of the

method just its implementation. The one limitation of the nth order method is the indirect relationship of the coefficients and the airfoil parameters used to define the airfoil's shape. Additionally, n^{th} order polynomials may require a significant number of higher order terms to effectively define the desired airfoil shape. A more detailed explanation of the limitations is given in the following section. Figure 2.2 shows an example of an nth order MCL.

$$y = 0.5621x^3 - 1.0125x^2 + 0.4504x$$
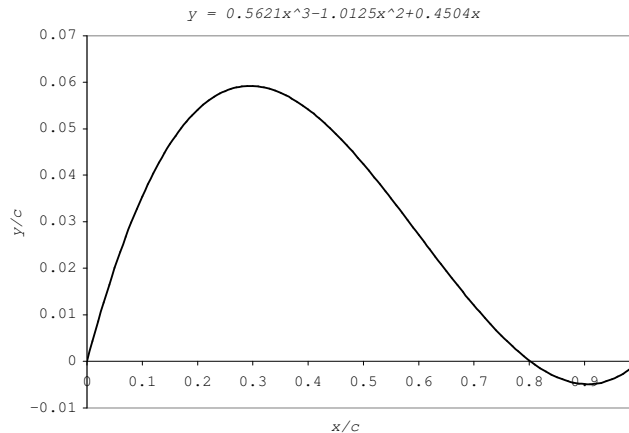
Figure 2.2: Example of an nth Order Polynomial MCL

2.3 *Isolation of Airfoil Shape Parameters*

The variables of interest when considering a thin/cambered airfoil with reflex are max camber (C), position of max camber (xC), max reflex (R), and position of max reflex (xR). These variables are chosen because they represent a direct link to airfoil performance. An airfoil with these variables defined is presented in Figure 2.3. It is important that when developing a scheme for airfoil design that these four variables are independent and than changes in one does not result in major changes in another. This ensures changes made during an optimization routine or through manual adjustments are predictable. This is the major concern with defining a MCL using polynomial coefficients; changes in a coefficient may result in changes to more than one aspect of the airfoil's shape.
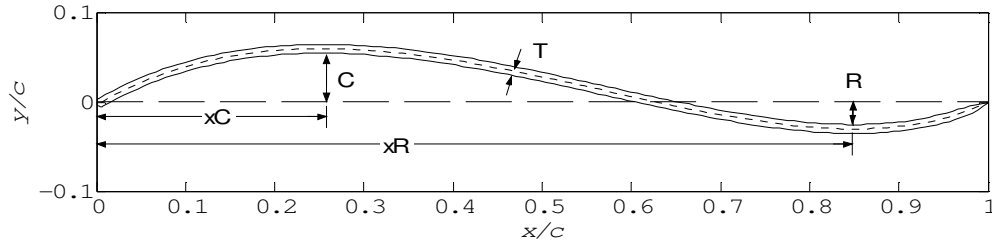
Figure 2.3: Description of Airfoil Shape Parameters

2.3.1 n[th] Order Polynomial Method

The goal of the nth order polynomial method is to fully define an airfoil's MCL using C, xC, R, xR and find the resulting polynomial coefficients. To be successful the method must be able to produce a MCL for a wide variety of airfoil variables. To simplify the method the airfoil will be normalized to a chord length of 1. Knowing the chord length is 1, and given C, xC, R, and xR 4 defining points and 2 defining slopes can used to solve for the required polynomial coefficients. The 4 defining points are the leading edge at (0,0), the trailing edge at (1,0), the point of max camber (xC, C), and the point of max reflex (xR, -R). The convention is that the reflex value is expressed as a magnitude below the chord line. The 2 defining slopes are both 0 at the points of max camber and max reflex. The 4 point and 2 derivative conditions are applied to a 5th order polynomial with unknown coefficients, shown in Equation 1. The resulting set of 6 equations, solved for the unknown coefficients in terms of the known airfoil parameters given in matrix form is shown in Equation 2. The matrix is easily solved using MATLAB. The resulting polynomial can then be plotted to show the MCL. The x coordinate is given in standard form normalized to the chord length.

$$y\left(\frac{x}{c}\right) = \alpha\left(\frac{x}{c}\right)^5 + \beta\left(\frac{x}{c}\right)^4 + \gamma\left(\frac{x}{c}\right)^3 + \delta\left(\frac{x}{c}\right)^2 + \phi\left(\frac{x}{c}\right).$$

Equation 1: 5th order poly with unknown coefficients.

$$
\begin{bmatrix} \alpha \\ \beta \\ \gamma \\ \delta \\ \phi \end{bmatrix} = \begin{bmatrix} 1 & 1 & 1 & 1 & 1 \\ (xC_{max})^5 & (xC_{max})^4 & (xC_{max})^3 & (xC_{max})^2 & (xC_{max}) \\ (xR_{max})^5 & (xR_{max})^4 & (xR_{max})^3 & (xR_{max})^2 & (xR_{max}) \\ 5(xC_{max})^4 & 4(xC_{max})^3 & 3(xC_{max})^2 & 2(xC_{max}) & 1 \\ 5(xR_{max})^4 & 4(xR_{max})^3 & 3(xR_{max})^2 & 2(xR_{max}) & 1 \end{bmatrix}^{-1} \begin{bmatrix} 0 \\ C_{max} \\ -R_{max} \\ 0 \\ 0 \end{bmatrix}
$$

Equation 2: 6 equations in matrix form.

To check the method's ability to model various MCLs a simple test of two sets of variables is presented. For the test C, xC, and R remain constant at values of 10%, 30%, and 1% chord respectively and xR is set to 75% and 85% chord. The resulting 2 MCLs are shown with the y-axis expanded in Figure 2.4.
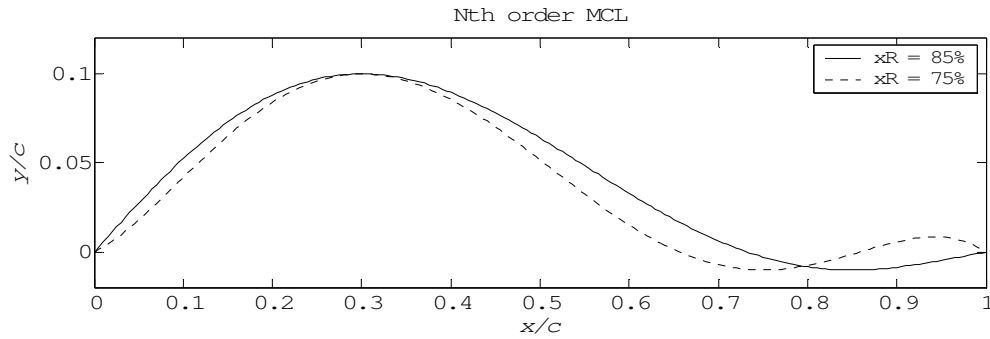
Figure 2.4: Comparison of nth Order MCLs

The airfoil with an xR of 85% appears to have acceptable features, such as no inflection point near the leading edge, only one local max and one local min, and positive trailing edge slope. The airfoil with xR of 75% exhibits all of these characteristics. In addition, there is a strong coupling of leading edge shape and position of max reflex. Both of the airfoils meet the constraints set by 4 points and 2 slope requirements, yet they exhibit radically different shapes with only a slight change in one defining parameter.

It is evident that a 5th order polynomial is insufficient to fully constrain the MCL shape for all possible defining parameter combinations. Higher order polynomials are not possible because additional defining parameters would be required with no guarantee that similar

24

behavior would not result. Addition of auxiliary parameters would also add complexity to any parametric study or optimization routine that may implement this method.

The nth order polynomial method, though used previously, is deemed insufficient due to its inability to simply and reliably model an airfoil MCL using the given constraints. To do it properly would require additional constraints resulting in higher order terms that unnecessarily increase complexity.

2.3.2   Bezier Curve Description

The Bezier curves were first introduced by the French automotive engineer P. Bezier in the 1960's (Kreyszig 1999). Bezier curves are defined by parametric equations and chosen specifically for their ability to create smoothly transitioning curves that serve both form and function (Scrbarough 1992). A *simple* Bezier curve is defined by 2 endpoints and 2 control points (Scrbarough 1992). The 4 points that create the defining polygon are shown in Figure 2.5. Bezier curves have a number of favorable characteristics, the most relevant to this work are:

- If n is the number of control points, (n + 1) is the degree of the polynomial defining the curve.
- The line segment connecting an endpoint with its nearest control point defines the tangent vector at the endpoint.
- The cure is bound by the line segments that make up the defining polygon.
- The curve does not oscillate more than (n+1) times, which is known as the variation diminishing property.
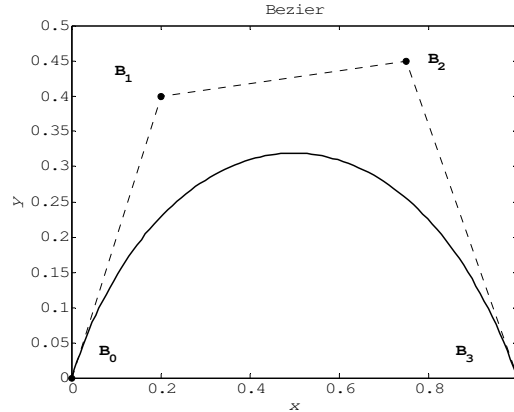
Figure 2.5: Bezier Curve with Defining Polygon and Control Points

The defining parametric equations in t for a 3rd order polynomial Bezier curve are presented in Equation 2.1 thru Equation2.6 (Kreyszig 1999). The endpoints are defined as *(x$_0$,y$_0$)* and *(x$_3$,y$_3$)* and the control points are defined as *(x$_1$,y$_1$)* and *(x$_2$,y$_2$)*. The domain of t is 0 to 1; {0 $\leq$ t $\geq$ 1}.

For the x coordinate:

$$x(t) = a_x t^3 + b_x t^2 + c_x t + x_0 \quad \text{Equation 2.1}$$

Where:

(a) $x_1 = x_0 + c_x/3$

(b) $x_2 = x_1 + (c_x + b_x)/3$ Equations 2.2 (a,b,c)

(c) $x_3 = x_0 + c_x + b_x + a_x$

For the y coordinate:

$$y(t) = a_y t^3 + b_y t^2 + c_y t + y_0 \quad \text{Equation 2.3}$$

Where:

(a) $y_1 = y_0 + c_y/3$

(b) $y_2 = y_1 + (c_y + b_y)/3$ Equations 2.4 (a,b,c)

(c) $y_3 = y_0 + c_y + b_y + a_y$

26

Equations 2.2 (a, b, c) and 2.4 (a, b, c) are solved for the polynomial coefficients of x(t) and y(t) as shown in Equations 2.5 (a, b, c) and 2.6 (a, b, c).

For x(t):

(a) $c_x = 3 \cdot (x_1 - x_0)$

(b) $b_x = 3 \cdot (x_2 - x_1) - c_x$ Equation 2.5 (a, b, c)

(c) $a_x = x_3 - x_0 - x_x - b_x$

For y(t):

(a) $c_y = 3 \cdot (y_1 - y_0)$

(b) $b_y = 3 \cdot (y_2 - y_1) - c_y$ Equation 2.6 (a, b, c)

(c) $a_y = y_3 - y_0 - y_y - b_y$

Knowing the x-y coordinates of the end points and control points fully defines the Bezier curve.

2.3.3 Bezier Curve Method

The goal of the Bezier method is similar to the nth order polynomial method; to fully define an airfoil's MCL using C, xC, R, xR and find the resulting Bezier control points. The airfoil is normalized to a chord length of 1, which results in the two Bezier endpoints being fully defined at (0,0) and (1,0). A closed form solution linking the 4 airfoil parameters to the x-y coordinates of the 2 control points grows rapidly in complexity and is difficult to solve. An easier, iterative method was chosen that capitalizes on the de-coupled state of the x and y coordinate equations. Relying on the derivative condition at xC and xR the y coordinates of control points are set first, utilizing an arbitrary x coordinate value. The y coordinate values of the control points are iteratively adjusted until both the local min and local max values of the resulting Bezier curve match the defining values of C and R within a set tolerance, usually 10^{-6}. The x values of the two control points are then iteratively adjusted until the x coordinates of the local min and local max values of the resulting Bezier curve match the defining values of xC and xR within the set tolerance. This iterative method is easily

implemented in MATLAB. Computation time is negligible, and once an airfoils control points are known the process does not need to be repeated. An example of a MCL generated using the Bezier method is given in Figure 2.6 with its control points labeled and defining polygon shown by a dotted line.
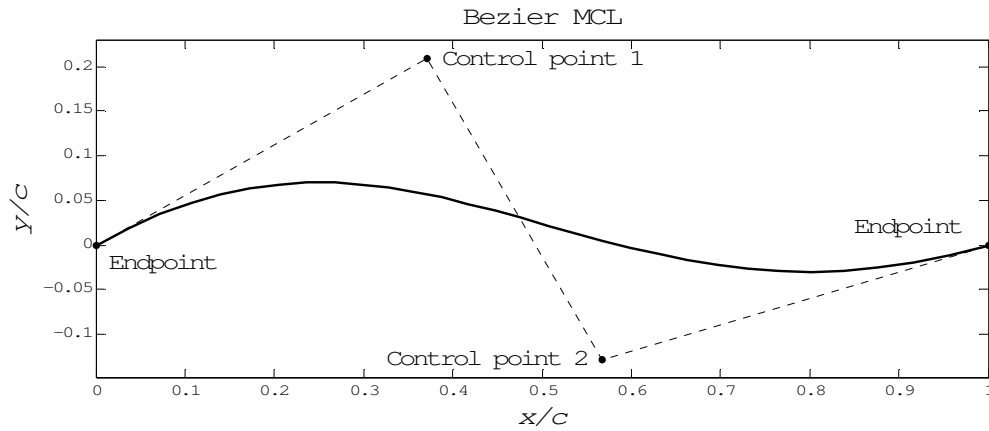
Figure 2.6: Bezier MCL with Defining Polygon and Control Points

The same test that was performed for the nth order polynomial method was recreated for the Bezier method to check the method's ability to model various MCLs. C_{max}, xC_{max}, and R_{max} remained the same constant values of 10%, 30%, and 1% chord respectively and xR_{max} was set to 75% and 85% chord. The resulting 2 MCLs generated from the Bezier method are shown with the y-axis expanded in Figure 2.7.
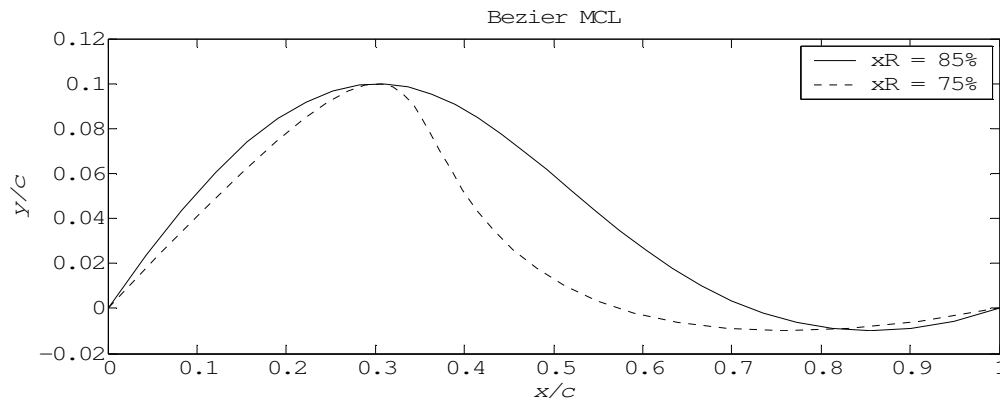
Figure 2.7: Comparison of Bezier MCLs

The 85% xR airfoil shows a very similar shape to the nth order method and has good shape behavior. The 75% airfoil again shows a connection between xR and leading edge slope and shape, yet the inflection point present in the nth order method is not present in the Bezier method. The trailing edge slope also shows a correlation to the magnitude of xR yet the Bezier method does not result in an additional local maximum near the trailing edge, as the nth order method did. These characteristics make the Bezier method superior to the nth order method.

2.4 Airfoil Generation

There are five variables required to fully define a thin/cambered/reflexed airfoil, thickness (t), C, xC, R, and xR. The two camber and two reflex variables are used in the Bezier method to define the MCL, with a slight adjustment based on thickness. A constant thickness distribution with a circular leading edge and parabolic trailing edge is then used to define the upper and lower surfaces of the airfoil from the MCL. The resulting x-y coordinates for the upper and low surfaces are then saved to a coordinate (*.cor) file to be opened by an analysis program later. A more detailed description of the methods is presented in the following sections. A number of Bezier airfoil shapes are presented in Appendix B as examples.

It is important to mention that for simplicity all airfoils generated by the Bezier method follow the same naming convention, i.e. BEZ062518510, which represents an airfoil that has 6% camber at 25% chord, 1% reflex at 85% chord, and is 1% thick; note that the final value is 10 times the thickness in %chord.

2.4.1 Thickness, Leading Edge, and Trailing Edge

The standard convention for defining airfoil thickness relies on a vertical displacement above and below the MCL of an airfoil, generally given by a mathematical function. This is not the case for thin/cambered/reflexed airfoil generation. The common method for constructing

very thin airfoils is to start with a material of constant thickness and form it into the desired shape or to layer materials on a mold of the MCL until the required thickness is achieved. Both of these methods result in an airfoil that has constant thickness perpendicular to the MCL of the airfoil, not vertically in the y-axis. To model this shape, half of the constant thickness value is applied above and below the MCL using the local normal vector direction.

It has been shown through wind tunnel testing that leading and trailing edge shape has negligible effect on thin/camber plate airfoil performance (Pelletier, Mueller 2000). Leading and trailing edge shape does however play a very critical role in numerical analysis as an important parameter in determining convergence. A semi-circle was chosen for the leading edge in order to achieve constant curvature at the leading edge. Sharp increases in curvature often result in high local peaks in pressure which make numerical convergence difficult. The semi circle is defined at the forward end point of the Bezier MCL with a radius of ½ T so that tangency is achieved at the upper and lower airfoil surfaces. The leading edge is shown in Figure 2.8.
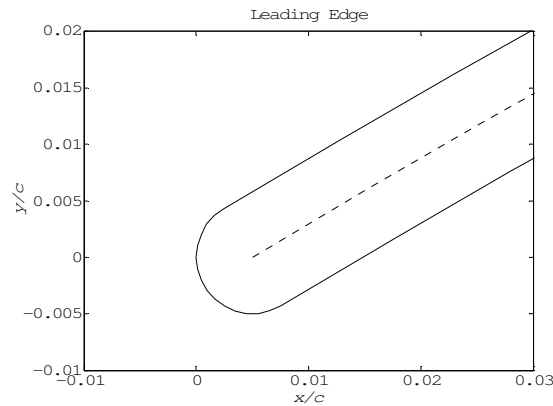
Figure 2.8: Bezier Airfoil Leading Edge Shape Detail

For the trailing edge 2 intersecting parabolic curves were chosen. At a set distance from the trailing edge, identified by a percentage of the airfoil thickness, a parabola is defined tangent to the upper surface and a second parabola is defined tangent to the lower surface. The two parabolas then intersect at the trailing edge forming a sharp corner. The trailing edge angle is

always the same, regardless of the airfoil thickness because of the way that parabolas are defined. A plot of the trailing edge shape is shown in Figure 2.9. This shape was chosen to allow easy application of the Kutta condition. Originally a circular trailing edge was employed but preliminary tests show poor convergence because of the Kutta condition requirement.
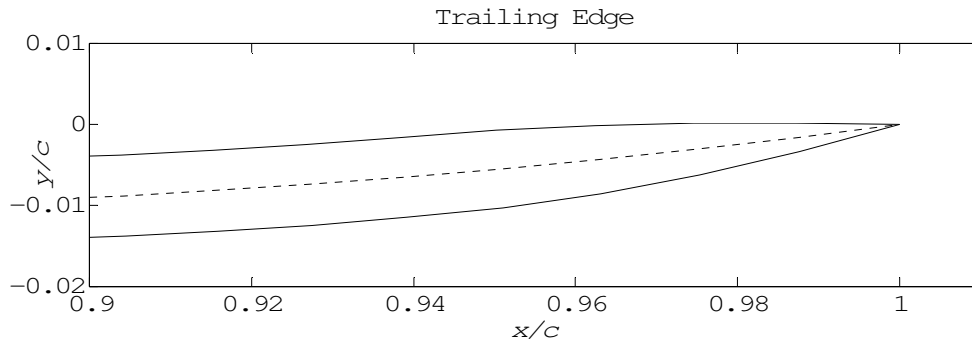
Figure 2.9: Bezier Airfoil Trailing Edge Shap Detail

2.4.2   Mean Camber Line Modifications

The MCL generated by the Bezier method previously described requires a slight modification due to the airfoil's thickness and the leading edge radius. All airfoil x coordinates are limited to $0 \leq x \leq 1$, which causes a problem when the MCL is defined from $0 \leq x \leq 1$ and a circular leading edge is applied. In order to alleviate this issue the first end point used in the Bezier method is shifted half the thickness of the airfoil to the right, which is the coordinate (.5*T,0). This is evident in Figure 2.8; with the dashed line not terminating at the origin (0,0). This accounts for the leading edge radius, which is .5*T. The airfoil thicknesses tested are so small that the change to the MCL is negligible.

2.4.3   MATLAB Functions

The method for generating Bezier airfoils described in the previous section was implemented in a series of MATLAB scripts and functions which can be found in Appendix C for reference.

A function, Bezier.m, was used to find the location of the control points required to generate a Bezier MCL that matched the desired airfoil shape parameters. Once the points were determined a script Add_Thickness.m found the local normal vector along the MCL and defined the upper and lower surfaces as well as the leading and trailing edges. Bezier_Airfoil_Generator.m was written to iteratively call the Bezier.m function for all combinations of the airfoil parameters supplied and generate the airfoil coordinate files. The inputs of Bezier_Airfoil_Generator.m are, the directory where the airfoil coordinate files will be saved, the name of the file that will contain a list of all the airfoil coordinate files generated, and five vectors containing all possible T, C, xC, R, and xR values. Bezier_Airfoil_Generator.m outputs a matrix containing the Bezier control points for each airfoil, a matrix that contains the actual C, xC, R, and xR values of the Bezier MCL, and a matrix that contains the supplied airfoil parameters. When all the airfoils are created the actual airfoil parameters are compared with the supplied parameters to verify they are all within the desired tolerance.

3   Tools for Analysis

The first section of this chapter covers the airfoil analysis code XFOIL developed by Drela (1989). The second section address Expect, a program control language that automates analysis done using XFOIL. The final section outlines the data processing tools developed to handle the data files created by XFOIL.

3.1   XFOIL

XFOIL was developed specifically to handle the highly complex boundary layer flow phenomena associated with low Re number flows and boundary layer-shock interactions present in high speed flows. XFOIL has been accepted by the MAV community as a reliable low Re number airfoil analysis tool. This is evident in XFOIL's prevalence in studies of 2D airfoils; all nine of the low Re numbers airfoil studies addressed in research utilize XFOIL.

3.1.1   History

Since its introduction by Mark Drela in 1986 as XFOIL 1.0, numerous changes and revisions have been incorporated as XFOIL evolved into its final version. Most changes were to address difficulties discovered during use, which has resulted in a program that implements a very user friendly, multifunctional environment. The implementation of a command line user interface started out as a fundamental shift from the batch-type CFD codes prior to 1986, however the proliferation of graphic user interfaces have rendered it outdated. In 2000, XFOIL 6.94 was officially frozen and no further changes made. XFOIL 6.94 for windows, downloaded from http://web.mit.edu/drela/Public/web/xfoil/ on 8/5/05 is the version used to perform the analysis presented.

33

3.1.2 Variables

There are a number of user defined variables that control different aspect of the analysis process such as convergence, speed, and accuracy of the solution. The variables are grouped into three different sections for simplicity. The three groups are, geometric, method, and solution. Each of the groups will be discussed in detail in the following sections, including a description of effect each has on XFOIL's operation and solution method.

3.1.2.1 Geometric Variables

The shape of the airfoil imported into XFOIL is directly defined by the Bezier method described in Section 2.3.3. The airfoil's representation in panel form is then defined by XFOIL. XFOIL utilizes a panel method solution scheme which requires the airfoil to be defined by a number of points connected by straight lines, known as panels (Drela, Giles 1987; Drela 1987). The maximum number of panels is defined by one less than the maximum number of points, which is limited to 280 by XFOIL. The number of panels has a direct effect on the time required to perform each of the solution iterations. How the panels are distributed over the airfoil is critical for solution convergence. The number of panels is defined by the variable N and the panel distribution parameters, panel bunching, and trailing edge/leading edge panel density ratio are defined by P, and t respectively. There is an additional parameter, TEgap which controls the gap between the two points that define the trailing edge. TEgap is used to improve convergence by softening the Kutta-condition requirement.

In order to best describe the intended airfoil shape, airfoils created by the Bezier method are defined by 280 equally distributed points and then re-paneled in XFOIL using the user defined parameters N, P, and t. The number of panels used is a compromise between computation time and accuracy. In a study performed by Drela (1989), an FX67-K-170 sailplane airfoil was tested at varying panel densities. It was found that N = 120 was required to achieve an accurate converged solution. There is a slight amount of variation in the

relationship between N and accuracy which is attributed to the change in panel locations which affects the turbulent transition location. In cases of low Re number flow, where laminar separation bubble size is quite large, the required panel density decreases. Increasing local panel density in the region of an anticipated short laminar separation bubble can also reduce the overall panel requirement.

Panel convergence is considered to have occurred when the addition of more panels to an airfoil results in a minimal change in performance. A test similar to the one performed by Drela was conducted on a BEZ053027510 airfoil to determine the optimal number of panels required to achieve panel convergence. The results of this test are shown in Figure 3.1. The baseline for the test was set at 100 panels. The number of panels was increased in increments of 25 up to 275, 4 less than the max panel limit. An average percent difference in C_l was then calculated at all converged angle of attack. For example, the 125 panel airfoil has an average percent difference in C_l from the 100 panel airfoil of about 8%; that is to say there was an average of 8% change in C_l values from the 100 panel airfoil to the 150 panel airfoil. The jump at 225 panels is attributed to the fluctuation of the transition location as described by Drela (1989). At and above 250 panels the difference in C_l due to changes in the number of panels is less than 1%, resulting in an acceptable of panel convergence. It can also be seen from Figure 3.1 that the percent difference value for 250 panels slightly increased, signifying a minor fluctuation due to a slight change in transition location. As the number of panels increases, fluctuations due to changes in transition location become less because changes in panel location reduce. From this case it was determined that increasing the number of panels to at least 250 would be required to achieve panel convergence. Increasing the number of panels above 250 would result in marginal improvements in panel convergence and require additional computational time.
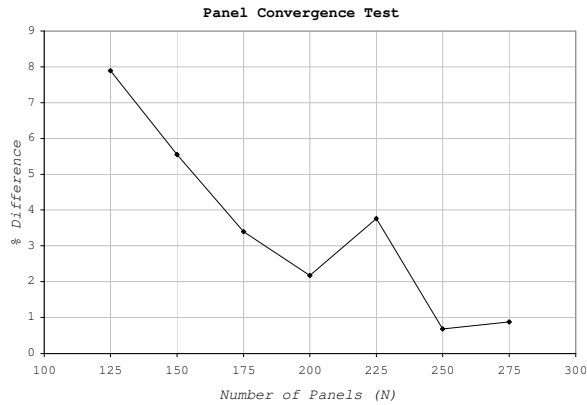
Figure 3.1: Panel Convergence Test

Increasing panel density in the region of anticipated laminar separation can better resolve airfoil performance. However in the case where an airfoil is examined over a wide range of angle of attack the laminar separation bubble location may move over the entire airfoil surface. In this case it is important to ensure that the entire airfoil surface receives sufficient panel density; this is achieved by limiting how dense the leading edge panel density is. Leading edge density is still important because short laminar separation bubbles occur near the leading edge and smaller bubbles require higher panel density. To achieve the best panel distribution the proper combination of P, and t must be chosen. P controls the panel bunching parameter and is limited to the range of 0 to 1; 0 results in a uniform panel distribution irregardless of the other parameters, 1 results in the full application of the other parameters. For consistency P = 1 was always used. The trailing edge/leading edge panel density ratio controls the difference between the leading edge and trailing edge densities. A very small t packs more panels at the leading edge where a large t packs more panels at the trailing edge. A t value of 0.15 provides good panel density near the leading edge to resolve small laminar separation bubbles yet leaves sufficient panel spacing at the trailing edge to resolve any separated flow. The resulting panel distribution for a BEZ052518510 airfoil is presented in Figure 3.2.

36
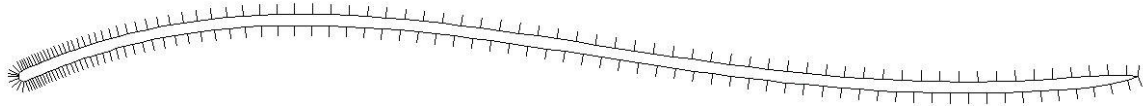
Figure 3.2: XFOIL Panel Distribution

The TEgap parameter is controlled in the geometric design routine of XFOIL. Setting a trailing edge gap, only slightly greater than zero drastically improves convergence of the numerical solution. This is because of the strict numerical constraint applied by the Kutta condition in cases of a sharp trailing edge. When the upper and lower panels at the trailing edge meet to form a sharp trailing edge, the corresponding boundary layers must match identically at the last panel. In the case of a trailing edge gap, the upper and lower surface boundary layers are able to adjust slightly aft of the trailing edge before coming together. The small adjustment causes a decrease in the interdependence of the upper and lower boundary layers and an increase in convergence. A TEgap of 0.001 was used for all Bezier airfoils as it was the minimum value that caused a noticeable increase in convergence levels. It is also the default value for any NACA series airfoil generated by XFOIL.

3.1.2.2 Method Variables

The variables that directly effect XFOIL's governing methods are, Ncrit, $X_{tr,upper}$, $X_{tr,lower}$, and M. Ncrit corresponds to the critical amplification ratio associated with the e^n transition method. $X_{tr,upper}$ and $X_{tr,lower}$ are user defined transition locations for the upper and lower surfaces; these variables override e^n transition prediction method and are useful for measuring the effect of a boundary layer trip. M is the parameter assigned to Mach number and is utilized in determining compressibility effects.

Mach number is the simplest user defined parameter to explain because it is always set to zero when considering MAV applications. The Mach number is utilized by XFOIL in the Karman-Tsien compressibility correction equation. When a Mach number of M=0 is used

37

the Karman-Tsien equations simple states that the C_p is equal to the incompressible coefficient of pressure ($C_{p,inc}$). This is the essence of the incompressible flow assumption.

The method variables $X_{tr,upper}$ and $X_{tr,lower}$ are only modified in the case where the specific location of transition is known before an analysis is performed. This can occur when a boundary layer trip is present on the airfoil surface, or if experimental tests were performed prior to analysis. In cases where values are specified free transition can occur ahead of the set location, but if the boundary layer is laminar at the point specified, transition is artificially induced. In most cases both $X_{tr,upper}$ and $X_{tr,lower}$ are left at their default value of one, allowing for free transition at any point on the airfoil.

The natural log of the amplification factor at which transition occurs is defined by Ncrit. The proper value of Ncrit depends on turbulence level of the flow being modeled. For a *clean* wind tunnel, an Ncrit value in the range of 10-12 is suggested (Drela 2000). For an *average* wind tunnel, 9 is suggested as the standard e^9 method. An Ncrit value from 4 to 8 is suggested for a *dirty* wind tunnel. In most cases, experimental results must be compared to analytic results in order to determine the best Ncrit value. The results of such a comparison are given in Section 3.1.5.

3.1.2.3 Solution Variables

The solution variables, Vacc, iter, and init all a direct effect on how much computational time is required for a converged solution or even if it is possible. Vacc is known as the viscous solution acceleration parameter and is generally used to reduce computational time. The maximum number of iterations to be performed is controlled by the iter parameter. The init parameter controls whether boundary layer initialization takes place at each calculated angle of attack.

The optimal iteration limit is difficult to determine. The large number of variables that effect how many iterations are required for convergence prevents establishing a simple relationship. As in most iterative solution methods it is thought that the more iterations the more likely a

solution will be found; but this is not always the case. The iteration limit does have a direct effect on solution time, requiring more time for more iterations. Iteration limit is predominately set based on time constraints alone and if insufficient convergence levels are achieved additional iterations are added.

Utilizing the previous converged solution as an initial guess for the next solution is a familiar method in numerical solution techniques, and is directly controlled by the init variable in XFOIL. In cases where the previous boundary layer values are used as a guess for the next solution, convergence is achieved in a fraction of the number of iterations as the previous case. XFOIL was set to always use the previous solution to minimize the solution time.

The viscous acceleration parameter, Vacc, is used as a minimum cut-off value for elements in the boundary layer coefficient matrix solved every iteration. The matrix is diagonally dominate and off diagonal elements are often very small if not zero. To better condition the matrix, off diagonal values that are less than Vacc are eliminated. The default value for Vacc is 0.01, however at Re numbers near or less than 100,000 this value may eliminate important elements, affecting the stability of the Newton scheme (Drela 2000). The value of Vacc does not affect the final converged solution. Preliminary tests showed that a reduction in Vacc by an order of magnitude resulted in a 60% increase in convergence with a negligible time penalty. It was determined that Vacc = 0.001 resulted in a sufficient convergence level. If any airfoils exhibit poor convergence an additional solution was recalculated with Vacc set to 0.

3.1.3 Sources of Error

A number of different sources of error that affect XFOIL's solution are presented, however it is only the errors that may be present for one airfoil and not another, or only present for some portion of the analysis that are of importance when considering the relative performance of different airfoils.

In any finite difference scheme the order of accuracy represents a quantifiable source of error. The error introduced by the differencing scheme is referred to as truncation error and is determined by the order of the approximation used. XFOIL employs two various differencing schemes depending on the boundary layer conditions to ensure numerical stability as well as accuracy. In most cases the boundary layer equations are discretized using a two-point central differencing scheme (Drela 2000). The scheme achieves second order accuracy at the price of being marginally stable. In cases of rapid boundary layer parameter change, such as the shape parameter near transition, the central differencing scheme exhibits unstable solution behaviors such as, oscillations and overshoots. In this case a much more stable backward Euler scheme is introduced. The backward Euler scheme relies on an upwind differencing scheme to handle rapid changes in boundary layer parameters and results in a first order accurate scheme. Use of the backward Euler scheme is limited in the interest of numerical accuracy. In general the overall method is assumed second order accurate. This error source is consistent in all solutions and is not considered to affect the relative airfoil performance.

As described in Section 3.1.2.1 there is error associated with the number of panels used when a panel representation if an airfoil is used. As can be seen is Figure 3.1, when 250 or more panels are used the difference is on the order of 1%. This can be considered the error associated with a panel airfoil representation. The error is not considered when comparing the performance of different airfoils because the same number of panels and distribution is used for every airfoil analyzed.

3.1.4 Limitations

There are a few known limitations of XFOIL that have a direct effect on the research performed and presented. One major limiting factor is the restriction of minimum airfoil thickness to 1%. Prediction of post stall airfoil performance is also very constrained. There have also been numerous assessments of XFOIL's ability to predict lift and drag.

The panel method that XFOIL employs directly limits the minimum thickness of airfoils that can be tested. In the hypothetical case of zero thickness, the boundary layer matrix would become singular and could not be solved. For the cases of very small thickness, the matrix is not well condition and has relatively large off diagonal elements which makes finding a solution difficult. In cases where a solution is obtained it is considered meaningful (Mark Drela, personal communication, Mar 31, 2001). In the case of airfoils with 1% thickness and above, setting a small Vacc value, as described in Section 3.1.2.3, increases convergence. As airfoil thickness decreases below 1% converged solutions become less likely.

The reliability of converged solutions beyond stall, associated with the occurrence of $C_{l,max}$, is poor. In most cases XFOIL will converge on a solution but large boundary layer thickness and fully separated flow are not well modeled which results in poor lift and drag values. In general only airfoil performance just after stall is relevant and additional data is not reliable.

There have been a number of studies that have addressed XFOIL lift and drag results. What is common to almost all of them is that they report that XFOIL over predicts lift and under predicts drag (Kellogg, Bowman 2004; Signh, et al. 2000). In a study by Kellogg and Bowman (2004), XFOIL's prediction of maximum lift to drag ratios was 11% higher than what was experimentally measured. The trend had been found consistently for all angle of attack that it is not considered a major limitation in comparison studies of XFOIL results.

3.1.5 Validation

The only way to guarantee accurate low Re number airfoil performance data is to gather it through wind tunnel testing. In the absence of accurate wind tunnel facilities, and when large numbers of airfoils must be tested, analytic tools must be utilized. It is the goal to show, in the validation presented, that XFOIL provides accurate trend capabilities results for Re numbers greater than 60,000. There is also an effort made to find the Ncrit value that results in the best match of trends between XFOIL and experimental results.

3.1.5.1 Previous Validation

XFOIL has undergone numerous validation studies. The original study, performed by Drela when XFOIL was first released in 1986, showed the program's ability to predict airfoil performance for a range of Re numbers from 250,000 to 650,000. Wind tunnel test and XFOIL results were compared for three airfoils, LNV109A, LA203A, and RAE2822, which were chosen for their distinct boundary layer, lift, and drag characteristics. The results of the analysis showed XFOIL could accurately predict airfoil performance over the tested Re range.

Further validation was preformed by Singh et al. (2000), Kellogg and Bowman (2004), and Selig et al. (1997) to evaluate XFOIL's performance at lower Re numbers. Singh et al. (2000) compared XFOIL results to experimental data for four airfoils. The four airfoils, NACA0009, NACA2414, SD7030, and S1223 where chosen for their readily available low Re number data and varying camber and thickness values. The XFOIL and experimental results were compared for Re numbers of 80,000, 100,000, and 300,000. A good correlation between experimental and analytic results was reported for all airfoils and Re numbers, except for S1223, which a poor correlation with experimental results. The conclusion of the comparison was that XFOIL has the ability to accurately predict the relative performance of different airfoils. Similar results were found by Kellogg for three airfoils, E387, SA7035, and GOE417A over a Re number range from 60,000 to 150,000. Comparisons of various airfoils at Re numbers of 200,000 and 300,000 by Selig also showed similar results.   In all comparisons XFOIL's ability to predict airfoil performance decreased as Re number decreased.

3.1.5.2 Present Validation

Through electronic correspondence with Drela, the XFOIL parameter Ncrit was determined to be a potential source for the discrepancy between XFOIL's predictions and wind tunnel measurements (Mark Drela, personal communication, Nov. 15, 2001). An Ncrit value of 9 is

generally chosen to model the flow conditions in a *clean*, low turbulence wind tunnel. Ncrit is inversely proportional to free-stream turbulence level (Tu) using Mack's correlation, presented in Equation 3.1 (Mark Drela, personal communication, Jul. 23, 2001).   By adjusting the Ncrit value used in XFOIL, variation in free stream turbulence can be accounted for.   It is thought that as Re number decreases the dependency of laminar separation bubble formation on free-stream turbulence, and therefore Ncrit, increases.

$$Tu = e^{-(Ncrit+8.43/2.4)} * 100\%$$

Equation 3.1: Mack's Correlation

Analysis of nine different airfoils at three Re numbers of 60,000, 100,000, and 200,000 was performed in order to determine the Ncrit value that best correlated experimental and XFOIL results.   The nine airfoils were, BW3, E221, E387, GM15, NACA0009, NACA64A01, NACA2414, S2048, and SD7080. Ncrit values of 6, 7, 8, and 9 were used to generate airfoil lift and drag polar at the three Re numbers. The four Ncrit values were chosen because the wind tunnel airfoil performance suggests higher than reported turbulence levels.

To determine which Ncrit value resulted in the best match between XFOIL and experimental results, a method based on least squares regression analysis was developed. Least squares regression analysis relies on varying the defining parameters of a guess function, usually in the form of a polynomial, to minimize the sum total of the squared difference between the given data and the corresponding guess function value. In the case of this analysis, the guess function was either the lift or drag polar generated by XFOIL, which varies with changes in the defining parameter, Ncrit. A consistent number of experimental lift and drag data points was not available for all nine airfoils at the three Re number which made comparison of the sum of the squared differences impossible. As an alternative an average squared difference was tabulated for the lift and drag of each airfoil, Re number, and Ncrit value.   This eliminated any bias in the sum of the squared differences that was caused by airfoils that had more or less experimental data available. The average squared difference for lift and drag of all nine airfoils was averaged for each Re number and Ncrit value. The results for lift and drag differed by 2 orders of magnitude. In order to determine the total performance, lift and

drag at all three Re numbers were normalized by a constant value and summed for each Ncrit value; the results are presented in Figure 3.3. In addition, the summation of the squared difference of lift and drag for each Re number is presented in Figure 3.4. Figure 3.3 shows that an Ncrit value of 7 results is the least average squared difference between XFOIL and experimental results. Ncrit values of 6 and 8 are only slightly worse than Ncrit of 7. From the lift and drag plots it is clear the trend in the summation is dictated primarily by the average squared difference of the drag values. The normalized average squared difference for the lift values appears indifferent to changes in Ncrit value. Figure 3.4 highlights the differences for the three Re numbers evaluated. For Re = 200,000 the variation of the normalized average squared difference shows less variation due to changes in Ncrit as Re = 60,000 and Re = 100,000. The results show that an Ncrit value of 7 results in the best match of XFOIL and experimental data as compared to Ncrit values of 6, 8, and 9.
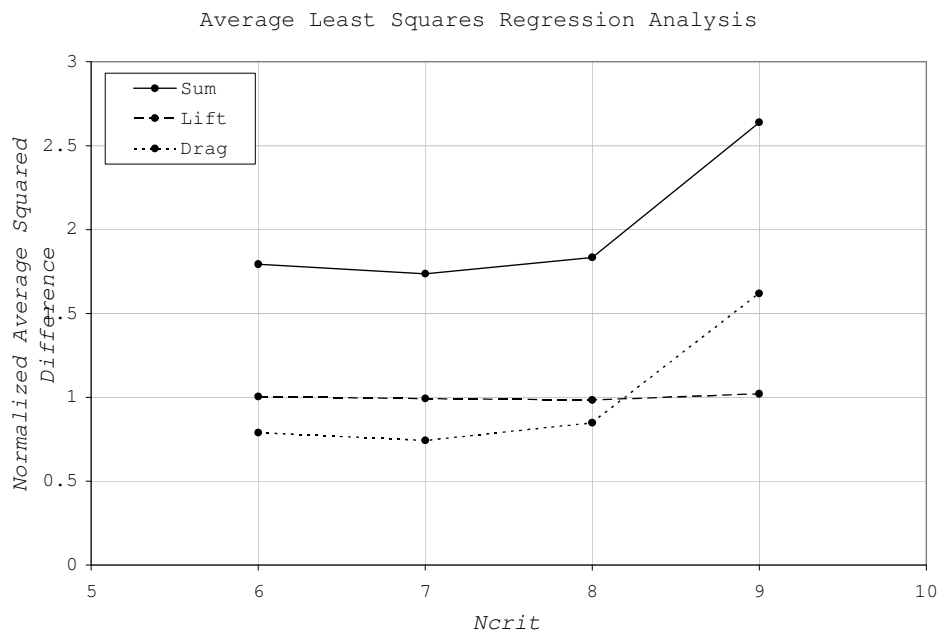
Figure 3.3 Average Least Squares Regression: Lift / Drag
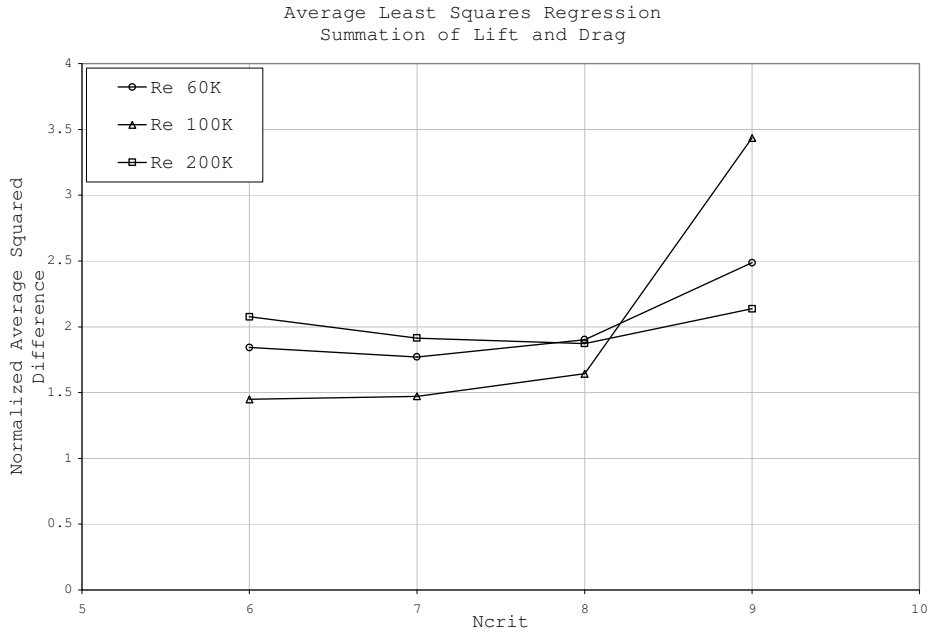
Figure 3.4: Average Least Squares Regression: Re Number

For the purpose of this research the ability to correctly predict trends in airfoil performance, such as lift and drag polar shape, is more critical than the accuracy of the results. Validation of XFOIL's trend prediction capabilities is difficult and relies heavily on empirical assessments. The comparison of experimentally obtained lift and drag data and XFOIL results for various Ncrit and Re number values is presented to validate XFOIL's ability to predict trends. The plots presented were chosen as representation of trends present in the majority of the 54 plots evaluated.

The most consistent trend in both lift and drag for all Ncrit values is the tendency for XFOIL trends to better match experimental trends as Re number increases. This trend was expected and is consistent with previous XFOIL validation studies. In addition, the effect of Ncrit on variation in performance of lift and drag greatly decreases as Re number increases. This is consistent with the hypothesis made prior to testing based on the decreased dependency of lift and drag performance on laminar separation bubble effects with increasing Re number. These trends are clear in the lift polar for the E387 airfoil at Re = 60,000 and 200,000 presented in Figure 3.5 and Figure 3.6 respectively.

45

Figure 3.5: Ncrit Comparison: Lift, E387, Re = 60K
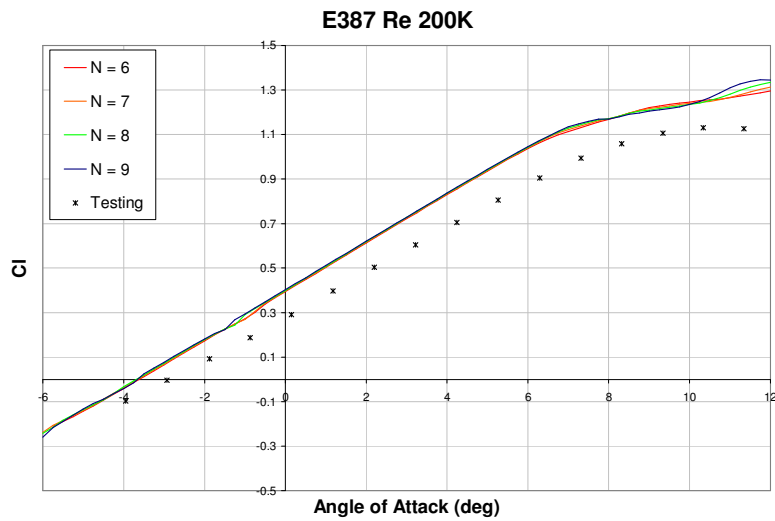
Figure 3.6: Ncrit Comparison: Lift, E387, Re = 200K

Figure 3.5 and Figure 3.6 are also examples of XFOIL's tendency to over predict lift. This trend is consistently found at higher angles of attack, but at and below 0° angle of attack for lower Re numbers XFOIL appears to be as likely to slightly under predict lift as it is to over predict lift. An example of this behavior is presented in Figure 3.7 and Figure 3.8.
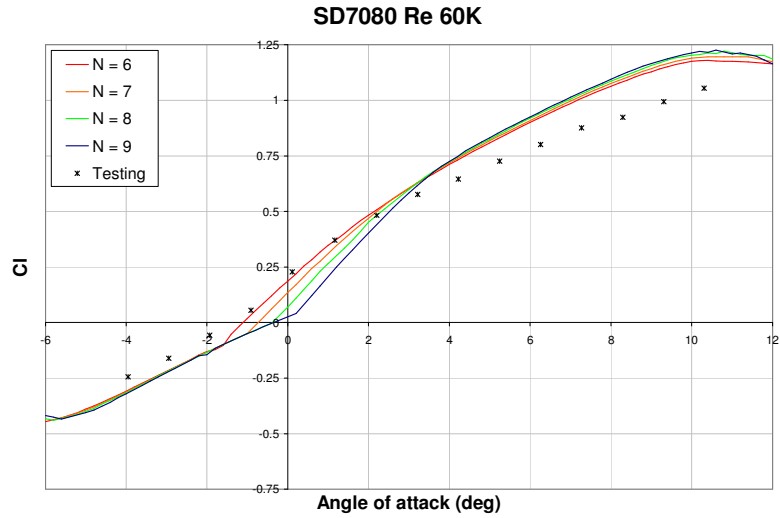
Figure 3.7: Ncrit Comparison: Lift, CD7080, Re = 60K
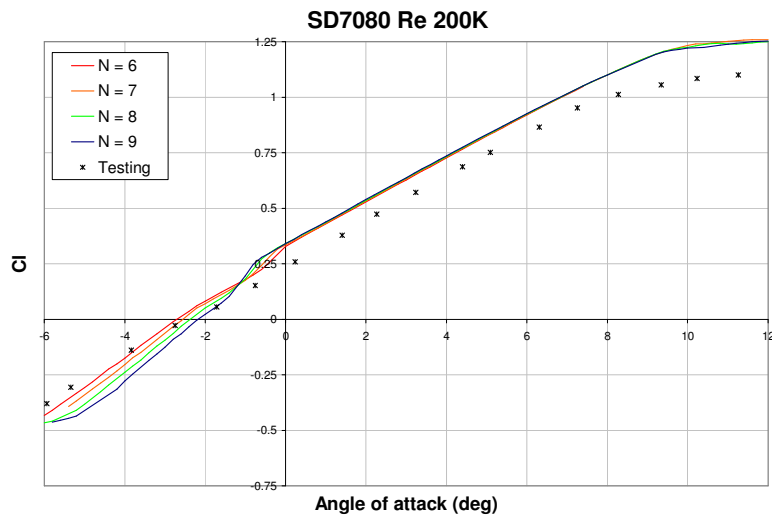
Figure 3.8: Ncrit Comparison: Lift, SD7080, Re = 200K

The trends associated with symmetric airfoils were used to proved XFOIL's ability to accurately predict changes in lift slope due to the presence of large laminar separation bubbles. For the NACA0009 airfoil, which is known to exhibit a non-linear lift curve due to laminar separation bubble effects, XFOIL accurately predicts the change in lift slope for all Re numbers. The changes in lift slope predicted by XFOIL appear to be more sever than the experimental data for higher Ncrit values. At a Re number of 200,000, Ncrit = 9 predicts a

drastic change in slope when only a minor change is present. Figure 3.9, Figure 3.10, and Figure 3.11 presents results for Re = 60,000, 100,000, and 200,000 respectively.
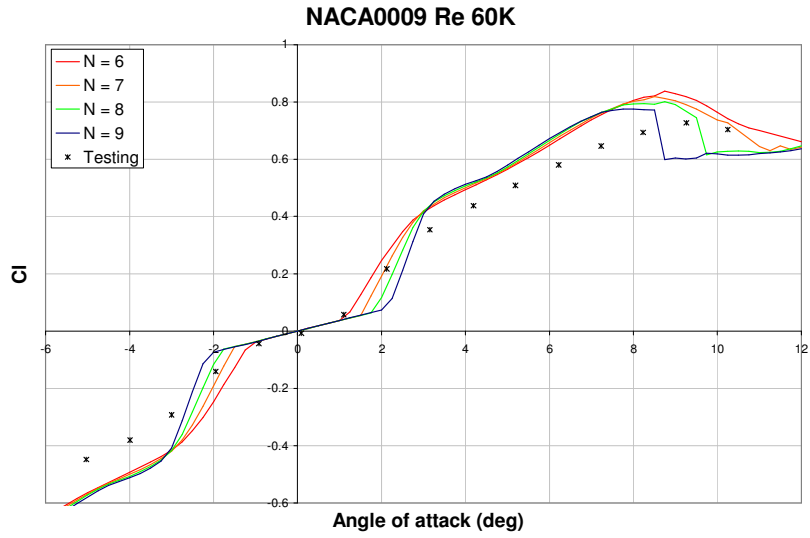
Figure 3.9: Ncrit Comparison: Lift, NACA0009, Re = 60K
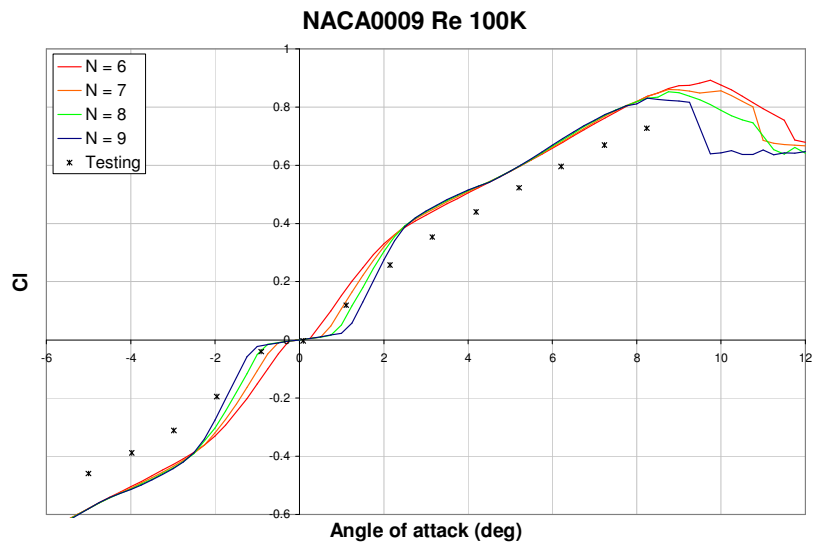
Figure 3.10: Ncrit Comparison: Lift, NACA0009, Re = 100K
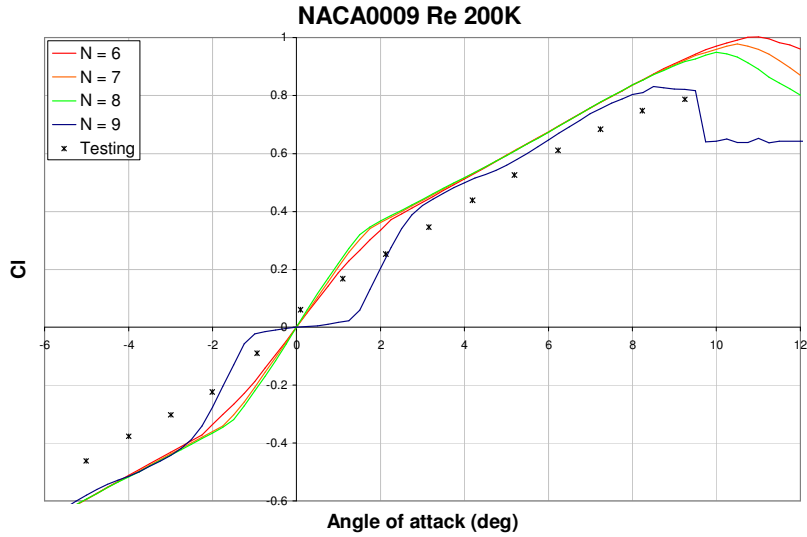
Figure 3.11: Ncrit Comparison: Lift, NACA0009, Re = 200K

The prediction trends associated with drag follow similar patters as lift. As Re number increases Ncrit dependence decreases and trend matching increases. The region of constant low drag, generally referred to as the *drag bucket*, is accurately predicted by XFOIL. Both the length, location, and any irregular features in experimental results for the drag bucket are paralleled by XFOIL results. Examples of these trends are presented in Figure 3.12, Figure 3.13, and Figure 3.14.

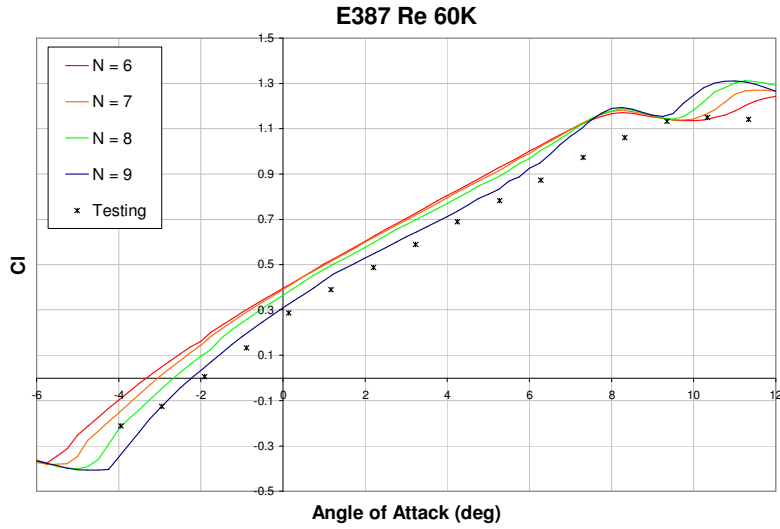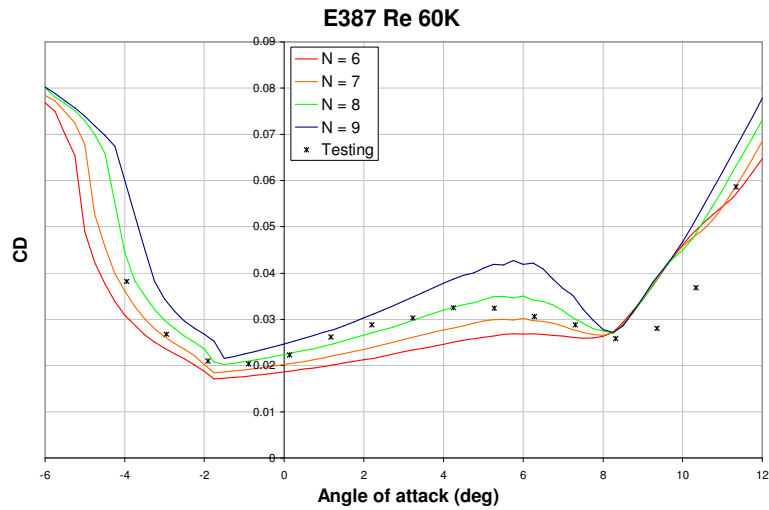**Figure 3.12: Ncrit Comparison: Drag, E387, Re = 60K**
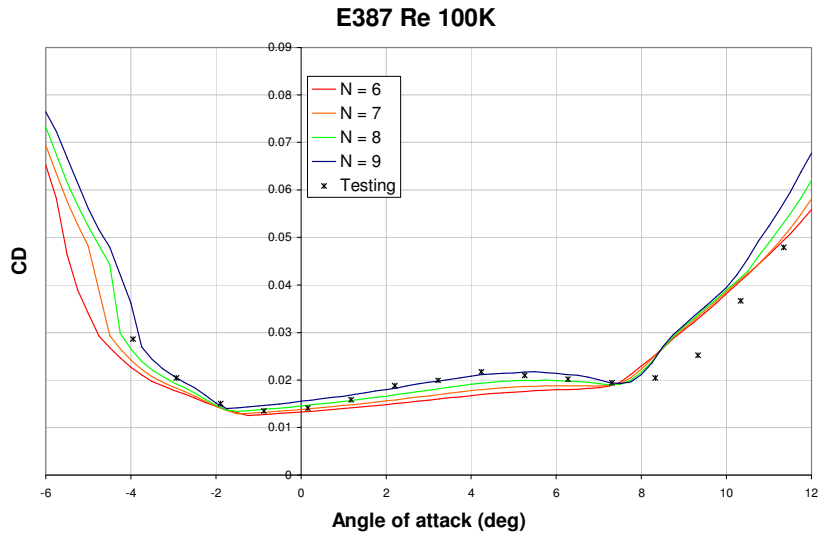
Figure 3.13: Ncrit Comparison: Drag, E387, Re = 60K
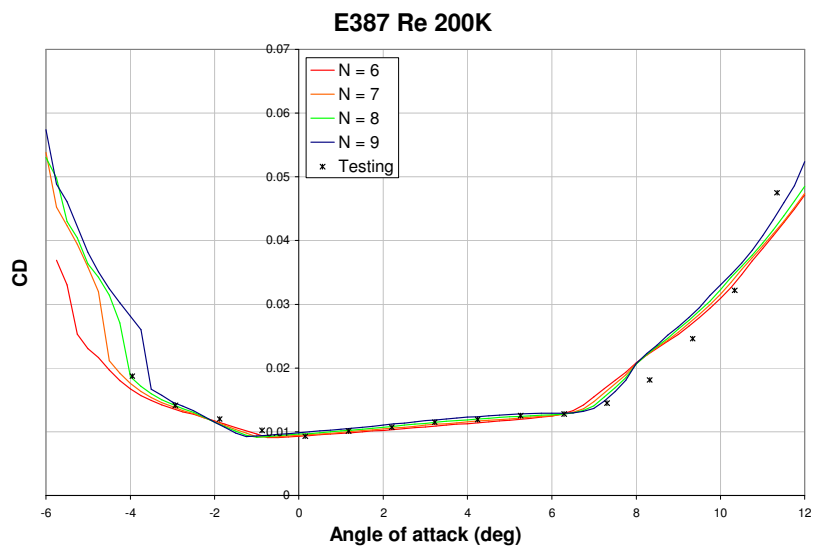
Figure 3.14: Ncrit Comparison: Drag, E387, Re = 200K

It was concluded from the average least squares regression analysis and the comparison study that XFOIL is adequate for low Re number analysis and has reliable trend prediction capability for Re numbers of 60,000 and above.

3.2 Expect

Understanding that a large number of airfoils would need to be analyzed using XFOIL during the course of this research, a bridge between the command line user interface of XFOIL and an automated interface driven by a predetermined logic structure was required.   A straightforward tool called Expect, built upon the Tool Command Language (Tcl), was designed specifically to interact with command line driven programs. Expect allows for implementation of a simple logic structure that goes well beyond feeding a preset sequence of commands into XFOIL.   Expect turned over 200 hours of laborious XFOIL user interaction into an overnight user free process.

3.2.1 Background

The foundation of Expect's usefulness is built on three basic commands, Spawn, Send and Expect. Spawn opens an program for interaction with expect. The expect command looks for a pattern match between a user defined string and the program's output. Send feeds a user defined string to the program's command line. Expect and send can be coupled to perform a predetermined action upon a specific program output. Additional functionality, such as *if-then* logic structure, logic tests, and mathematical operations are provided by the underlying Tcl language.   This combination allowed for a script that has versatility in application and error handling capabilities.

3.2.2 Script

The Expect script used to collect the data presented herein was Expfoil_V4.tcl, and is presented in Appendix C for reference. The script employs a simple iterative loop structure to sequence first through airfoils, then Re number, and then angle of attack. The geometric, method, and solution variables discussed previously are all set prior to staring the iterative loop. A number of procedures are set that contain common actions for use throughout the

51

script. Global variables are used in order for the procedures as well as the main body of code to share variable values.

The script has a number of built in functions worth nothing without a detailed description. The airfoils names, used to load the airfoil coordinate files into XFOIL, are read from the file AirfoilNames.out generated by the same MATLAB function that creates each airfoil coordinate file. For each airfoil and Re number a unique polar data file is created that follows the naming convention; Airfoil name_Re number_N crit_X_P. For example, BEZ031528020_Re200K_N7_X_P is the polar file for the BEZ031528020 airfoil, at a Re number of 200,000, and using a N_crit value of 7. The X means the data was collected by XFOIL, and the P means it is a polar file. A similar naming convention is used in defining the boundary layer (BL), shape parameter (H), and coefficient of pressure (CP) files. These three parameters are defined for each converged angle of attack, but only recorded for user defined angles of attack. The naming convention for these three files follow the form; Airfoil name_Re number_N crit_Angle of attack _X_BL/CP/H. Where BL/CP/H will signify the type of data file it is.

The most common nonconformity that the script must overcome is a non-converged solution. XFOIL's solution method relies on the values in the solution matrix to be the converged solution values; however that is not the case when a converged solution is not obtained. In order to eliminate the possibility of error being introduced from the non-converged solution matrix it is initialized prior to continuing to the next solution. This solution method achieved a high convergence level with minimal additional computational time. There are also cases where XFOIL does not converge and locks where no further user inputs are accepted. There are a number of output patterns that are indicative of such a case and the script is defined to detect them and reset the analysis. After XFOIL is reset, the script reloads all variables to return to the exact point where XFOIL locked and then it follows the same procedure as in the case of a simple non-converged angle of attack.

3.2.3   Validation

In order to ensure that the script was in fact producing the same output as a user would, a comparison of the output from the script and a human interaction session was performed. The results for a BEZ031517510 airfoil at a Re number of 60,000 were compared and showed no difference in any recorded polar values. A plot of Cl vs. α is presented in Figure 3.15 as an example of the data collected.
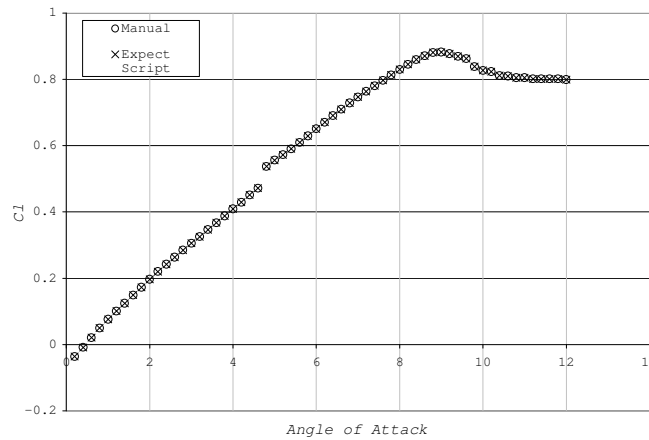
Figure 3.15: EXPECT Script Validation

3.3   Data Processing

The vast amount of data required automating the process of finding and recording the $C_{l,max}$, α_{stall}, $C_l/C_{d,max}$, and $\alpha_{Cl/Cd,max}$. This was done using a series of MATLAB functions and scripts to convert the XFOIL formatted polar, boundary layer, C_p, and H files into simply formatted data files that could be called and read into MATLAB. Additional checks were implemented to eliminate the possibility of misnaming data files. All MATLAB code covered in this section if presented in Appendix C.

3.3.1 Data File Format

The results of the final XFOIL analysis were 1,296 polar files containing angle of attack, lift, drag, moment, and upper and lower boundary layer transition data. Also 35,000 boundary layer, C_p, and H files were created. Each file was saved as a *.txt file following the naming convention outlined in Section 3.2.2. The file was formatted with the data appearing in tab delimitated columns with the airfoil name, Re number, Ncrit, and other specific information appearing in a section before the start of the data. Text headings outlined the content of each column. A MATLAB script was used to convert each file into simple space delimitated columns with no text headings. This allowed for the MATLAB function *load* to be used to accesses the data from each file quickly and simply. The process was computationally time consuming but saved significant time when accessing the data for evaluation. The resulting data files did not contain any descriptive information about what each column contained so a simple key was generated to describe the data in each column. The key used was associated with the last section of the file name, P, BL, CP, or H. The MATLAB functions that performed these tasks were SavePolarData_x_V3.m, SaveBLData_X.m, SaveCPData_X.m, and SaveHData_X.m, which are presented in Appendix C.

3.3.2 Verification

The primary check implemented was with the polar data conversion to ensure that all anticipated polar files were present. If any polar files were missing the airfoil number and the corresponding Re number were output for re-evaluation using the Expect script in XFOIL. A similar check was not applied to the BL, CP, and H files because missing files were anticipated due to unconverged angle of attack. Any missing files were still recorded and presented in a vector list in the MATLAB workspace.

Verification of the variables used by XFOIL for the analysis and the anticipated variables was performed for each data file. The data contained in the heading section of the files, airfoil name, Re number, Ncrit value, etc., was compared to the data file name to ensure the

specified data matched the intended analysis variables. If any discrepancies were found a vector containing the data file's name was output to the MATLAB workspace. For the final analysis no discrepancies were found.

4 Airfoil Analysis

The first section of this chapter describes the issues related to data quality and analysis. In addition, unanticipated lift curve behavior is addressed. The second and third sections present the results for $C_{l,max}$, α_{stall} and $C_l/C_{d,max}$, $\alpha_{Cl/Cd,max}$ respectively. The relationships between the different airfoil shape parameters and the performance results are emphasized. The fourth section suggests a design methodology utilizing the results of the analysis. The final section presents general conclusions of the analysis.

4.1 Data Assessment

The potential for unconverged solutions and variations in data quality throughout the range of files created required a detail assessment of the data collected. An evaluation of each data set for a specific group of requirements was performed prior to using the data to form results. The requirements limit the number of unconverged angles of attack that can occur sequentially and test the data in the vicinity of $C_{l,max}$ and $C_l/C_{d,max}$ to ensure these values were properly reported.

4.1.1 Unconverged Angle of Attack

Not all airfoil polar data files were complete. For certain airfoils, Re numbers, and angles of attack XFOIL was unable to achieve a converged solution. In these cases, C_l and C_d performance data was not generated, which created the potential for inaccurate data evaluation. The two major concerns were large gaps in data that may span the region of anticipated peak $C_l/C_{d,max}$ performance and truncated data that prevents accurate $C_{l,max}$ assessment. Short frequent gaps in polar data are not a concern because the angle of attack

step size, 0.2°, is much smaller than required to resolve the lift and drag polars. Figure 4.1 presents a flow chart of the method described.

Large gaps in data were measured by comparing the anticipated angle of attack sequence to the recorded angle of attack sequence of each polar file. If the largest gap in angle of attack was greater than 2° and occurred prior to $C_{l,max}$, the data was rejected. Gaps in angle of attack greater than 2° can have significant effects on portions of the drag polar that are not linear. During preliminary analysis large gaps in data were common but as XFOIL's convergence level increased the number of gaps larger than 2° were greatly reduced.

Truncated data refers to cases where XFOIL was unable to obtain a converged solution beyond a certain angle of attack. If the last converged angle of attack is less than α_{stall}, $C_{l,max}$ and $C_l/C_{d,max}$ may be reported incorrectly. If the maximum converged angle of attack is determined to be less than α_{stall}, the data is rejected. A description of how stall α_{stall} was determined is presented in the following section.

Truncated data and data with large gaps resulted in rejection of 9.5% of the data files recorded during the final analysis. Of the 9.5%, there was no noticeable trend in any airfoil shape parameter or Re numbers that could be responsible for a poor convergence level. This amount of unconverged data was expected due to the trade offs required for a timely solution.
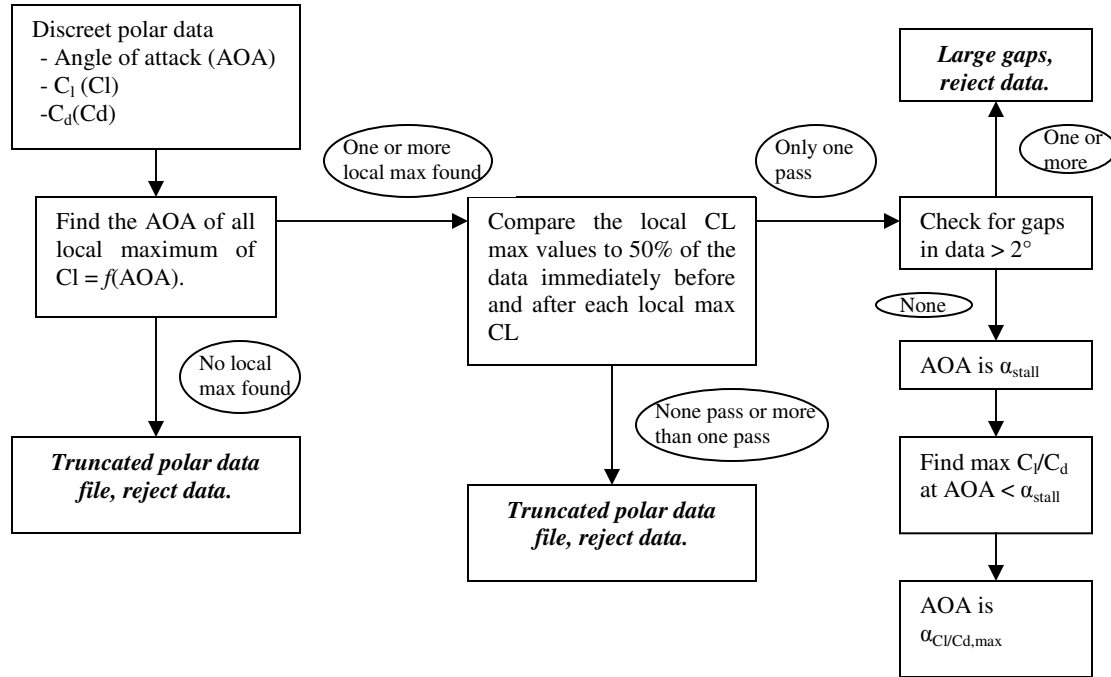
Figure 4.1: Data Evaluation Flow Chart

4.1.2 $C_{l,max}$ and α_{stall}

$C_{l,max}$ was not simply defined as the maximum C_l value attained for the range of converged angle of attack , but as the C_l value corresponding to the airfoil's stall angle of attack. This method was required because XFOIL's post stall predictions of C_l are unreliable and often spike to values larger than $C_{l,max}$. This trend is clear in Figure 4.2. Stall is evident at 7.8° with expected post stall behavior up to 8.8°. After 8.8° large regions of fully separated flow dominate the upper surface of the airfoil and XFOIL's predictions lose meaning.
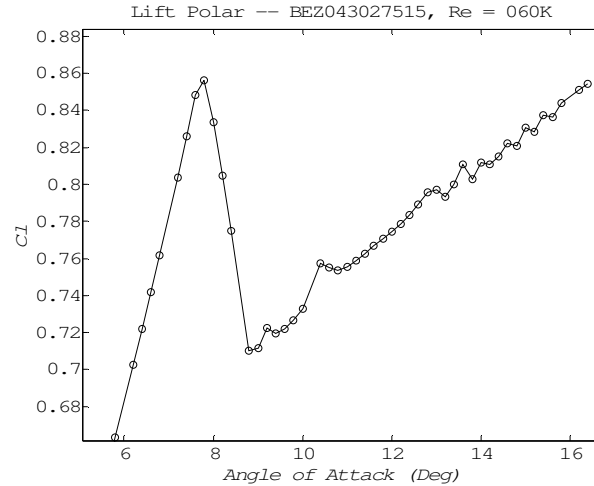
Figure 4.2: Example C$_l$ Plot

An airfoil has stalled when lift production decreases and drag increases with increasing angle of attack. Minor oscillations and nonlinearities in C$_l$ can result in several locations of apparent stall when taking a numerical differentiation. In order to eliminate any minor oscillations from being identified as the stall point, each local maximum was compared to a portion of C$_l$ values immediately before and after a potential C$_{l,max}$. Evaluation of 50% of the C$_l$ values before and after a local maximum ensured that the reported C$_{l,max}$ was not due to minor oscillations or effected by oscillations in post stall C$_l$. Each C$_l$ value in the evaluated range must be less than the local C$_l$ for the point to be identified as C$_{l,max}$. The function used to implement this method in MATLAB also had the advantage of limiting the range of α_{stall} and C$_{l,max}$ between 5 points from the lowest and highest converged angle of attack. This acted as a catch for any truncated data that may have oscillations or a minor dip at the maximum converged angle of attack.

To measure the potential range of α_{stall}, the converged angles of attack before and after stall were evaluated. This range of potential values is due to the discreet nature of the data. The difference between the two angles represents a value similar to the least count of a measurement device. The smallest value that the difference could be is 0.4°, which is twice the angle of attack step used by XFOIL to calculate the data. The average range of α_{stall} due to unconverged angle of attack data was found to be 0.6°.

4.1.3 $C_l/C_{d,max}$ and $\alpha_{Cl/Cd,max}$

Determining $C_l/C_{d,max}$ relied on a simple evaluation of the maximum C_l/C_d value. Figure 4.3: Example C_l/C_d Plot shows an example of a standard C_l/C_d vs. α plot where the global maximum is clear. Any post stall behavior is eliminated by only addressing the angles of attack less than α_{stall} when finding $C_l/C_{d,max}$.
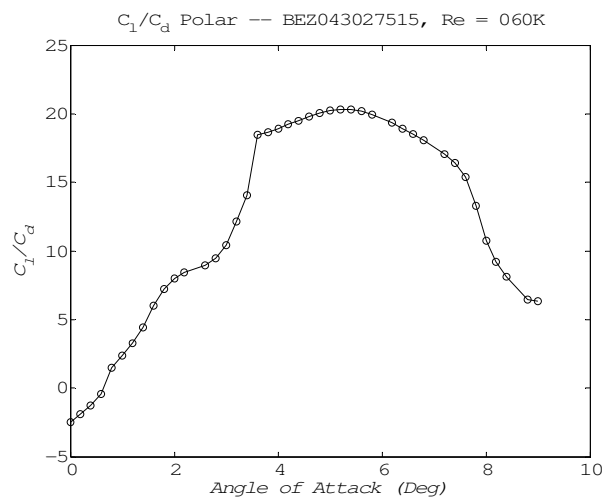
Figure 4.3: Example C_l/C_d Plot

The potential range of angle of attack for $C_l/C_{d,max}$ was calculated in the same way as stall angle of attack. The average difference was 0.5°, which is only slightly greater than the minimum of 0.4° representing a good level of convergence near the angle of attack of $C_l/C_{d,max}$.

4.1.4 Lift Polar

During the preliminary analysis of the Bezier airfoils a substantial non-linearity in C_l vs. angle of attack was consistently recorded. A slight bump due to laminar separation bubble effects was predicted by Gad-El-Hak for low Re numbers, however the magnitude of the

non-linearity seen during preliminary analysis was much larger than Gad-El-Hak's predicted. The non-linearity was similar to what was seen during testing of semi-circular airfoils by Jenkins et al. (1998). Figure 4.4 shows a typical jump in C_l for a BEZ053017515 airfoil at a Re number of 150,000. Upon further investigation it was found that XFOIL's prediction of the drastic change in slope occurred at different locations for increasing and decreasing angle of attack. The change in location is shown in Figure 4.5. Investigation of a NACA0009 airfoil at a Re number of 60,000, which XFOIL predicts will have a small bump in C_l, showed no change in bump location for increasing and decreasing angle of attack. It was determined that the non-linearity present for Bezier airfoils could not be entirely due to laminar separation bubble effects on the upper surface of the airfoil.
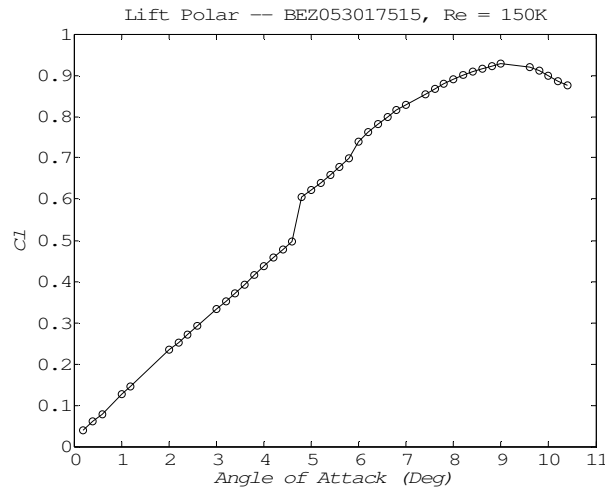
Figure 4.4: Typical Jump C_l
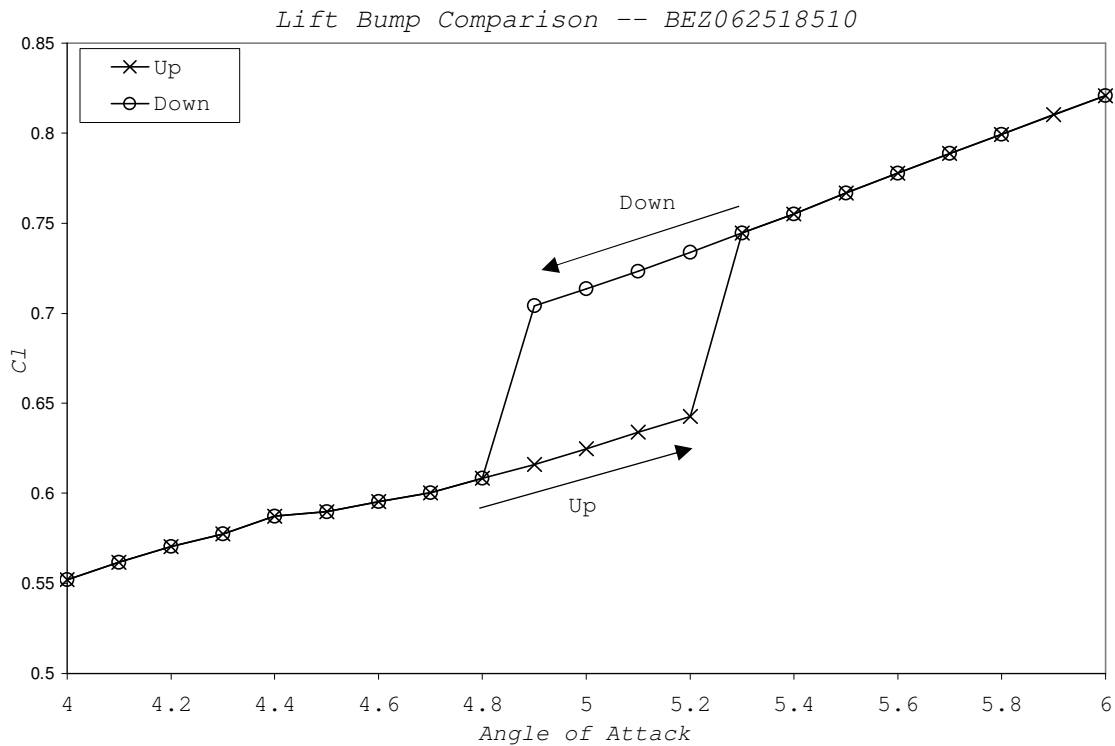
Figure 4.5: Jump in C$_l$ for Increasing and Decreasing Angle of Attack

The change in location of the jump was critical in understanding why the jump occurred. For low angles of attack the lower surface of a Bezier airfoil has separated flow starting near the leading edge and reattaching at a point close to the trailing edge, depending on the airfoil and Re number. As angle of attack increases the separated boundary layer region has a tendency to remain in a separated state. This tendency has been measured previously as stall hysteresis, present when a short laminar separation bubble burst and cannot reform when angle of attack is decreased (Gad-El-Hak 1989; Boreren, Bragg 2001). Once the angle of attack reaches a critical value, the boundary layer on the lower surfaces transitions from partially separated to fully attached. This is a function of the concaved lower surface shape of Bezier airfoils and also the semi-circular airfoils tested by Jenkins et al. (1998). Once the lower surface boundary layer becomes attached, C$_l$ experiences a significant increase. When decreasing angle of attack the lower surface boundary layer has a tendency to remain attached, which results in the lift bump occurring at a lower angle of attack. This is because the attached lower surface boundary layer results in an increased C$_l$.

Figure 4.6 shows the upper and lower surface transition locations for BEZ043027515 at a Re number of 60,000 from 0° to α_{stall}. Figure 4.7 presents the corresponding C_l curve. Transition location refers to the point on the airfoil where XFOIL predicts that the flow will become turbulent. The increase in C_l performance coincides with the bottom surface transition location's jump to the trailing edge. The movement of the upper surface transition location from near 60% to less than 10% chord represents a transition from a large laminar separation bubble to a short leading edge bubble. This region coincides with the dip in C_l performance before the increase in C_l. The movement of the upper surface transition location forward before lower surface transition moves to the trailing edge causes a more pronounced increase in C_l. Figure 4.8 and Figure 4.9 present the transition plot and corresponding C_l plot for an airfoil exhibiting a small jump in C_l. Figure 4.8 shows how the upper surface transition location moves towards the leading edge after the lower surface transition location has moved to the trailing edge. The effect is apparent in the minor dip in C_l that occurs after the increase in C_l. The jump in C_l is smaller because the dip did not occur before the jump.
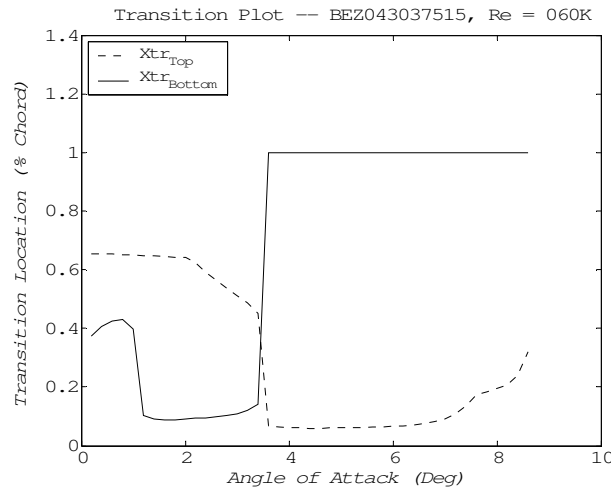
Figure 4.6: Transition Plot for Large Jump in C_l
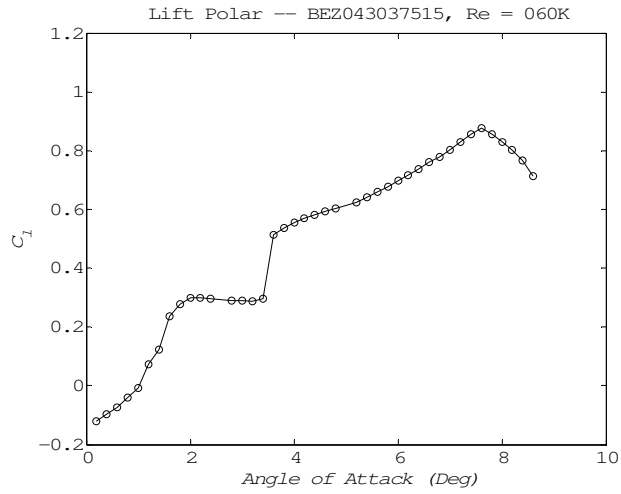
Figure 4.7: Example of Large Jump in C_l
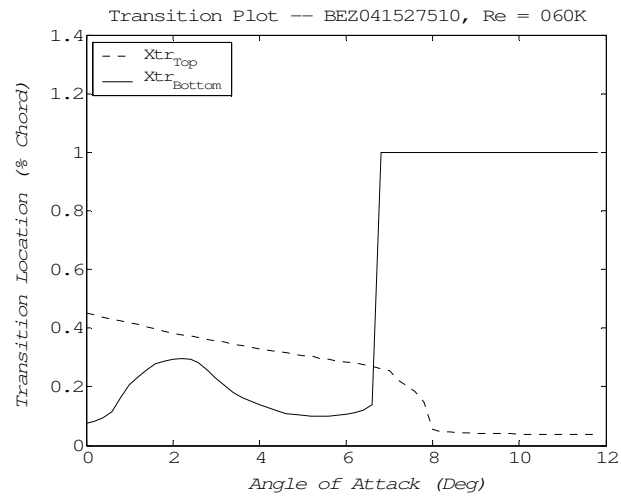
Figure 4.8: Transition Plot for Small jump in C_l
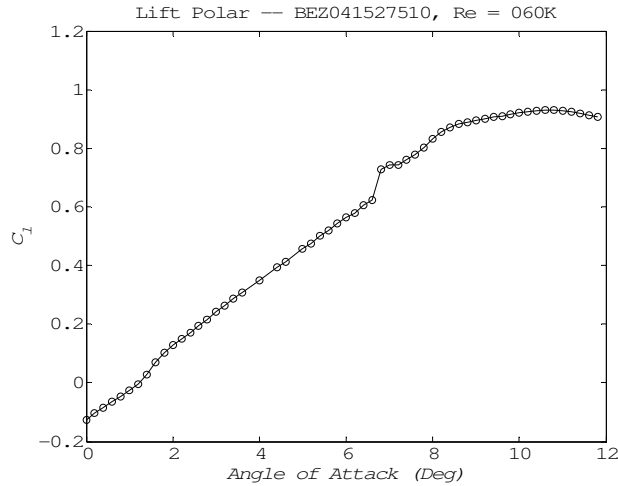
Figure 4.9: Example of Small Jump in C_l

4.2 Results: $C_{l,max}$ and α_{stall}

The $C_{l,max}$ value of an airfoil is a critical parameter in defining the slow flight and high lift characteristics of a MAV. High $C_{l,max}$ values allow for larger payloads and slower minimum flight speeds. α_{stall} is important in defining the operating range of angle of attack for the airfoil, with high α_{stall} expanding the range of operable angle of attack. The following sub-sections will address the effect each airfoil shape parameter has on $C_{l,max}$ and α_{stall}. Simplified plots are presented that represent the general trends seen throughout the data as well as highlight any anomalies in the results.

4.2.1 Max Camber and Position of Max Camber

Max camber (c) and location of max camber (xC) were found to have a strong effect on maximum lift production, which is consistent with previous findings. A comparison of $C_{l,max}$ values for various different cambered Bezier airfoils is presented in Figure 4.10, Figure 4.11, and Figure 4.12. For simplicity reflex (R), location of max reflex (xR), and thickness (T) were held constant at 1%, 80%, 0.1% chord respectively and $C_{l,max}$ results are presented for the different combinations of C and xC for three Re numbers. The plots were generated so

65

that data is not extrapolated and known data points occur only were 2 lines intersect. This convention is used consistently for this style of 3D plots. Figure 4.9 includes additional information to help interpret the plots.

C/xC Evaluation (R = 1, xR = 80, T = 0.10) Re = 60K
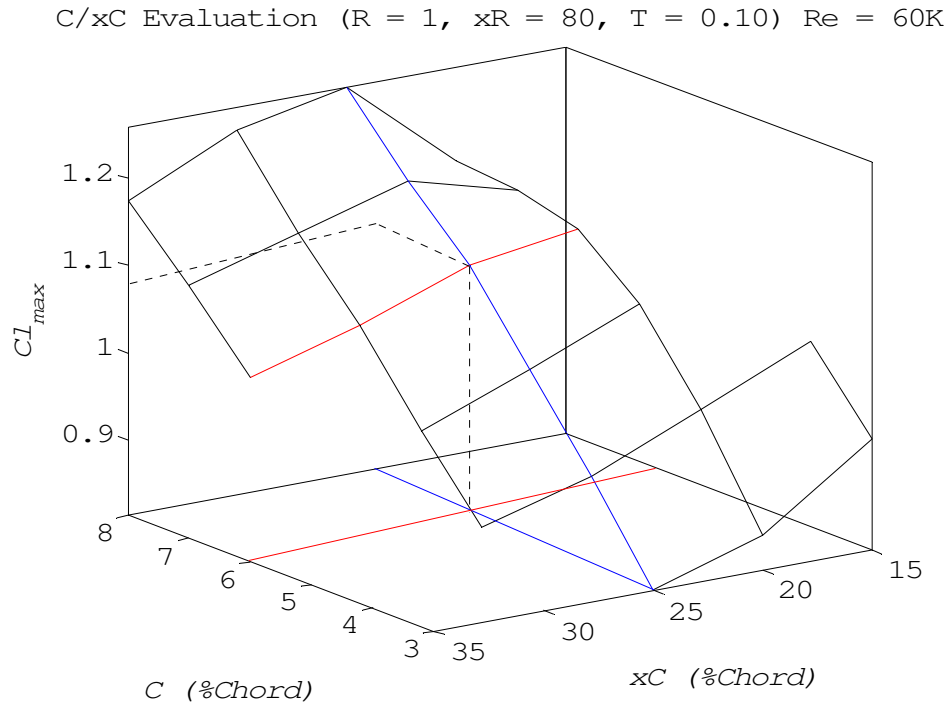
Figure 4.10: C/xC Evaluation: $C_{l,max}$ (R=1, xR=80, T=0.10, Re=60K)

C/xC Evaluation (R = 1, xR = 80, T = 0.10) Re = 100K
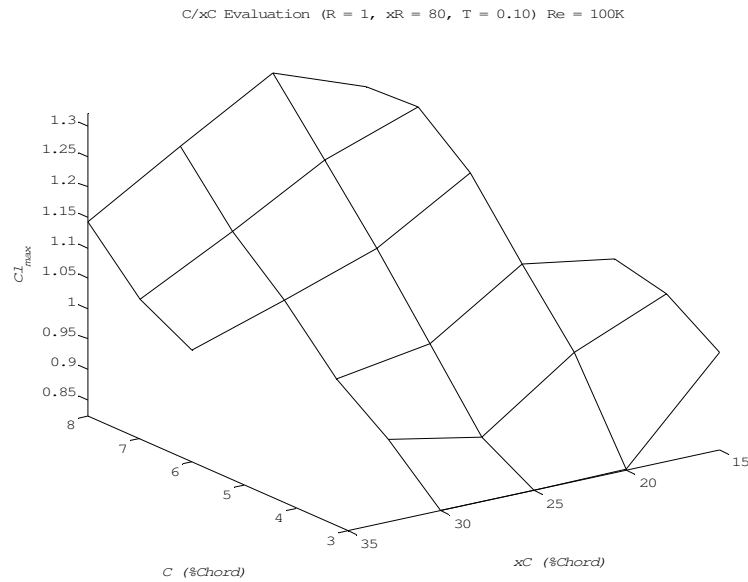
Figure 4.11: C/xC Evaluation: $C_{l,max}$ (R=1, xR=80, T=0.10, Re=100K)
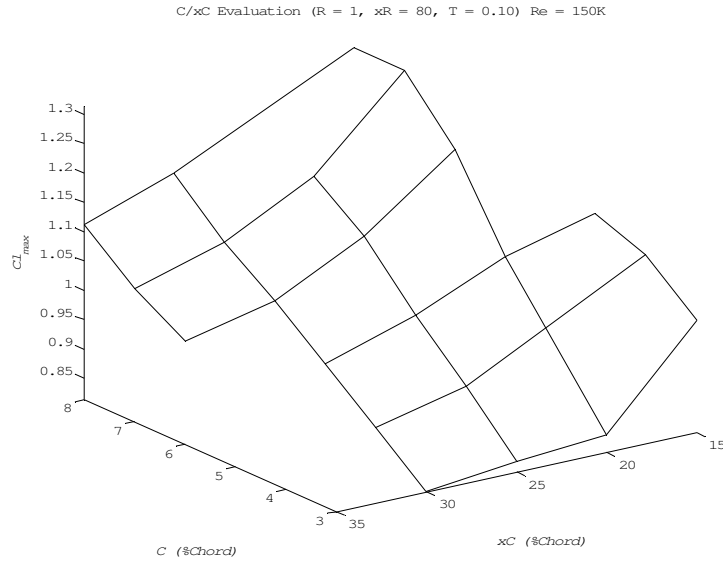
Figure 4.12: C/xC Evaluation: $C_{l,max}$ (R=1, xR=80, T=0.10, Re=150K)

Common to all three Re numbers is an increase in $C_{l,max}$ with an increase in C for xC values greater than 20% chord, with higher Re numbers exhibiting a more linear relationship. At and below 20% chord, lower Re numbers showed signs of degraded performance for increasing C values. For all but Re = 60,000, decreasing xC caused increases in $C_{l,max}$ with the gain becoming less as C increased and Re number decreased. For Re = 60,000, reducing xC below 25% for high C values caused a reduction in $C_{l,max}$. The decrease in performance for high C and low xC values was more severe for an xR value of 85%. This is an indication of a slight interdependence between C, xC, and xR. The three plots represent the trends associated with the majority of airfoils analyzed.

In order to isolate camber as the independent parameter of interest, xC, R, xR, and T were held constant while C and Re number were varied. Figure 4.13 shows the results for $C_{l,max}$ for six different camber values at three Re numbers for xC = 25%, R = 1%, xR = 85%, and T = 0.1% chord.
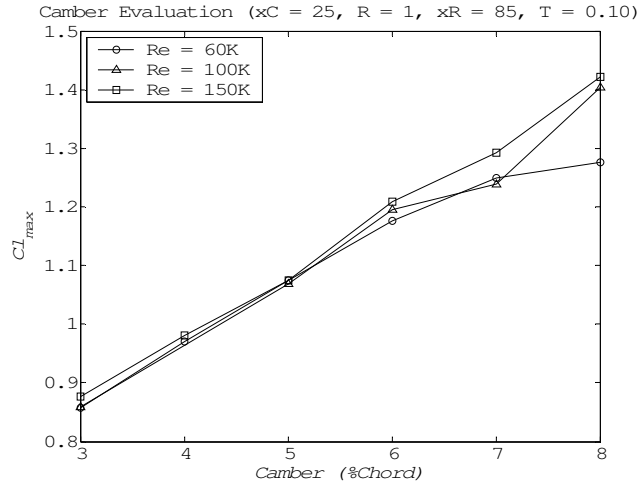
Figure 4.13: C/Re Evaluation: $C_{l,max}$ (xC=25, R=1, xR=85, T=0.10)

For Re numbers above 60,000, $C_{l,max}$ increases steadily as camber increases. For Re = 60,000, $C_{l,max}$ increases less as camber increases. This trend is more evident when xC is smaller. For xC = 20%, R = 1%, xR = 85%, and T = 0.1% chord, all three Re numbers exhibit less linear behavior with a growing discrepancy in $C_{l,max}$ for different Re numbers. Figure 4.14 shows this trend in $C_{l,max}$. This airfoil was chosen to identify the reason for the decrease in performance for high C low xC values.
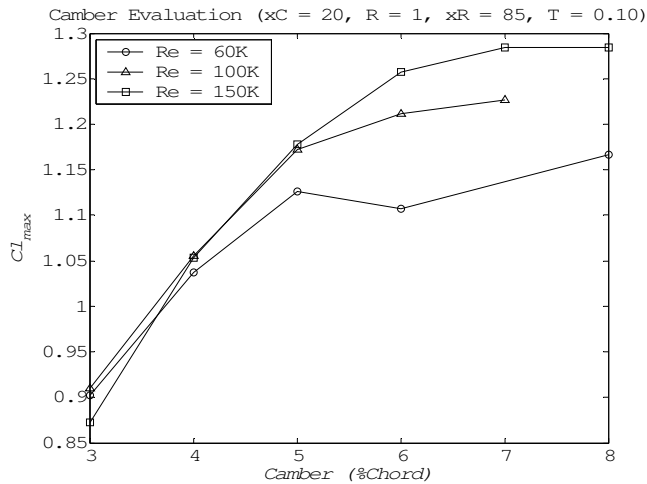
Figure 4.14: C/Re Evaluation: $C_{l,max}$ (xC=20, R=1, xR=85, T=0.10)

68

The upper surface boundary layer behavior is the cause of the linear and non-linear relationship between $C_{l,max}$ and max camber. The leading edge angle, defined by the slope of the MCL at the leading edge, increases with increasing camber and decreasing location of max camber. This change caused an increase in the angle of attack at which the transition location moves toward the leading edge. In Figure 4.15 the transition location moved to the leading edge at progressively higher angle of attack for increasing camber. For simplicity, only camber values of 5% thru 8% chord are presented in Figure 4.15. The movement of the transition location aft at higher angle of attack was found to be caused by laminar separation bubble growth. The presence of a laminar separation bubble in this region prevents flow from separating over the aft portion of the airfoil, allowing for increasing $C_{l,max}$ for higher camber values. In the case where xC = 20% chord the leading edge angle is increased, further retarding the transition point's movement toward the leading edge until higher angles of attack. Figure 4.16 shows that the transition point collapses to the leading edge at approximately 2° higher angle of attack for all camber values for the lower xC value. The higher angle of attack and increased curvature of the forward portion of the airfoil, due to the change in xC, prevents the short leading edge laminar separation bubble from expanding aft and causes the bubble to burst at the leading edge. This inhibits the airfoil from achieving attached flow at higher angles of attack which limits $C_{l,max}$. The transition curves in Figure 4.16 differ very little at higher angles of attack which corresponds to the similar $C_{l,max}$ values attained by the different camber values, and the reason for the curvature present in Figure 4.14.
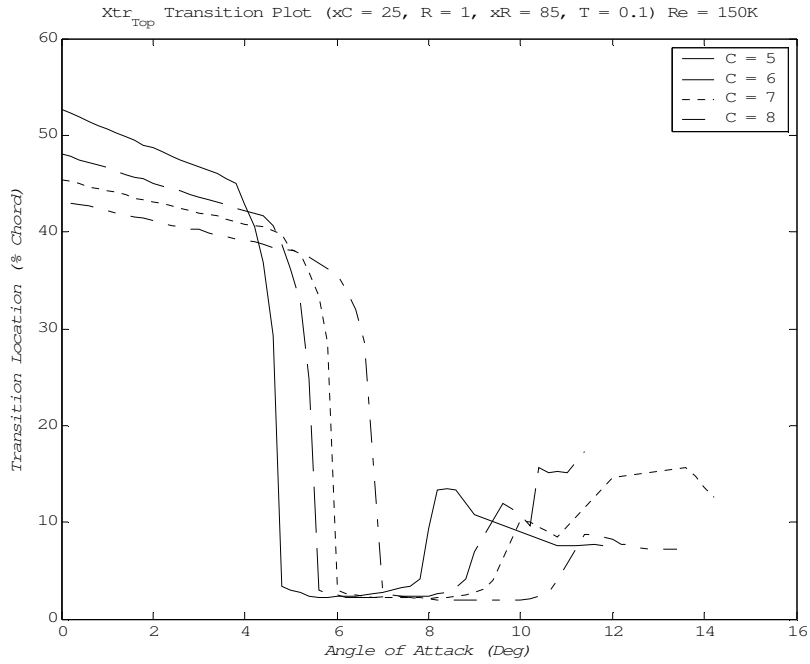
Figure 4.15: C Transition (xC=25, R=1, xR=85, T=0.10,Re=100)
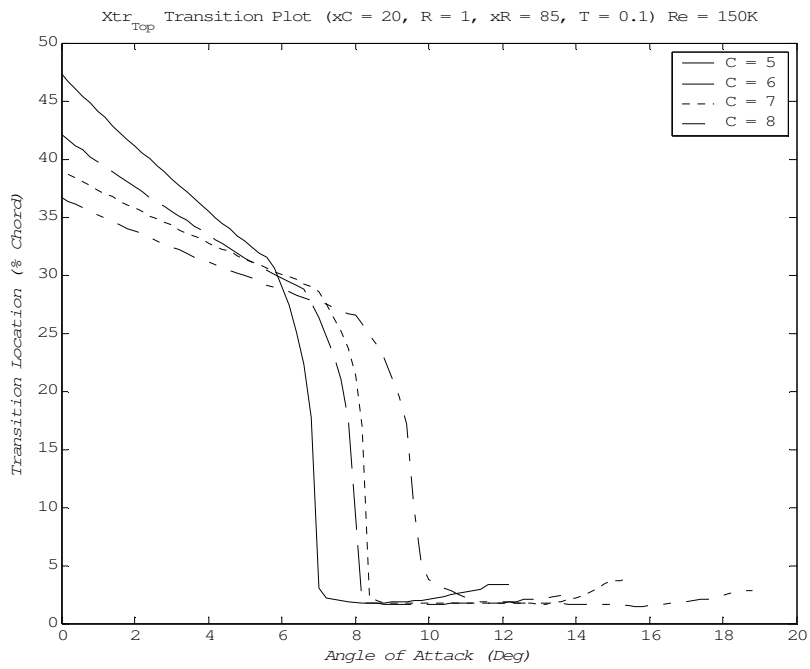
Figure 4.16: C Transition (xC=25, R=1, xR=85, T=0.10,Re=150)

The relationship between airfoil parameters C and xC and α_{stall} is complex. Figure 4.17, Figure 4.18, and Figure 4.19 show the dependency of α_{stall} on C and xC for Re numbers of 60,000, 100,000, and 150,000. As C and xC increase, α_{stall} increases, with the correlation most prominent at a Re number of 60,000. For Re numbers of 100,000 and 150,000 the relationship breaks down and becomes less linear. The significant increase in α_{stall} as xC decrease below 25% is common for a majority of the airfoils analyzed. The trend of increasing α_{stall} with increasing C occurred consistently at all Re numbers for a variety of R, xR, and T values.
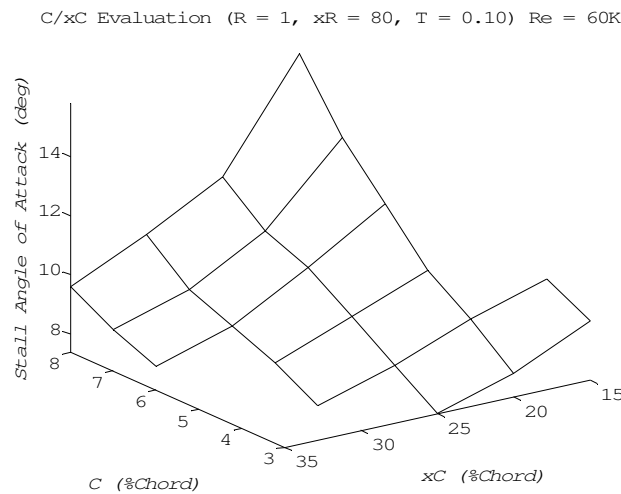
Figure 4.17: C/xC Evaluation: α_{stall} (R=1, xR=80, T=0.10, Re=60K)
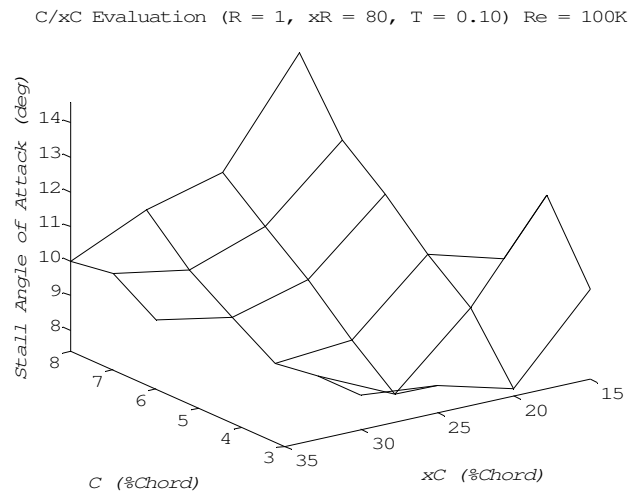
Figure 4.18: C/xC Evaluation: α_{stall} (R=1, xR=80, T=0.10, Re=100K)

C/xC Evaluation (R = 1, xR = 80, T = 0.10) Re = 150K
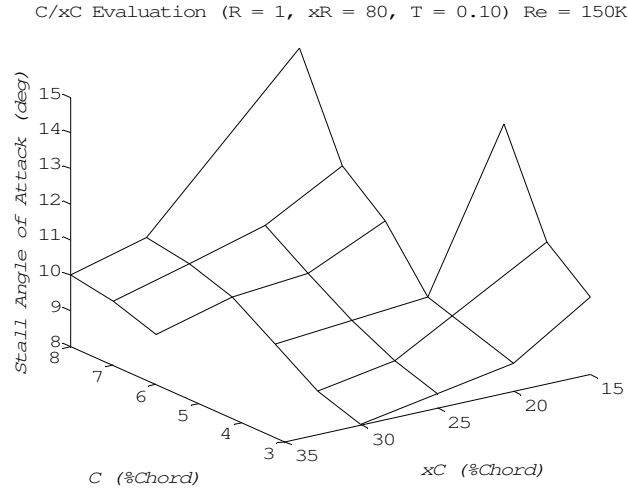
Figure 4.19: C/xC Evaluation: α_{stall} (R=1, xR=80, T=0.10, Re=150K)

Stall angle of attack exhibits a direct relationship with C and xC. As discussed previously, increases in C and decreases in xC cause an increase in leading edge angle, which delays stall. The relationship between the airfoil shape parameters, C and xC, and stall angle of attack does not break down for large leading edge angles in the same way as $C_{l,max}$. Figure 4.20 and Figure 4.21 show the stall angle of attack for the same airfoil shape parameters presented as examples for $C_{l,max}$. For xC = 25%, α_{stall} progressively increases as C increases with Re = 60,000 showing a tendency to stall at higher angles of attack. This trend is due to the formation of short leading edge laminar separation bubbles at lower Re numbers that prevent separation over the aft portion of the airfoil by acting as a boundary layer transition mechanism.
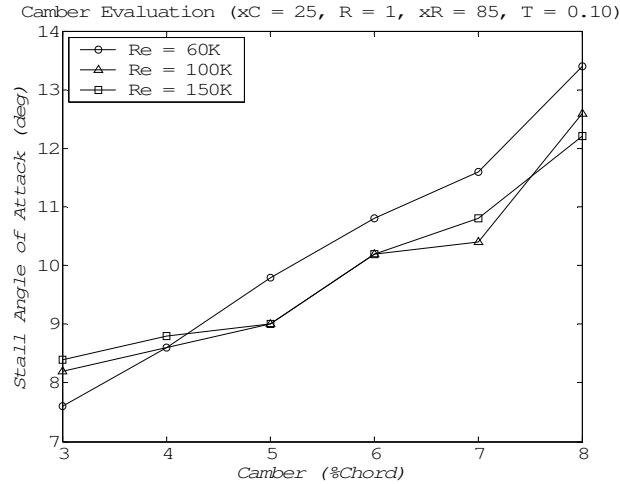
Figure 4.20: C/Re Evaluation: α_{stall} (xC=25, R=1, xR=85, T=0.10)
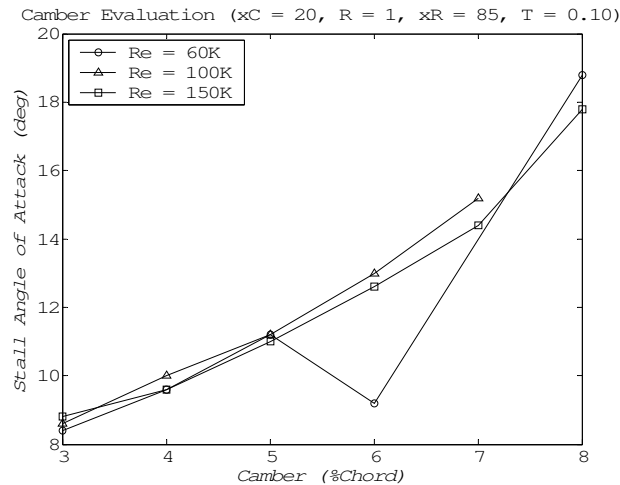
Figure 4.21: C/Re Evaluation: α_{stall} (xC=20, R=1, xR=85, T=0.10)

In Figure 4.21 the same increasing trend in α_{stall} is present, with the exception of 6% camber at Re = 60,000. The 6% camber airfoil exhibited premature stall at lower Re numbers. The premature stall at Re = 60,000 is due to the tendency of the turbulent boundary layer aft of the leading edge laminar separation bubble to separate. The boundary layer over the aft surface of the airfoil at higher Re numbers is able to remain attached and achieved a higher stall angle of attack. The dependence on Re number is not present at higher camber values because the increased curvature prevents any large regions of attached flow aft of the leading edge laminar separation bubble for all Re numbers.

4.2.2   Max Reflex and Position of Max Reflex

Max Reflex was found to have a minimal affect on $C_{l,max}$ performance where as the location of max reflex and $C_{l,max}$ exhibited a direct correlation. Plots of $C_{l,max}$ for different R and xR values at constant C, xC, and T values of 5%, 25%, and 0.1% respectively are presented in Figure 4.22, Figure 4.23, and Figure 4.24. The three figures address the range of Re numbers analyzed.
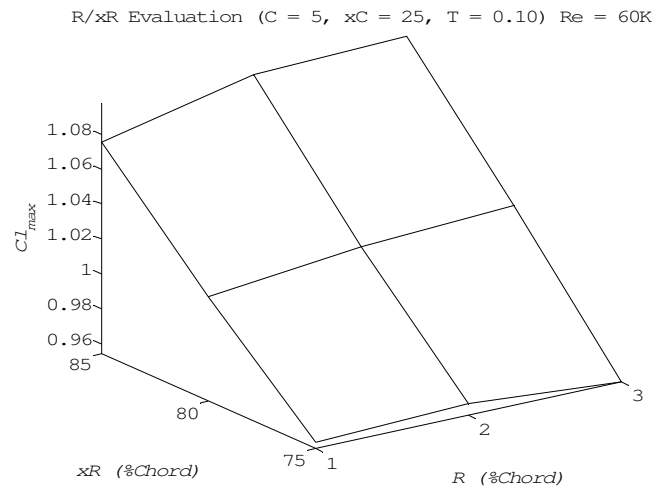
Figure 4.22: R/xR Evaluation: $C_{l,max}$ (C=5, xC=25, T=0.10, Re=60K)
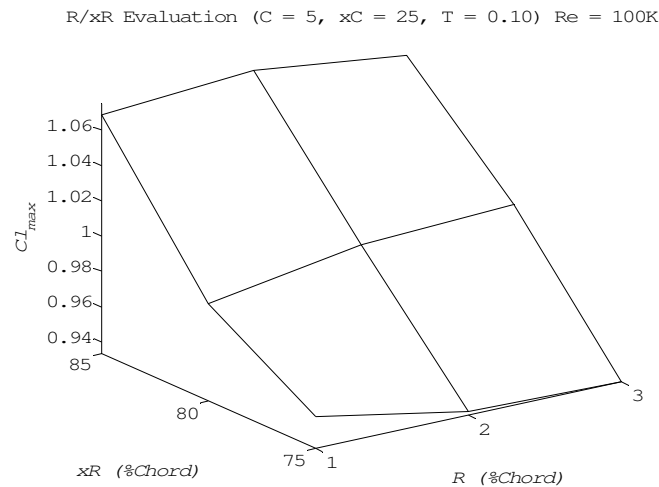
Figure 4.23: R/xR Evaluation: $C_{l,max}$ (C=5, xC=25, T=0.10, Re=100K)
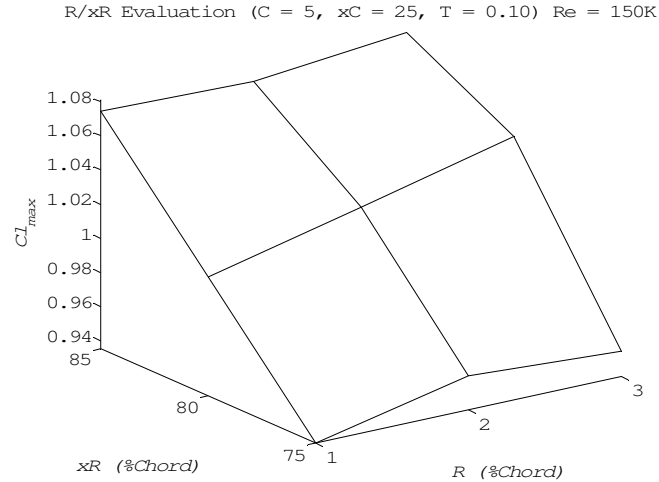
Figure 4.24: R/xR Evaluation: $C_{l,max}$ (C=5, xC=25, T=0.10, Re=150K)

All three Re number plots exhibit similar responses to changing R and xR values. Increases in xR cause an increase in $C_{l,max}$ for all R values and Re numbers. The magnitude of the change in $C_{l,max}$ due to xR is much less than what was caused by changes in C and xC. No significant change in $C_{l,max}$ was found for increasing R values at any Re number.

To determine the reason for the strong connection between $C_{l,max}$ and xR and the weak connection between $C_{l,max}$ and R, plots of the upper and lower surface pressure distributions were studied. The pressure distribution plots were studied because the primary reason for adding reflex to an airfoil is to shift the pressure distribution aft affecting the pressure recovery region. The affects of changes in R and xR were evaluated independently at Re = 60,000 for C, xC, and T values of 5%, 25%, and 10% chord respectively. Coefficient of pressure (C_p) was recorded every 2° angle of attack during the analysis. The stall angle of attack was slightly above and below 9° angle of attack for all cases. To eliminate the possibility of comparing pre and post stall C_p behavior, all evaluations were performed at 8° angle of attack.

The change in C_p due to variation of R, shown in Figure 4.25, is minor and localized to the aft 60% of the upper surface of the airfoil. The upper surface C_p distribution is shown as a dotted line and the lower surface C_p as a solid line; this convention is constant throughout.

75

The difference between top and bottom surface C_p distributions over the aft 35% of the airfoil grows with an increase in reflex. The change between the upper and lower C_p values for this region is greater for the change from R = 1 to 2 than it is for R = 2 to 3. This is an indication that increasing R has a diminishing effect on the pressure distribution and subsequently $C_{l,max}$. The decrease in top surface Cp values over the aft 35% of the airfoil is offset by an increase in top surface C_p values for the region between 30% and 60% chord for increasing R, causing only a minimal effect on overall C_l performance. This was due to the increased curvature in the region for larger R values.
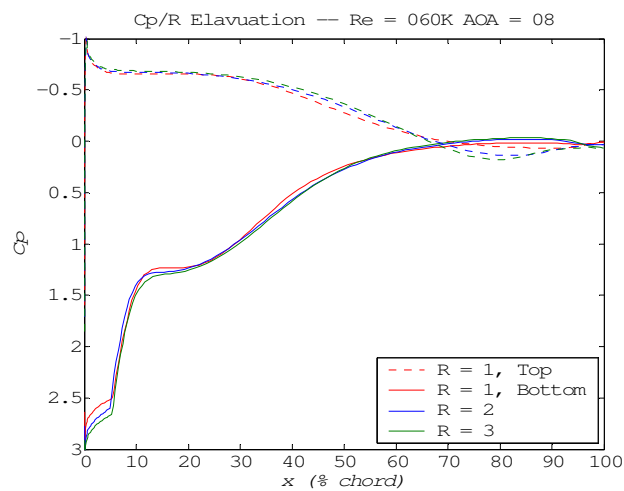
Figure 4.25: Cp/R Evaluation (Re=60K, α=8°)

Figure 4.26 shows the effect changes in xR have on the C_p distribution. Unlike R, changes in xR effect the C_p distribution of both the upper and lower surfaces. Decreasing xR causes the difference between the C_p distribution on the top and bottom to diminish over the range of 35% to 75% chord. This trend is due to the shift in airfoil curvature forward. The shift in curvature causes the pressure recovery region between 40% and 80% chord to transition from concaved to convex. The concaved pressure distribution is closer to the ideal case of a Stratford pressure distribution for high lift airfoils causing higher $C_{l,max}$ (Selig, Guglielmo 1997).
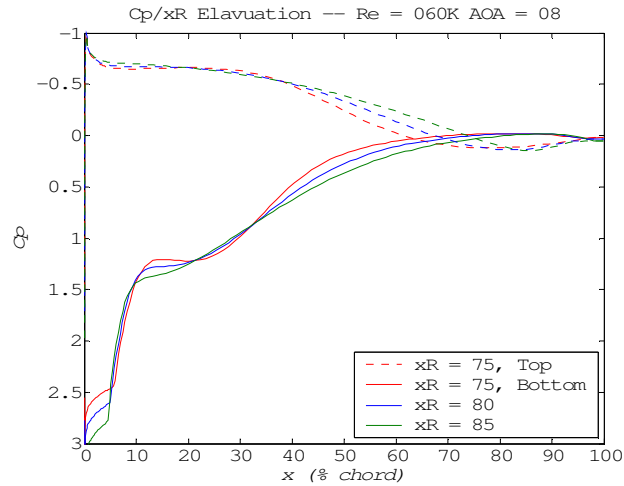
Figure 4.26: Cp/xR Evaluation (Re=60K, α=8°)

No relationship between R or xR and α_{stall} was found. Figure 4.27 represents the distribution of α_{stall} over the range of R and xR values, which is common for all C, xC, and Re numbers. Compared to the mean anticipated range of 0.6°, covered in Section 4.1.2, there was no appreciable difference in α_{stall} for different R and xR values.
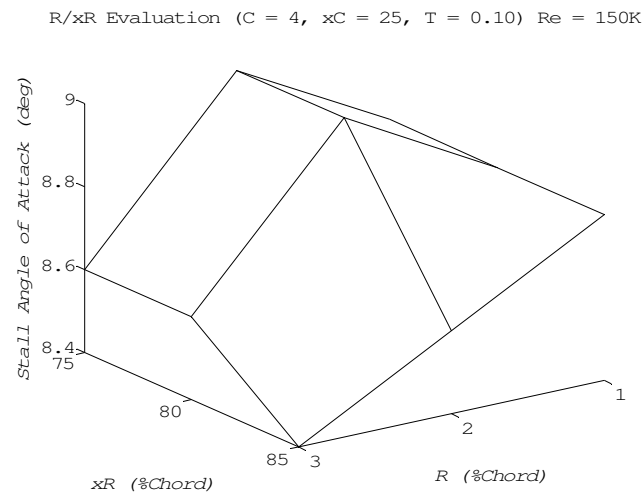
Figure 4.27: R/xR Evaluation: α_{stall} (C=4, xC=25,T=0.10, Re=150K)

4.2.3 Thickness

A change in thickness from 1% chord to 1.5% chord did not cause a change in any of the performance trends for $C_{l,max}$ or α_{stall} described in the previous sections. An increase in thickness does cause a slight increase in the magnitude of $C_{l,max}$ and α_{stall} for a majority of the airfoils analyzed. The increase of $C_{l,max}$ and α_{stall} is caused by a subtle change in the boundary layer behavior near the leading edge. The change is due to the larger leading edge radius which causes any leading edge laminar separation bubbles that form to be shorter. Figure 4.28 shows the pressure distribution for both thickness values at C = 5%, xC = 25%, R = 1% and xR = 85% chord. The data is presented for an angle of attack of 10°, which is the stall point for the 1% thick airfoil and 0.4° less than α_{stall} for the 1.5% thick airfoil. The region of relatively constant C_p for the lower surface signifies the presence of a laminar separation bubble. For T = 1.5% the region of constant pressure is slightly smaller and at a higher C_p value than T = 1%. The difference is why the thicker airfoils achieve a have slightly higher $C_{l,max}$.
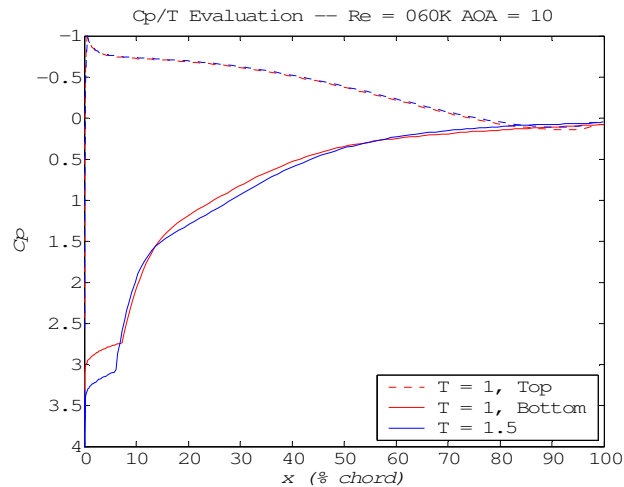
Figure 4.28: Cp/T Evaluation (Re=60K, α=10°)

4.3   Results: $C_l/C_{d,max}$ and $\alpha_{Cl/Cd,max}$

$C_l/C_{d,max}$ is a measure of the efficiency of airfoil. A high $C_l/C_{d,max}$ value means an airfoil that can generate high lift with a minimal drag penalty resulting in minimal power consumption

during flight or higher flight speeds at lower power consumption. The value of $\alpha_{Cl/Cd,max}$ dictates whether the airfoil is likely to operate at or near $C_l/C_{d,max}$. The following sections will present the affect C, xC, R, xR, and t have on $C_l/C_{d,max}$ and $\alpha_{Cl/Cd,max}$.

4.3.1 Max Camber and Position of Max Camber

The affect changes in C and xC have on $C_l/C_{d,max}$ and $\alpha_{Cl/Cd,max}$ are more complex than on $C_{l,max}$ and α_{stall}. The trends in $C_l/C_{d,max}$ and $\alpha_{Cl/Cd,max}$ associated with changes in C and xC are best described by what quadrant of the C/xC plane the airfoil is in. Figure 4.29 shows the quadrants for reference.
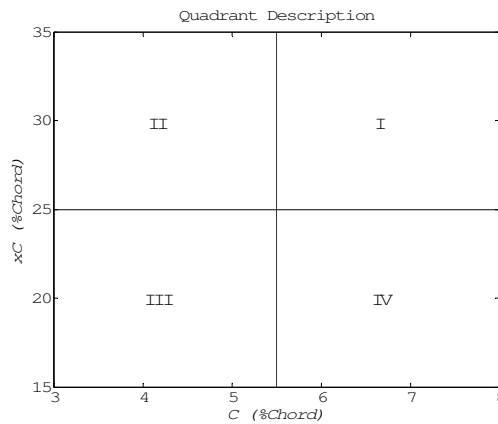
Figure 4.29: Quadrant Description

Results for various Re numbers, R, and xR values show that quadrant III attains the highest $C_l/C_{d,max}$ values for a majority of airfoils. The lowest values appear in quadrant IV. Values across quadrants I and II show relatively similar performance but at magnitudes less than those attained in quadrant III. In quadrants I and IV decreasing xC degrades performance where as in quadrants II and III decreasing xC improves performance. These trends are evident for the data presented in Figure 4.30, Figure 4.31, and Figure 4.32.

Figure 4.30: C/xC Evaluation: $C_l/C_{d,max}$ (R=2, xR=75, T=0.10, Re=100K)

C/xC Evaluation (R = 1, xR = 80, T = 0.10) Re = 100K

Figure 4.31: C/xC Evaluation: $C_l/C_{d,max}$ (R=1, xR=80, T=0.10, Re=100K)

C/xC Evaluation (R = 3, xR = 80, T = 0.10) Re = 60K
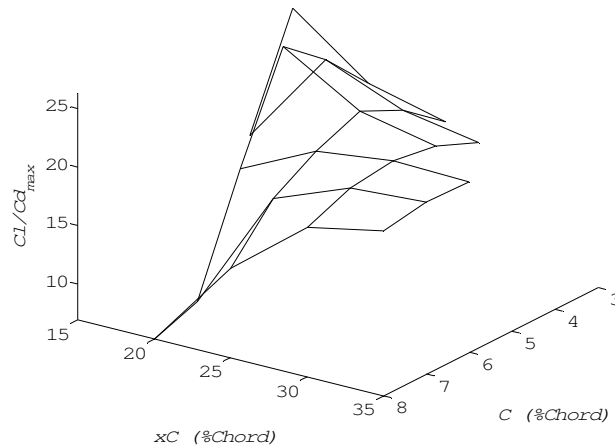
Figure 4.32: C/xC Evaluation: $C_l/C_{d,max}$ (R=3, xR=80, T=0.10, Re=60K)

Unlike $C_{l,max}$ these trends are also dependent on xR, with increased xR resulting in a shift in maximum C_l/C_d performance to quadrant IV. The shift in trends shows a strong interdependence between C, xC, and xR which was not discovered for $C_{l,max}$ or α_{stall}. Figure 4.33 shows the $C_l/C_{d,max}$ performance for an airfoil with xR = 85% chord, to be compared with Figure 4.30.

C/xC Evaluation (R = 2, xR = 85, T = 0.10) Re = 100K
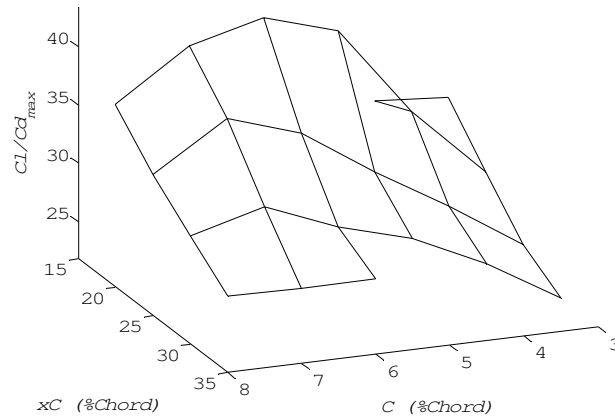
Figure 4.33: C/xC Evaluation: $C_l/C_{d,max}$ (R=2, xR=85, T=0.10, Re=100K)

The shift in peak $C_l/C_{d,max}$ performance to higher C values for constant xC values is consistent with the improved performance in quadrant IV. Moving xR aft prevents the drop in performance from occurring in quadrant IV. To determine the cause of this behavior an evaluation of the laminar separation bubble location and the drag polar for two characteristic airfoils was performed. Laminar separation bubble location plots are important in determining the potential magnitude of bubble drag which is considered a major contributor to the total drag of a low Re number airfoil (Lyon, et al. 1997; Gopalarathnam, et al. 2001). The BEZ072027510 and BEZ072028510 airfoils at Re = 100,000 achieve a $C_l/C_{d,max}$ of 17.5 and 41.7 respectively. The BEZ072027510 airfoil achieves $C_l/C_{d,max}$ at an angle of attack of 12.2° and the BEZ072028510 airfoil at 9.0°. Figure 4.34(a, b) and Figure 4.35(a, b) show the laminar separation bubble location and drag for the BEZ072027510 and BEZ072028510 airfoils respectively. The lift polar is not presented because both airfoils exhibit similar C_l vs. α behavior.

(a)   (b)
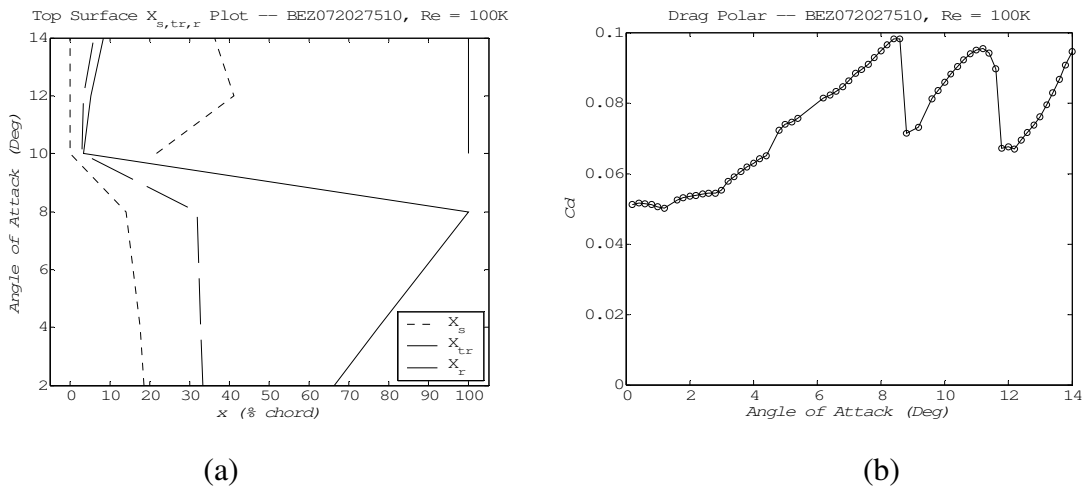
Figure 4.34: Transition Plot/Drag Polar – BEZ072027510
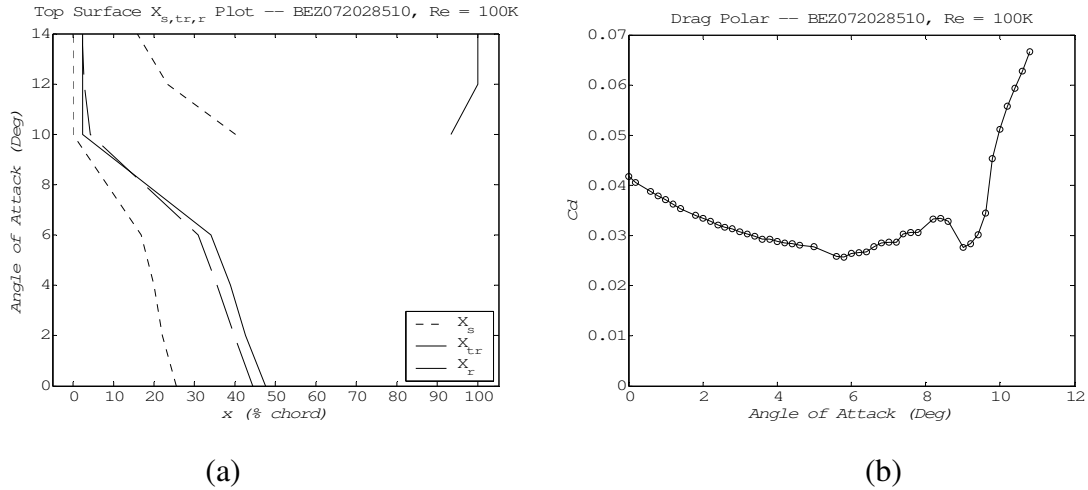
Figure 4.35: Transition Plot/Drag Polar – BEZ072028510

In Figure 4.34(b) the drag plot has two local minima at approximately 9° and 12° angle of attack which correspond to regions of reduced bubble drag. At 12° angle of attack, the short leading edge laminar separation bubble causes the aft separated region to shrink reducing the total bubble drag. The drag polar for the BEZ072028510 airfoil shows a more traditional shape with a region of relatively constant low drag and an increase in drag associated with post stall angles of attack. The local minimum in the drag polar at 9° corresponds to the $C_l/C_{d,max}$. The decrease in drag is caused by the formation of a small leading edge laminar separation bubble which allows the aft potion of the airfoil to operate separation free. This behavior is due to the geometric connection between the curvature of the section just aft of the max C location and xR. As xR is shifted aft the curvature decreases slightly allowing the boundary layer to reattach and preventing the formation of a laminar separation bubble on the aft portion of the airfoil.

The behavior of $\alpha_{Cl/Cd,max}$ is dependent on what quadrant of the C/xC plane the airfoil is in. Quadrant II consistently exhibits relatively low $\alpha_{Cl/Cd,max}$ with increasing performance moving towards quadrants I and IV. Quadrant III regularly attains the highest $\alpha_{Cl/Cd,max}$ values. Figure 4.36, Figure 4.37, and Figure 4.38 represent three examples of airfoil groups that demonstrate these trends.

83

C/xC Evaluation (R = 2, xR = 75, T = 0.10) Re = 100K
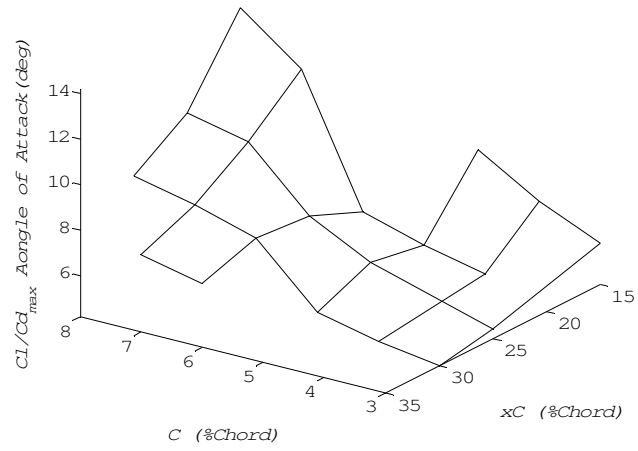
Figure 4.36: C/xC Evaluation: $\alpha_{Cl/Cd,max}$ (R=2, xR=75, T=0.10, Re=100K)

C/xC Evaluation (R = 1, xR = 80, T = 0.10) Re = 60K
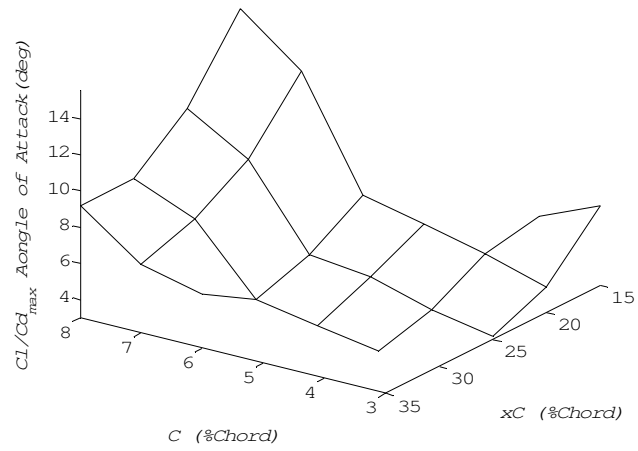
Figure 4.37: C/xC Evaluation: $\alpha_{Cl/Cd,max}$ (R=1, xR=80, T=0.10, Re=60K)
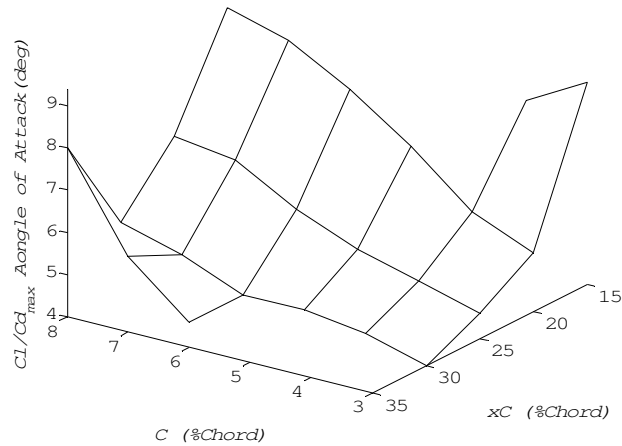
Figure 4.38: C/xC Evaluation: $\alpha_{Cl/Cd,max}$ (R=2, xR=85, T=0.10, Re=100K)

Decreasing xC tends to have a stronger effect on $\alpha_{Cl/Cd,max}$ than increasing C. This is attributed to the drag penalty associated with separated flow at higher angles of attack present for higher camber airfoils. The effect of changes in xR on $\alpha_{Cl/Cd,max}$ are not evident in the IV quadrant. The slight increase at high C and xC values was not found consistently and not considered a trend associated with changes in any airfoil shape parameter.

4.3.2 Max Reflex and Position of Max Reflex

The relationship of R and xR to $C_l/C_{d,max}$ is distinct, with changes in R and xR resulting in predictable variations in $C_l/C_{d,max}$. Changes in $\alpha_{Cl/Cd,max}$ are not as consistent and show no clear trends for the range of airfoils parameters tested. The interdependence of C, xC, and xR was described in the previous section and will not be addressed in this section. The general trends associated with changes of R and xR will be the focus of this section.

Increasing xR and decreasing R resulted in increases in $C_l/C_{d,max}$. This trend is evident in Figure 4.39 and Figure 4.40. There is no clear dominance of xR or R over the other, with changes in either variable resulting in changes in $C_l/C_{d,max}$ of similar magnitude.

85

R/xR Evaluation (C = 4, xC = 20, T = 0.10) Re = 60K
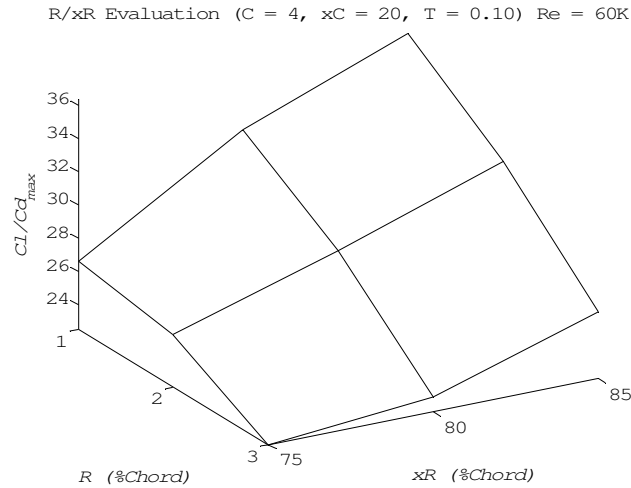
Figure 4.39: R/xR Evaluation: $C_l/C_{d,max}$ (C=4, xC=20, T=0.10, Re=60K)

R/xR Evaluation (C = 6, xC = 30, T = 0.10) Re = 150K
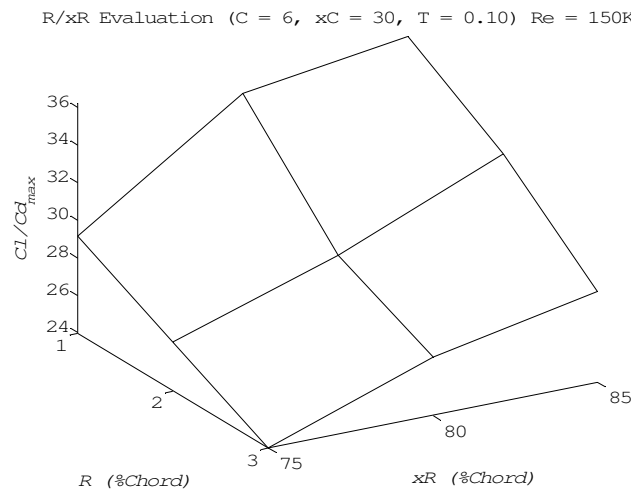
Figure 4.40: R/xR Evaluation: $C_l/C_{d,max}$ (C=6, xC=30, T=0.10, Re=150K)

To determine the cause for the balance between the effects of changes in R and xR, 3 of the airfoils presented in Figure 4.40 were evaluated. BEZ063017510 was chosen as the baseline; BEZ063018510 and BEZ063037510 were chosen because they achieve a gain in $C_l/C_{d,max}$ of 9.1 and 8.7 respectively and represent independent changes to xR and R. A comparison plot of C_l/C_d for the three airfoils is presented in Figure 4.41.
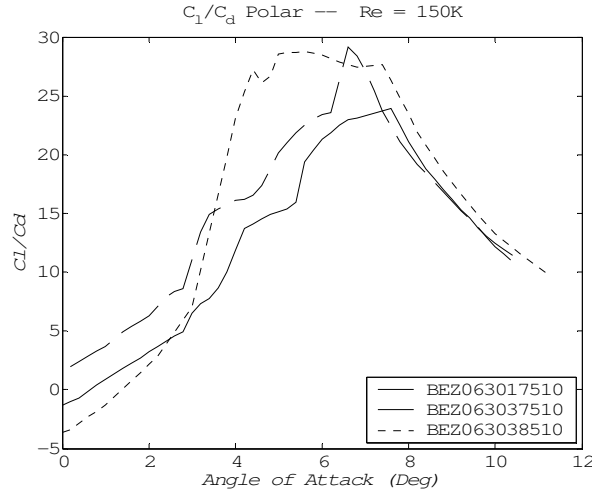
Figure 4.41: R/xR Evaluation: C_l/C_d Polar (C=6, xC=30, T=0.10, Re=150K)

The behavior of the three C_l/C_d plots shows that the similar change in magnitude of $C_l/C_{d,max}$ is not due to a similar change in C_l/C_d behavior. The baseline airfoils (solid line) and the airfoil with an aft shift in R (dashed line) show similar shape in C_l/C_d with an increase in magnitude with an additional jump in performance at 7° due primarily to changes in C_d; this is consistent with the previous finding that R has a minimal effect on $C_{l,max}$. The dotted curve, corresponding to the airfoil with increased xR, shows a noticeable departure from the baseline airfoil representing a change in boundary layer behavior. The fact that the magnitude of the change in $C_l/C_{d,max}$ from the baseline airfoil for the two test airfoils is not attributed to changes in xR and R causing similar changes in boundary layer behavior.

The shift in C_l/C_d for the BEZ063038510 airfoil present in Figure 4.41 is significant because it represents a substantial improvement in airfoil performance characteristics. With an increase in xR, the range of angle of attack that the airfoil attains near $C_l/C_{d,max}$ values is expanded from a point to a broad band. This trend was not found consistently for other values of xC and C with xR = 85% and R = 1% chord.

There was no consistent trends associated with $\alpha_{Cl/Cd,max}$ for changes in xR or R. The variation in $\alpha_{Cl/Cd,max}$ was beyond the limit expected for variation due to the discrete nature of the data. It is possible that the 3 xR and 3 R values do not provide enough resolution to

develop the general trends present in the data. The invariance of α_{stall} to changes in xR and R was attributed to the tendency of the boundary layer over the aft portion of the airfoil to be fully separated, but with the case of $\alpha_{Cl/Cd,max}$ the boundary layer separation and reattachment locations are highly sensitive to xR and R. In addition, the interdependency of $C_l/C_{d,max}$ on xC, C, and xR results in drastic changes in boundary layer behavior with subtle changes in xR and R.

4.3.3 Thickness

Comparing the $C_l/C_{d,max}$ and $\alpha_{Cl/Cd,max}$ performance of each airfoil at thickness values of 10% and 15% chord showed no change in performance trends. For $Cl/C_{d,max}$ the average difference between airfoils with 10% and 15% thickness was -0.26. The average $C_l/C_{d,max}$ value for only 10% thickness airfoils was 24.9 and 24.1 for 15% thickness. Similar results were found for $\alpha_{Cl/Cd,max}$ which had an average difference of 0.26° between similar airfoils at 10% and 15% thickness. The difference is just slightly larger than the minimal angle of attack step size used for the analysis of 0.2°. Figure 4.42 and Figure 4.43 shows an example of the difference in laminar separation bubble location for both 10% and 15% thickness airfoils. The discrepancy at lower angles of attack is attributed to a lack of converged boundary layer data at an angle of attack at 6°. The similarity between the plots was found consistently for all airfoils parameters.
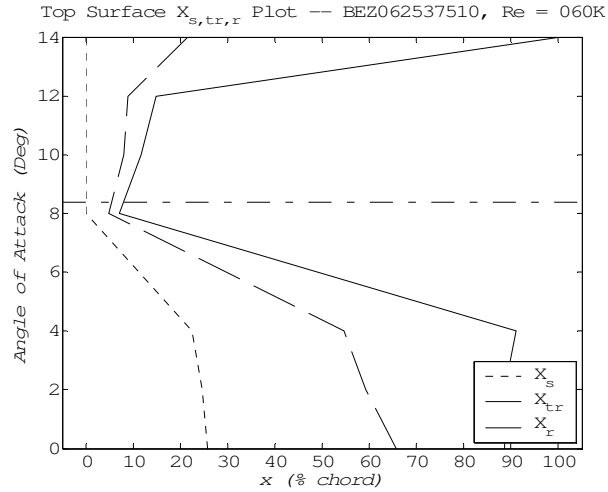
Figure 4.42: Separation/Transition/Reattachment: BEZ062537510, Re=60K
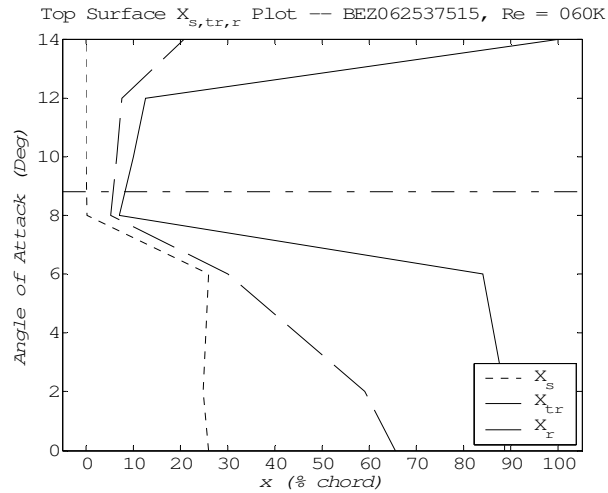
Figure 4.43: Separation/Transition/Reattachment: BEZ062537515, Re=60K

4.4 Design Methodology

Two basic airfoil design methods are presented that focus on two fundamentally different requirements; high $C_{l,max}$ and high $C_l/C_{d,max}$. Airfoils intended for slow flight speed/high lift applications are defined by their $C_{l,max}$ performance. Fast flight speed/low drag airfoil requirements are achieved by focusing on $C_l/C_{d,max}$ performance. The following sections

89

address each of these types of airfoil design methods and suggest the importance of each airfoil shape parameter. Example airfoils are presented in each section. The final section will discuss the limitations of a 2D design approach. The intent of this section is to present a possible scenario in which the results of the analysis can be applied to airfoil design. Further work is required to establish a sophisticated design process.

Common to both methods is an emphasis placed on low range Re number performance. This requirement is intended to address the desire to decrease overall aircraft size which results in smaller airfoil chord lengths and lower Re numbers.

4.4.1   Design for $C_{l,max}$

The focus of design for $C_{l,max}$ is to attain a high $C_{l,max}$ with preference placed on airfoils with trailing edge stall behavior. Trailing edge stall is important in design for $C_{l,max}$ because the airfoil will be operating near α_{stall} and trailing edge stall behavior exhibits minimal drop in C_l at post stall angles of attack, allowing for easy recovery from stalled flight conditions. C and xC have a strong effect on $C_{l,max}$, so they are the driving parameters and will be chosen first. This is possible because the performance trends associated with C and xC show little dependence on R and xR. R and xR are considered secondary parameters and chosen to improve $C_{l,max}$.

Using the information presented in Section 4.2.1 higher C values and xC values no less than 20% are favorable for high $C_{l,max}$ performance. From Section 4.2.2, higher xR values result in higher $C_{l,max}$ values. The amount of max reflex, R, is considered a free variable because it does not effect $C_{l,max}$ performance. An airfoil with xC = 25%, C = 8%, xR = 85%, R = 1%, and t = 10% was chosen as the preliminary airfoil. The results presented are for Re = 60,000 in accordance with the emphasis placed on low Re number performance. Figure 4.44 shows that for a range of 1.8°, C_l is within 5% of $C_{l,max}$. As shown in Figure 4.45, this airfoil also has the advantage of exhibiting a local maximum in C_l/C_d near α_{stall}. In addition, less than 1% of that airfoils tested achieve a $C_{l,max}$ at Re = 60,000 greater than the airfoil chosen. The airfoil is presented in Figure 4.46. The limitations of XFOIL's prediction capabilities would

require wind tunnel testing to verify the exact magnitude of the airfoil's performance characteristics.
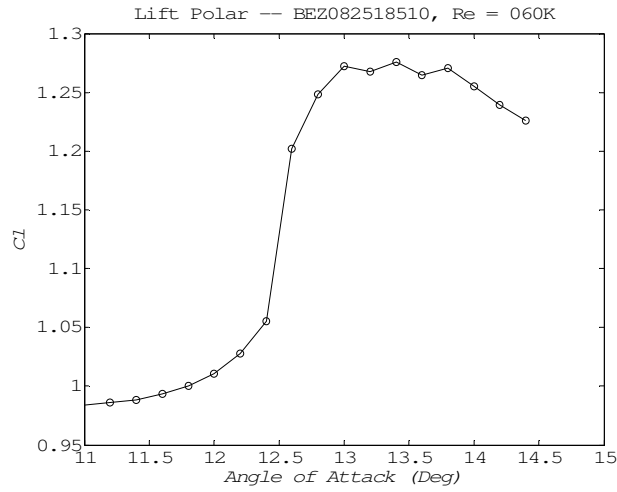
Figure 4.44: C_l Polar: BEZ082518510, Re=60K
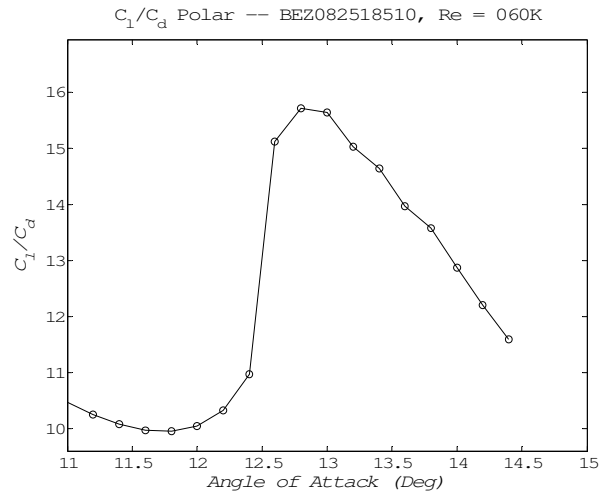
Figure 4.45: C_l/C_d Polar: BEZ082518510, Re=60K
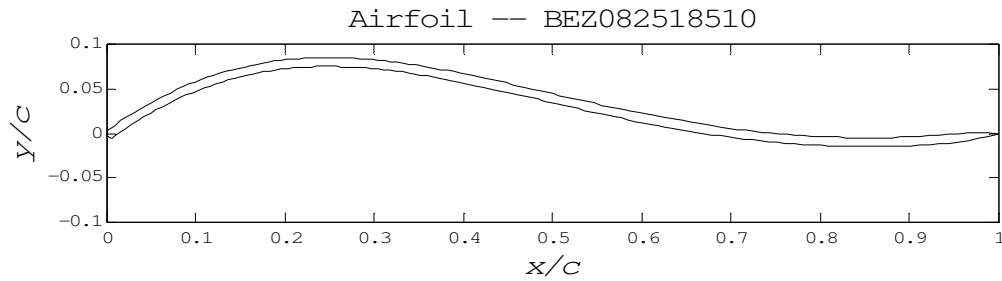
Figure 4.46: BEZ082518510

4.4.2 Design for $C_l/C_{d,max}$

The goal of design for $C_l/C_{d,max}$ is to achieve a high $C_l/C_{d,max}$ value. Due to the strong coupling between C, xC, and xR, and their direct effect on $C_l/C_{d,max}$ all three are deemed primary variables. R is considered a secondary variables and chosen to improve $C_l/C_{d,max}$ performance.

Using the information presented in Section 4.3.1 and Section 4.3.2 the airfoil designer is able to create an airfoil that achieves a high $C_l/C_{d,max}$. Increasing xR shifts $C_l/C_{d,max}$ to higher C values and increases the magnitude of $C_l/C_{d,max}$. For this reason xR = 85% was chosen. The corresponding C and xC values therefore occurred near the boundary of quadrants III and IV. C = 6% and xC = 25% were chosen because they represent the maximum $C_l/C_{d,max}$ attained in the C vs. xC plane for xR = 85%. R=3% was chosen because of the direct correlation between increasing R and increasing $C_l/C_{d,max}$. The resulting airfoil BEZ062538510, presented in Figure 4.47, achieves a $C_l/C_{d,max}$ of 28.2 with only 2% of all the airfoils tested achieving a higher $C_l/C_{d,max}$. Figure 4.48 shows the C_l/C_d plot for the chosen airfoil. The limitations of XFOIL's prediction capabilities would require wind tunnel testing to verify the exact magnitude of the airfoil's performance characteristics.
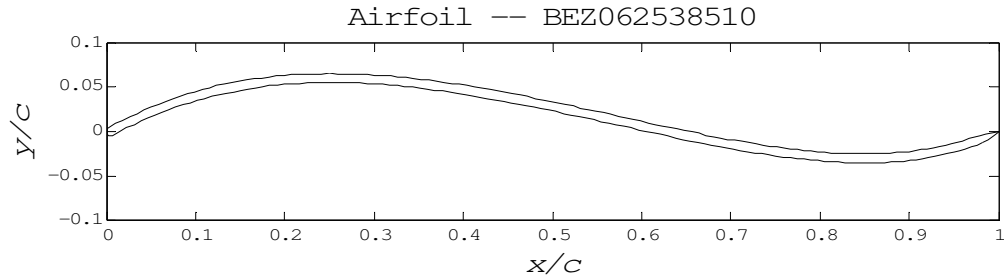
Figure 4.47: BEZ062538510
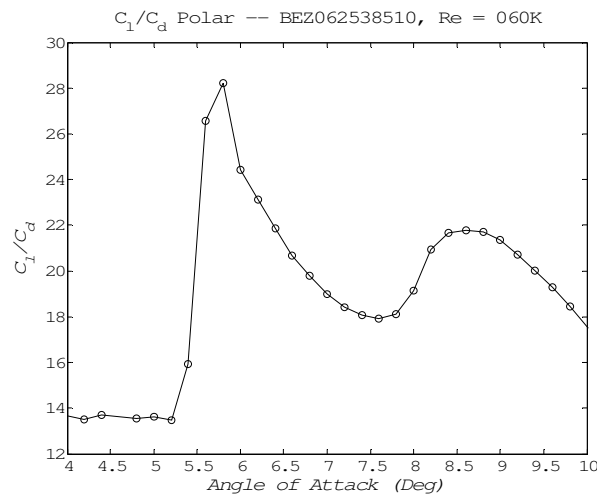
Figure 4.48: C_l/C_d Polar: BEZ062538510, Re=60K

4.4.3 Limitations

The major limitation of the design methods is that they only suggest the airfoils that achieve favorable performance characteristics, not 3D wing shapes. The behavior of the 2D airfoil is an indication of how a similar shaped wing might perform, but in most cases the airfoil shape along the wing's span is modified to address the 3D flow effects. To account for this, the design methods can be applied to different sections of the wing span to address the varying flow phenomena. For example, strong 3D vortex structures are present at the wing tips of a low aspect ratio wing, causing the local angle of attack to be reduced and the upper surface less susceptible to boundary layer separation (Lian, et al 2003; Torres, Mueller 2004; Viieru, Lain, Shyy, Ifju 2003). These changes in local flow phenomena need to be taken into

93

account to determine the best airfoil shape for that section of the wing. Additional factors such as prop wash, and control surface location play an important roll in the 3D flow structure present for a wing. For the successful design of a wing for a MAV all of these effects must be taken into account.

Additionally, the design methods only suggest the airfoils that have improved relative performance over the other airfoils tested; this does not guarantee that airfoil parameters between, greater than, or less than the values tested won't perform better. The resolution of the present study would need to be increased to eliminate this limitation.

4.5 Conclusions

The presence of the discontinuity in the lift curve was found to be consistent with the boundary layer behavior of the upper and lower surfaces. XFOIL's prediction that the lower surface boundary layer remains in the separated or attached state of the previous angle of attack is consistent with experimental results for stall hysteresis behavior. The exact shape of the near jump region of the lift curve was found to be dependent of the upper and lower boundary layers.

A direct correlation was found between C and both $C_{l,max}$ and α_{stall}. Changes in C caused a shift in the boundary layer transition location to higher angle of attack allowing the airfoil the achieve higher $C_{l,max}$. Decreasing xC resulted in increased $C_{l,max}$ and α_{stall} values. Decreasing xC increased the C_p spike near the leading edge and increased the angle of attack at which a short leading edge laminar separation bubble forms, both of which improve $C_{l,max}$ and increase α_{stall}.

Changes in R did not result in any changes in $C_{l,max}$ or α_{stall}. This trend was consistent with the large laminar separation bubble region present on the aft portion of the airfoils at α_{stall}. Shifts in xR towards the trailing edge caused an increase in $C_{l,max}$ due to a corresponding shift in the pressure recovery region aft. With pressure recovery occurring nearer the trailing edge

more of the airfoil experiences higher C_p values which resulted in higher $C_{l,max}$. There was no correlation found between the airfoil parameter xR and α_{stall}.

Thickness variation caused only a slight increase in the magnitude of $C_{l,max}$ due to an increase in the leading edge pressure spike and presence of smaller leading edge laminar separation bubbles. Thickness was not found to have an effect on $C_l/C_{d,max}$ or $\alpha_{Cl/Cd,max}$.

The airfoil shape parameters C, xC, and xR were found to be interrelated when determining relative $C_l/C_{d,max}$ performance. For $C_l/C_{d,max}$ over the range of C and xC values a saddle point in present near the mid field point with high C and xC and low C and high xC value combinations resulting in moderate relative performance. Low C and xC values showed the highest $C_l/C_{d,max}$ performance with high C and low xC values exhibiting the lowest $C_l/C_{d,max}$ performance. This trend shifted to higher C values with increasing xR. At xR = 85%, high C low xC transitioned from the lowest performing to the highest performing $C_l/C_{d,max}$.

A direct correlations was found between C and $\alpha_{Cl/Cd,max}$. For decreasing xC, $\alpha_{Cl/Cd,max}$ increased with the increase becoming larger for higher xR values. This was expected considering the interdependence of the 3 parameters found for $C_l/C_{d,max}$. Increasing xR and decreasing R resulted in changes of similar magnitude in $C_l/C_{d,max}$, though due to dissimilar changes in the boundary layer performance. There were no consistent changes in $\alpha_{Cl/Cd,max}$ caused by modification of xR or R.

Significant airfoil performance modifications can be achieved with control of the 5 specific airfoil shape parameters. Changes in C and xC account for 40% variation in $C_{l,max}$ and R and xR account for 15% variation in Cl,max. Modifications to C and xC account for 40% variation in α_{stall}. $C_l/C_{d,max}$ vary up to 30% due to changes of C and xC and 20% for changes in R and xR. 50% variation in $\alpha_{Cl/Cd,max}$ is achieved with adjustments to C and xC.

5 Airfoil Testing

At the onset of this research it was determined that the low speed closed circuit wind tunnel and accompanying low force/moment balance were insufficient to accurately measure lift, drag, and moment data. Through further investigation it was concluded that the wind tunnel would be able to provide boundary layer observation capability with reasonable anticipated accuracy by utilizing a surface oil flow visualization technique. Boundary layer details such as separation and reattachment location are critical in determining airfoil performance and a validation of XFOIL's boundary layer predictions provides insight into XFOIL's ability to predict other aspect of airfoil performance. The objective of the testing is to compare the boundary layer observations taken in the wind tunnel to the predictions of laminar separation bubble location by XFOIL.   The results can also be used to determine the validity of future wind tunnel experiments.

The following section will address the airfoils chosen for experimental validation. The second section describes the experimental set-up used, measurements devices, and sources of error. The third section addresses the experimental procedure. The fourth section presents the results of the validation study. The final section covers the experimental results and discussion.

5.1 *Experimental Airfoils*

A set of five airfoils were chosen from the 432 airfoils analyzed in an attempt to verify airfoils with varying $C_l/C_{d,max}$ and $C_{l,max}$ performance. The selected airfoils are presented in Table 5.1 along with their $C_l/C_{d,max}$ and $C_{l,max}$ performance as predicted by XFOIL.   In addition, an E387 airfoil was chosen for experimental validation because of the prevalence of published boundary layer data available from multiple sources.

96

Airfoil Name	Re Number	$C_{l,max}$	$C_l/C_{d,max}$
BEZ032037516	60,000	0.81	19.26
	100,000	0.78	21.60
	150,000	0.78	23.36
BEZ053018513	60,000	1.06	28.18
	100,000	0.99	31.50
	150,000	1.06	33.92
BEZ062518513	60,000	1.21	30.54
	100,000	1.25	38.24
	150,000	1.14	44.18
BEZ072018013	60,000	1.12	11.38
	100,000	1.19	18.53
	150,000	1.37	38.53
BEZ083018513	60,000	1.33	21.49
	100,000	1.39	32.53
	150,000	1.34	39.29

Table 5.1

The range of airfoils was chosen to test a wide variety of boundary layer characteristics. The BEZ032037516 airfoil was chosen primarily for its unique shape. With 3% camber and 3% reflex, the airfoil as almost a symmetric *S* shape, yet it is able to achieve reasonable $C_l/C_{d,max}$ values. Relatively consistent $C_{l,max}$ and $C_l/C_{d,max}$ values for the range of Re numbers was the reason BEZ053018513 and BEZ062518513 were chosen; as well as the high over all values. The BEZ072018013 airfoil was chosen for its high $C_l/C_{d,max}$ variance with Re number. The final airfoil, BEZ083018513 was chosen because of its surprisingly high $C_l/C_{d,max}$ values.

5.1.1 Airfoil Construction

The airfoils used in the experiment were required to be rigid while having a thickness less than 2% chord. An airfoil construction method utilized a simple positive/negative compression mold and carbon fiber composite material was chosen. A similar method had been used by the author previously to construct thin rigid airfoils and has been proven effective. All necessary tools and materials were readily available, which greatly simplified construction.

The five test airfoils and the E387 airfoil were chosen to have a 0.13m chord and 0.26m span with a rectangular planform, resulting in an aspect ratio (AR) of 2.0. This size ensured that the lift and drag forces would not exceed the limits of the current balance if future measurements were required. The nominal velocity required to achieve a Re number of 60,000 for the wing was less than the low limit of the wind tunnel, yet reducing the size of the wing to accommodate higher wind tunnel velocities would greatly obstruct oil flow visualization. It was decided that only Re numbers of 100,000 and 150,000 would be tested. The span was chosen so that the tip vortices generated would not impinge on the wind tunnel walls. The span was also sufficient to limit tip vortex effects from reaching the mid-span region at moderate angles of attack, resulting in mostly 2D flow at mid-span.

Mold construction began by creating an airfoil template from a scale printout of each of the 5 Bezier airfoils. Thin cardboard was used as the template material. The cardboard templates were cut at the lower surface of the airfoil to allow for the thickness of carbon fiber material. Once cut, the edges of the cardboard were coated with a thin layer of epoxy to harden the edge. The mold was made from rigid foam insulation, available at most local home improvement stores. Rigid foam insulation was chosen for its dimensional stability and availability. The foam was cut into blocks using a *hot wire* technique, where current is passed through a wire that heats due to internal resistance. The heated wire can then easily cut through the foam, similar to a precise band saw. The airfoil templates were then applied to opposite sides of the foam blocks. The hot wire was used to cut the foam block along the template's edge creating the positive and negative sides of the mold. Any slight surface irregularities were sanded with fine grit sand paper. The mold surfaces were then covered

with a layer of 2 oz. fiberglass and 2 layers of epoxy. Each layer was sanded with fine grit sand paper resulting in a glass like surface finish.

A layer of 6 oz. carbon fiber was used as the primary structural layer of the airfoil. The carbon fiber was placed between two finished mold halves and covered with epoxy and a mold release plastic. At least 40 lbs of ballast was placed on top of each mold in order to ensure a complete mate over the entire upper to lower mold interface. The epoxy was allowed to harden for 18 hours. An additional layer of 2 oz. fiber glass was applied to the upper surface of the airfoil following the same procedure as with the first layer. After the second layer was sanded smooth, a third layer comprised of a piece of white grid paper and 1 oz. finishing fiberglass was applied to the upper surface and placed between the mold halves. Two additional thin layers of epoxy were applied to the upper surface of the airfoil and allowed to cure outside of the mold. After each layer of epoxy, the upper surface was wet sanded with a sequence of 400, 600, and 800 grit sand paper. In the final step the leading edge was sanded round and the trailing edge was sanded to a sharp point to mimic the shape of the airfoils used for the analysis.

The E387 airfoil, chosen for boundary layer validation, had a thickness distribution and could not be made in the same way as the five Bezier airfoils. The construction method was similar, except when cutting the airfoil out of the foam block; the upper and lower surfaces of the airfoil were cut resulting in 3 mold pieces. The upper and lower foam portions were treated just as the previous molds had been. The center foam piece, which had the airfoil shape, was sanded to remove any irregularities. The trailing edge was removed at approximately 85% chord because the airfoil's thickness was to thin for the foam to maintain the desired shape. The aft 15% was replaced with a tapered piece of 1/8" balsa wood, attached to the foam with epoxy. The resulting airfoil was covered with a layer of 1 oz. fiber glass, followed by a layer of graph paper and 1 oz fiber glass and 2 layers of epoxy. The first two layers were cured under pressure between the upper and lower mold halves. The final two epoxy layers were allowed to harden separate of the molds and were sanded in the same way as the Bezier test airfoils.

The final step was to apply a small aluminum tab to the lower surface trailing edge of the airfoils as an attachment point. The aluminum tab was created by bending a strip of 1"x4"x1/16" aluminum sheet metal into a *T* shape. Each leg of the *T* was 1" long with the lower porting of the *T* being doubled up. The upper portions of the *T* were attached to the trailing edge so the lower portion was perpendicular to the airfoil surface and parallel with the chord wise direction. The aluminum tab is used to attach the airfoil to the sting in the wind tunnel.

5.1.2   Airfoil Measurements

Each airfoil was measured in various locations in order to determine its exact dimensions. Chord measurements were taken at the mid-span location as well as 0.06m to the right and left of mid-span. The average of these three values was used as the airfoil's chord length. Airfoil thickness measurements were taken at three different locations as well. Measurements at points near the leading edge, trailing edge, and mid-chord were averaged to determine the airfoil's thickness.

The shape of the Bezier airfoils was tested using a master template created in the same way as the templates used in making the molds. All five airfoils match their respective master templates within 0.25mm at mid-span and 0.06m to the right and left of mid-span. The E387 airfoil upper and lower surfaces were checked in the same way. An additional template was made to check leading edge radius of the E387 airfoil. It was discovered that the actual leading edge radius was slightly larger than the intended leading edge radius. The effects of this discrepancy are addressed in Section 5.2.3.

5.2   *Experimental Set-up*

The intent of the experimental set up was to utilize as much of the current wind tunnel configuration as possible. Since no force or moment data was required only a limited

number of experimental variables needed to be recorded; minimizing the time required to calibrate and validate measurement devices. The current low force/moment balance was used for testing, though only as a device to change airfoil angle of attack, not as an instrument for gathering data. A detailed description of the balance and the wind tunnel is given by Shreve (2005) and will not be presented here; only the aspects of the experimental set-up that were critical to the experiment will be covered.

5.2.1 Wind Tunnel

The test airfoil was attached to the balance in the wind tunnel using a solid aluminum rod. The rod clamped to the aluminum T structure on the trailing edge of the airfoil and was attached to the balance using a sleeve and 2 set screws. The rod was attached to the airfoil at zero incidence so an airfoil angle of attack of 0° corresponded to a sting angle of 0°. The length of the sting was such that the airfoil's ¼ chord point was directly over the balance rotation point as suggested by Shreve (2005). This cause the airfoil to rotate about its ¼ chord point as angle of attack was changed.

Wall structures, called splitter plates, were placed on either side of the airfoil in the wind tunnel. Both splitter plates were placed parallel to the flow leaving a nominal 0.5 cm gap between the test airfoil and the splitter plates. The leading edge of the airfoil was 1.5 chord lengths from the start of the splitter plates. Splitter plates are used to isolate the airfoil from the 3D flow effect created by tip vortices. Preliminary boundary layer tests performed without splitter plates resulted in a spanwise variation in separation and reattachment points. This behavior was eliminated with the use of splitter plates. There was slight interference near the wing tips due to boundary layer growth on the splitter plates; however the effect was localized to 1.0 cm from each splitter plate.

The balance alone proved insufficient to prevent small vibrations and deflections in the test airfoil. During an initial test the airfoil deflected as much as 1.0 cm up and back with a variation in position of +/- 0.5 cm in all directions. As angle of attack and velocity increased

the deflections and vibrations grew. In order to prevent deflection, nylon thread was attached to the lower surface of the Bezier test airfoil at the ¼ chord point and a small hole was drilled in each splitter plate at the corresponding location. The nylon tread was pulled taunt through each hole and held in place to the outside of the splitter plate with a piece of tape. Using this method, all visible deflections and vibrations were eliminated with little to no effect on the airfoil or splitter plate boundary layer. In the case of the E387 airfoil, a small rod that passed through the splitter plate and into a hole in the end airfoil was used. The effect was the same as the nylon thread method.

5.2.2 Measurement Devices and Error

There are five basic parameters that must be monitored during testing, velocity, temperature, pressure, angle of attack, and surface oil feature location. The following sections cover the instruments, methods, and error associated with each of the five measurements.

5.2.2.1 Velocity and Pressure

Wind tunnel velocity is the most critical measured parameter. A Dwyer® series 641RM heated mass flow sensor was used during testing to measure velocity. The device was factory calibrated and had been in use for less than 100 hours of cumulative tunnel run time. Flow velocity was indicated on a LED display. The indicated flow velocity required an adjustment based on local atmospheric pressure. The correlation equation relating corrected velocity (V_{cor}), standard pressure (P_0), atmospheric pressure (P_a), and indicated pressure (V_{ind}) is given in Equation 5.1.

$$V_{cor} = \frac{P_0}{P_a} V_{ind}$$

Equation 5.1

Standard pressure P_0 is 29.9 in. Hg and atmospheric pressure was recorded from weather measurements gathered locally at the Rochester International Airport. The velocity sensor was located midway between the splitter plates 1 chord length in front of the leading edge of the wing and 7.5 cm from the upper wind tunnel wall. This location ensured the sensor would not be affected by upper wall or splitter plate boundary layers. The location is slightly affected by changes in angle of attack.

Before the start of each test the local atmospheric pressure was recorded. This value was assumed constant throughout the test. Atmospheric pressure was reported in in. Hg and has a least count of 0.01 in. Hg.

The error associated with the velocity sensor was defined by the instrument limit of error (ILE). The ILE of a device is the finest increment to which a device can be read or the tolerance value associated with the device. The velocity sensor has an ILE of 3% of the full scale value, which was set to 75 m/s. The resulting error in velocity was 2.5 m/s. The velocity was recorded every minute during the test to establish an average velocity and standard deviation. The ILE and twice the standard deviation were compared and the greater value was reported as the error in velocity. The doubled standard deviation value, representing a 95% confidence interval, was consistently an order of magnitude less then the ILE and never used.

5.2.2.2 Temperature

Wind tunnel temperature was measure using a thermocouple placed aft of the test section in the core region of flow. The aft location was chosen to eliminate any effect on the freestream velocity in the vicinity of the test airfoil. A data acquisition card and LabVIEW interface developed by Shreve were used to record the thermocouple output (Shreve 2005). The thermocouple has a least count of 0.1 °C. Temperature was measure every minute during testing and the average value was used. The standard deviation was found and the 95% confidence interval was calculated and compared to the least count. The larger of the two

values was used as the error in temperature measurement. Unlike velocity, the least count and 95% confidence interval were of the same order of magnitude.

5.2.2.3 Angle of Attack

Airfoil angle of attack was measured using a digital inclinometer attached to the support arm of the balance. The balance arm remains parallel to the sting for all angles of attack. Since the airfoil was attached to the sting at zero incidence the angle of the balance arm is the same as the angle of attack of the airfoil. The error in angle of attack is taken as the least count of the sensor which is $0.1°$. To verify the airfoil's angle of attack is the same as the balance's angle of attack and additional inclinometer is used. A portion of the airfoil's mold was placed on top of the airfoil that created a surface parallel to the chord line of the airfoil. The additional inclinometer was used to find the angle of the upper surface, which is compared to the angle of the balance arm. The zeroing feature on the balance's inclinometer was used to eliminate any discrepancies.

5.2.2.4 Surface Oil Feature Location

The grid paper applied during the construction phase was used to measure the location of surface oil features. The grid paper has bold lines every centimeter running spanwise and chordwise along the test airfoil. Three light weight lines are equally spaced between each bold line signifying 0.25 cm increments. The light weight lines define the ILE for measuring the location of surface oil features. The chordwise location of any surface oil features were measured at the mid-span location as well as 0.06m to the right and left of mid-span. The average value of the three locations was used.

There exists a slight difference between airfoil chord location and the grid location because the grid paper is applied to the surface of the airfoil. This discrepancy increases with an increase in distance from the leading edge. In general, airfoils with higher camber and reflex values have larger differences in chord location and corresponding grid location. In the case

of the BEZ083018513, which has the largest discrepancy, the maximum difference is much less than ILE and the effect is negligible.

5.2.3 Experimental Sources of Error

There are a number of additional sources of error that cannot be measured for the current wind tunnel configuration. Substantial additional testing would be required to quantify these errors which is beyond the scope if the current research. However the anticipated effect of any additional sources of error can be used to understand discrepancies in wind tunnel data.

The turbulence level of the core region of flow in the test section is important in understanding airfoil boundary layer behavior. There currently is no information regarding the turbulence level of the RIT wind tunnel. The turbulence level is associated with the variation of velocity in any direction other than the main flow. A reasonable turbulence level for low Re number testing is less than 0.1% of the main flow velocity (Selig, et al. 1995). It has been reported that thin cambered airfoils are insensitive to changes in turbulence level below 1%, minimizing the error associated with the wind tunnel turbulence (Mueller 1999).

Turbulence level is similar to the acoustic disturbances present in a wind tunnel. A number of studies have shown that machinery, traffic, speech, and other ambient noises can cause noticeable changes in lift and drag at low Re numbers by promoting boundary layer transition (Grundy, Keefe, Lowson 2001). The proximity of the RIT wind tunnel to the machine shop as well as the poor internal acoustics of a closed circuit wind tunnel represents significant sources of error.

The RIT wind tunnel utilizes 4 screens up stream of the test section which are thought to reduce the free-stream turbulence intensity. To determine the effect of the screens two validations tests were performed using an E387 airfoil; one test without screens and one with screens. The results are presented in Figure 5.1. The results show that without screens the

laminar separation bubble collapses at an angle of attack 2° less than the test with screens. This is a strong indication that the turbulence level is greater without the screens.

Surface Oil Flow Comparison RIT Wind Tunnel E387
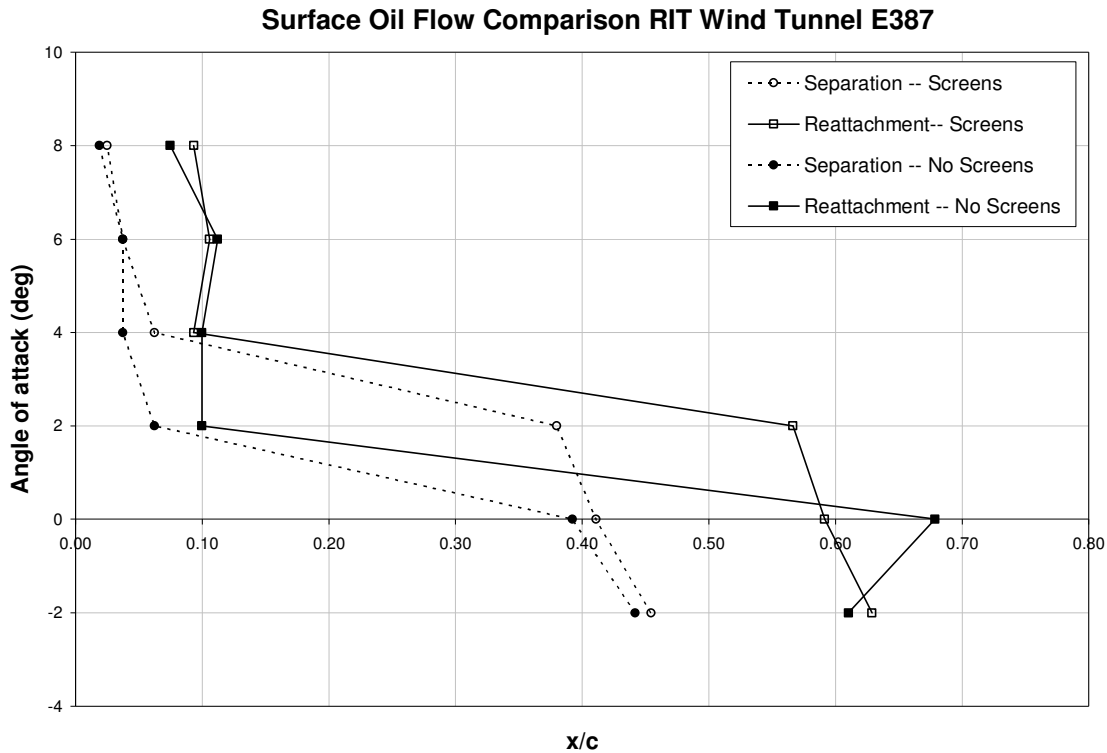
Figure 5.1: Wind Tunnel Results: E387, With and Without Screens

There are additional errors in velocity beyond the instrument error associated with the velocity sensor. The two major sources are blockage and circulations effects. Blockage effects occur whenever the test volume is occupied by either physical objects or regions of low velocity, such as an airfoil's wake. Blockage effective reduces the cross sectional area of the test section causing an increase in local velocity to maintain mass continuity (Barlow, et al. 1999). When testing Bezier airfoils the effect of blockage is minimal at moderate angle of attack because wing volume is negligible. As angle of attack increases and the airfoil's wake region grows and blockage effects amplify. The presence of splitter plates in the test section does affect blockage. Velocity was measured between the splitter plates to better gage the velocity near the airfoil and eliminate the need to account for splitter plate blockage. A velocity measurement location near the airfoil has the disadvantage of being affected by

106

circulation generated by the airfoil. The result of increased circulation is an increase in local velocity (Grundy, et al. 2001). Circulation effects diminish as distance from the airfoil increases. As a result, the velocity sensor was placed a reasonable distance from the airfoil while still being between the splitter plates in order to reduce circulations effects on velocity.

5.3   *Experiment Outline*

In order to ensure consistency in testing of various airfoils, an experimental procedure was developed. In addition, a detailed description of the anticipated surface oil features and their meanings with respect to boundary layer behavior is presented. The surface oil feature descriptions were used to eliminate any inconsistency in interpretation of the experimental results.

5.3.1   Experimental Procedure

Prior to the first test with each airfoil any discrepancy in angle of attack between the airfoil and balance was eliminated using the zeroing procedure described in section 5.2.2.3. Once the airfoil's angle of attack was verified the airfoil was removed from the test section for application of the oil to the airfoil's surface.

Consistency in the fluid/pigment mixture used throughout testing was important. Surface oil flow visualization relies on the use of a constant kinematic viscosity fluid to ensure accurate results. The fluid used was Dow® 200 fluid, which has a known kinematic viscosity of 500 centistokes. Orange pigment in powder form was added to the fluid to increase the visibility of surface oil features. A mass ratio of 5:1, fluid to pigment, was always used to ensure consistent results. The fluid and pigment were stirred for 30 seconds prior to application to ensure a homogeneous mixture. Using leading edge to trailing edge brush strokes, the mixture was applied to the test airfoil with a 3" foam brush. Once completely covered, the airfoil sat in still air for one minute which completely eliminated any surface texture left by

the brush. After the first test of a particular airfoil, the fluid/pigment mixture was reapplied using the same method while the airfoil was still in the test section. The airfoil was allowed to sit for 1 minute with the wind tunnel at zero velocity before the next test started.

When starting the wind tunnel there is a short period of time when the velocity accelerates from 0 m/s to the desired tunnel velocity. This time was limited to no more than one minute. If the amount of time required to reach the desired velocity exceeded one minute the test was restarted with a new layer of fluid/pigment mixture. One minute of slower than desired tunnel velocity did not affect the final result of the test. As velocity increases to the desired velocity, the boundary layer transitions from large regions of fully separated flow to the final boundary layer state. Regions of separated flow are characterized by negligible change in the surface oil layer causing an insignificant change to the surface oil distribution during the first minute. A series of photographs were taken throughout a test to show how the surface oil features were developing over time. The photographs are presented in Appendix D.

Throughout the test, velocity and temperature measurements were recorded once every minute. The total test time was between five to ten minutes, with surface oil feature measurements made during the last minute. Surface oil features were measured while the wind tunnel was still at the desired velocity and the oil features were clearly visible and had not changed position for 2 minutes. Making the measurements at the desired velocity eliminated changes due to tunnel slow down time. Once measurements were made and velocity was reduced to 0 m/s, the process was repeated.

5.3.2 Surface Oil Flow Description

A change in surface oil texture was used to classify the start of the laminar separation bubble region. Slow near-surface velocities result in low surface shear stress and negligible surface texture change over the bubble region. Prior to separation the near-surface velocities are significant, causing changes in surface texture. The point of separation is defined at the boundary of the changed and unchanged surface oil texture. The texture of the pre-separated

region is characterized by a wavy appearance and is easily distinguishable from the region of smooth unchanged surface texture during testing. Photo documentation of the feature could not occur because the wavy texture quickly diminished once wind tunnel velocity was reduced.

Laminar separation bubble reattachment was much simpler to identify. As described by Lyon, et al. (1997) there is a local spike in C_f just prior to boundary layer reattachment. The spike in C_f causes a local accumulation of oil just forward of the reattachment location; referred to as an oil accumulation line. Reattachment was defined as the point just aft of the oil accumulation line. A photograph of the oil accumulation line and the reattachment point are presented in Figure 5.2.
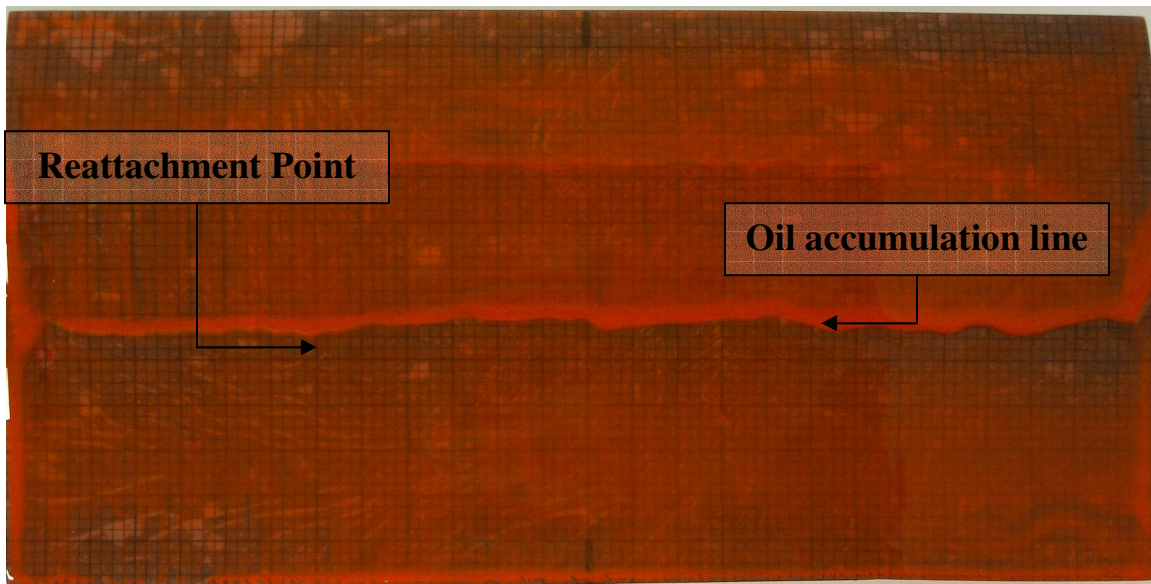
Figure 5.2: BEZ053018513, Re = 100K, α = 0°

Separation and reattachment that spans a short distance of the upper surface starting at the leading edge is distinguished by a clear accumulation of oil at the leading edge. The length of the separated region is too short to for the region of smooth surface texture to develop so the oil accumulation line is the only visible feature. In cases of a leading edge oil accumulation line, separation was recorded at the leading edge and reattachment was

recorded aft of the oil accumulation line. Figure 5.3shows a photograph of the leading edge oil accumulation line and reattachment point.
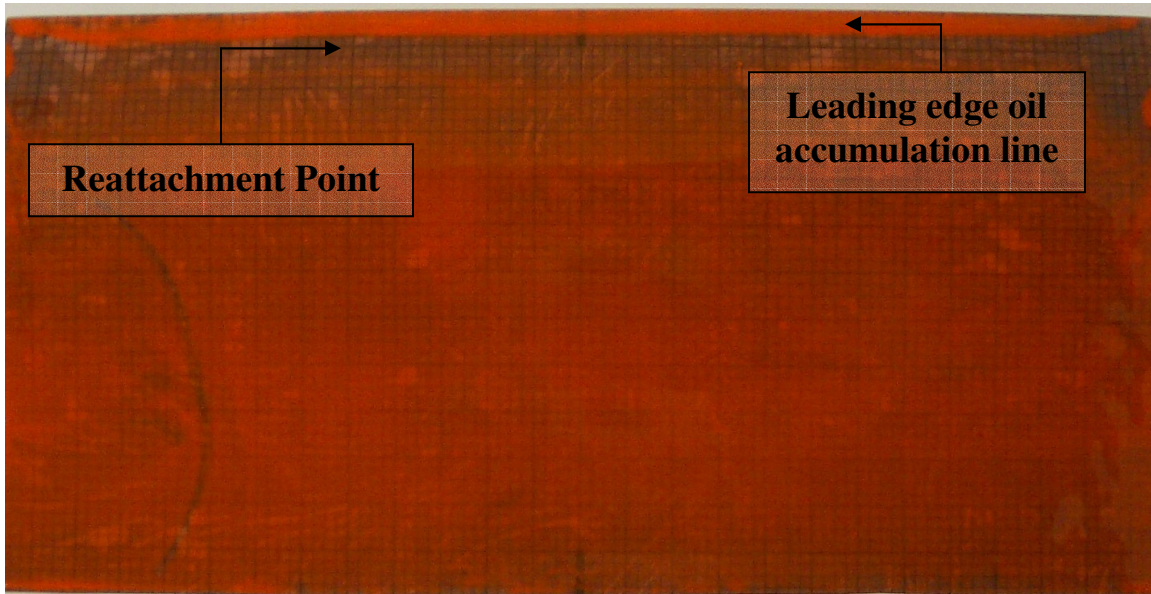
Figure 5.3: BEZ053018513, Re = 100K, α = 6°

A series of photographs were taken every 30 seconds to document surface oil flow feature development of the BEZ062518513 airfoil at 0° angle of attack and a Re number of 150,000. The photographs are presented in Appendix D. The first noticeable feature was an oil accumulation line at 6.5 cm from the leading edge, recorded at 1 min. At 4 minutes, a change in surface texture became clear and the oil accumulation line was still at 6.5 cm from the leading edge but more pronounced. During the 5th and 6th minutes the features became more pronounced, but did not show any change in location. At 6 minutes the test was complete and measurements were made.

5.4 Validation

An E387 airfoil was chosen for the validation study because of the availability of experimental results. The boundary layer behavior and laminar separation bubble location for the validation data was measured using surface oil flow visualization as well as surface

pressure and hot wire anemometer measurements at two separate wind tunnels. Boundary layer measurements taken in RIT's low speed closed circuit wing tunnel were compared to the known data to determine the validity of the experimental results.

5.4.1   Known Data

A similar validation study performed by Lyon, et al. (1997) that determined the laminar separation bubble location for an E387 airfoil for Re = 200,000. The location was found using surface oil flow visualization in the UIUC wind tunnel. The UIUC wind tunnel has a reported turbulence level less than 0.1%. This data will be referred to as the *UIUC data* form now on. The results were compared to data collected at NASA's Langley Research Center Low-Turbulence Pressure Tunnel (LTPT). The turbulence level of the LTPT was reported to be less than 0.1%. The UIUC data was found to match the LTPT data within 2% chord for locations of laminar separation and reattachment.

5.4.2   Validation Results and Discussion

XFOIL analysis was performed to determine the laminar separation bubble location for an E387 airfoil at Re = 200,000. An Ncrit value of 9 was used to best simulate the reported turbulence level in the LTPT and UIUC wind tunnels. Laminar separation bubble location was found for angles of attack between -2° and 6°, above 6° the laminar separation bubble collapses.

The laminar separation bubble location on an E387 airfoil was found using surface oil flow visualization in the RIT wind tunnel. Results were collected at Re = 200,000 and angles of attack between -2° and 8° for comparison with XFOIL, LTPT, and UIUC results. Figure 5.4 presents the separation and reattachment locations for the four data sets.
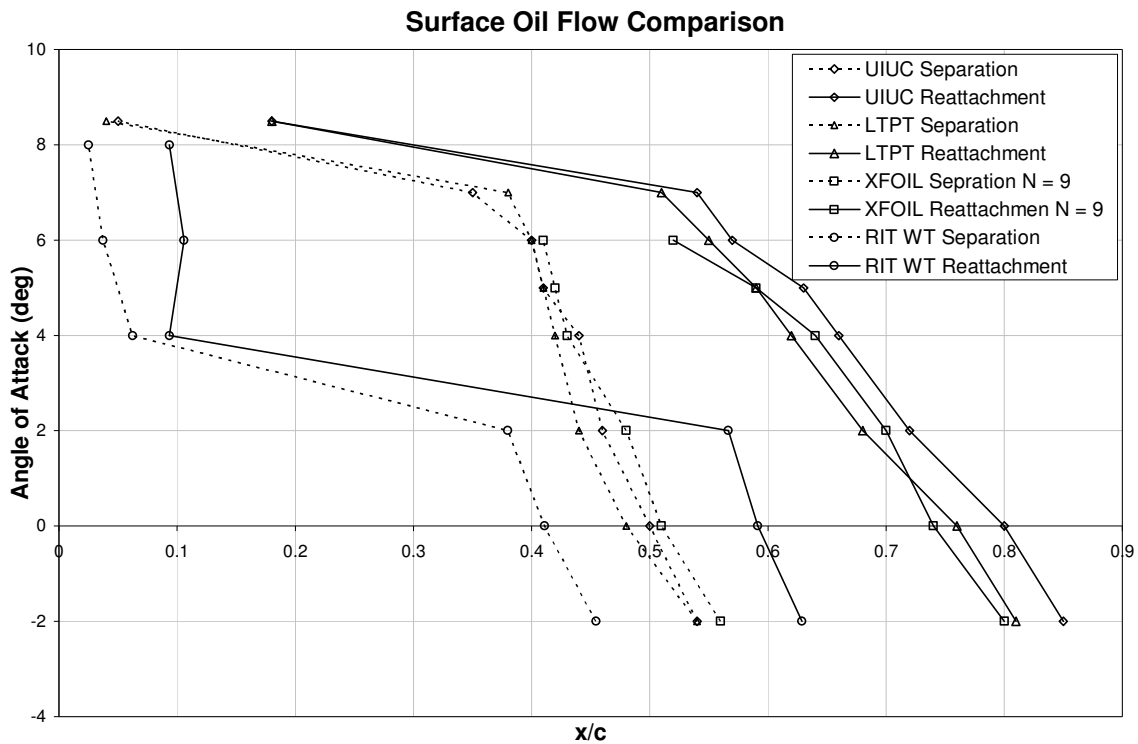
Figure 5.4: Wind Tunnel Results: E387 Validation

The UIUC, LTPT, and XFOIL data correlates well up to 6° angle of attack where XFOIL predicts the laminar separation bubble will burst. XFOIL results were also gathered for Ncrit = 7, but the results showed a shorter laminar separation bubble region than measured in the LTPT and UIUC wind tunnels. The separation and reattachment points measured in the RIT wind tunnel show a very poor correlation to the known results. The boundary layer behavior does exhibits two dominate trends associated with the known errors in the experimental set-up. The major model inaccuracy was an increased leading edge radius caused by the chosen manufacturing process. A larger leading edge radius is associated with earlier boundary layer separation (Greenblatt, Wygnanski 2003). This behavior is evident in the results gathered in the RIT with tunnel. Also, although the turbulence level of the RIT wind tunnel is unknown it is though to be much larger than 0.1% reported for both the LTPT and UIUC wind tunnels. Higher freestream turbulence causes a decrease in laminar separation bubble size by promoting laminar to turbulent transition; a trend also present for the data collected in the RIT wind tunnel.

Due to theses inaccuracies, the results of the validation were deemed inconclusive. The unknown turbulence level of the RIT wind tunnel makes comparison to results obtained at different wind tunnel facilities difficult. The RIT wind tunnel can be a useful tool for comparison and evaluation of results gathered using only the RIT wind tunnel. In addition, XFOIL's ability to model different flow conditions can accommodate various wind tunnel configurations allowing for comparison between XFOIL and the RIT wind tunnel results. This is evident in XFOIL's prediction of separation and reattachment location for the E387 airfoil.

5.5   Surface Oil Flow: Results and Discussion

Laminar separation bubble location was determined for five Bezier airfoils using the surface oil flow visualization technique described previously. The test results were compared to XFOIL predictions using Ncrit = 7 to evaluate XFOIL as a tool to model low Re number boundary layer behavior on Bezier airfoils. Results for Re = 100,000 and 150,000 are presented for two airfoils representative of the best and worst correlation between experimental and analytical data. The complete set of test results is presented in Appendix D.

5.5.1   BEZ032037516

The wind tunnel results for the BEZ032037516 test airfoil at Re = 100,000, presented in Figure 5.5, showed good correlation to the XFOIL predictions. The wind tunnel data, shown in red, was found to separate and reattach at lower x/c values than predicted by XFOIL. This trend was found consistently for all airfoils tested. The length of the laminar separation bubble at all but 4° angle of attack matched the length predicted by XFOIL within the measured uncertainty. At 4° a short leading edge bubble is present in both the wind tunnel and XFOIL results but the effect on the aft boundary layer in the region differs. The decrease

in the aft laminar separation bubble predicted by XFOIL does not occur for the wind tunnel measurements. The collapse of the leading edge bubble occurs at 9° for both the wind tunnel test and XFOIL prediction.
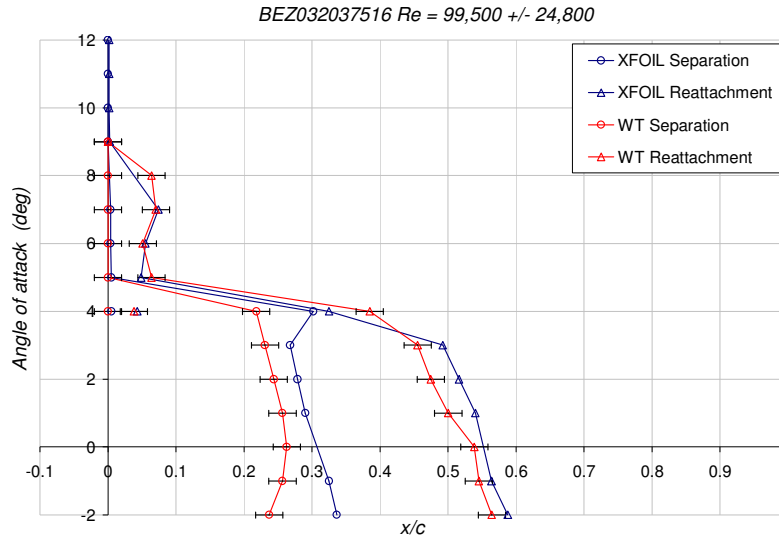
Figure 5.5: Wind Tunnel Results: BEZ032037516, Re=100K

For Re = 150,000, the wind tunnel results depart from the XFOIL predictions. The wind tunnel results suggest the large laminar separation bubble collapses to a short leading edge bubble at a lower angle of attack. This behavior is thought to be the result of a local increase in angle of attack of the airfoil due to circulation effects. A higher velocity is required to achieve the desired Re number which results in higher circulation effects. Circulation causes the streamlines of the core region of flow within the wind tunnel to deflect increasing the local angle of attack of the wing (Barlow, Rae, Pope 1999). At 3° angle of attack XFOIL predicts a very short leading edge bubble, which is on the order of magnitude of the thickness of the leading edge oil accumulation line. The presence of the oil accumulation line limits the smallest leading edge laminar separation bubble that can form. This was an unanticipated error associated with the testing method. The larger bubble contributes to the discrepancy between the XFOIL and wind tunnel results. The comparison is presented in Figure 5.6.
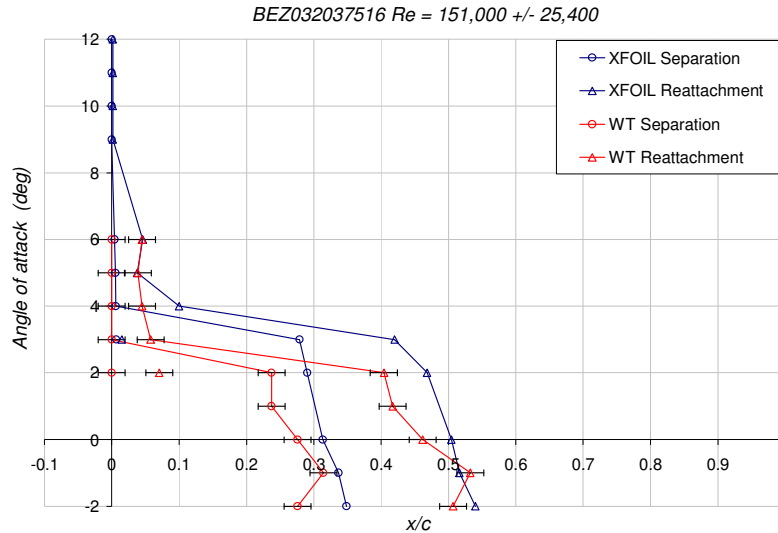
Figure 5.6: Wind Tunnel Results: BEZ032037516, Re=150K

For the tested airfoils with increased camber the trend of earlier separation and reattachment was consistent with the discrepancy between XFOIL and experimental results growing with increased camber. This is attributed with the increased circulation associated with higher lift generation, a predominate performance characteristic of higher cambered airfoils. The size of the laminar separation bubble was always consistent with the XFOIL predictions when no short leading edge laminar separation bubble was present. For the lower cambered airfoils, leading edge laminar separation bubbles were dominate only over a small range of angle of attack that appeared in the transient region as the bubble transition from a more aft location to a short leading edge bubble.

5.5.2   BEZ083018513

The 7% and 8% camber airfoils exhibited strong leading edge laminar separation bubbles over a range of angle of attack. This caused a large discrepancy between the XFOIL predictions and the wind tunnel results. XFOIL predicts, for the 8% camber experimental airfoil, small leading edge laminar separation bubbles for the range of angle of attack from 5° to 9° for both Re numbers tested. XFOIL also predicts large regions of separated flow over

the aft portion of the airfoil which are highly dependent on the short leading edge laminar separation bubble. The wind tunnel model does not form the short leading edge laminar separation bubble and forms a large laminar separation bubble over the mid section of the airfoil chord. Without the transition to turbulent flow occurring near the leading edge, as is the case in the XFOIL predictions, the boundary layer separates prior to the aft region of separated flow predicted by XFOIL. The boundary layer comparisons for the 8% airfoil at Re = 100,000 and 150,000 are presented in Figure 5.7and Figure 5.8.
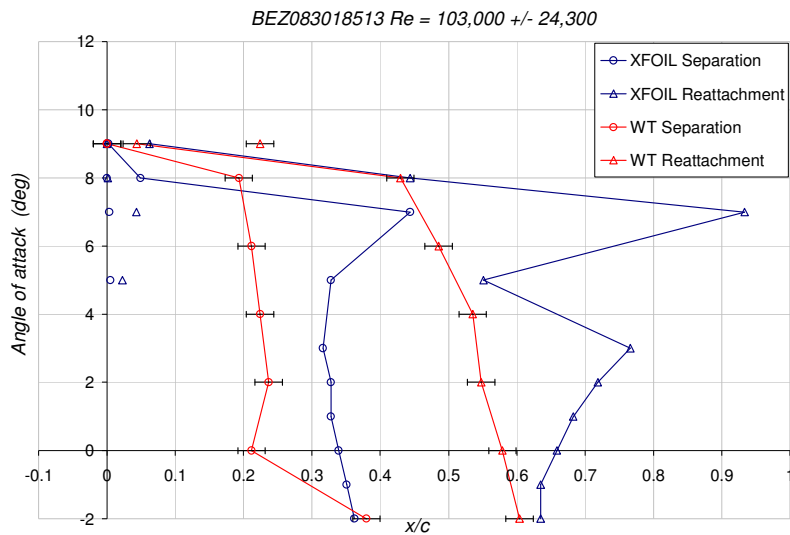
Figure 5.7: Wind Tunnel Results: BEZ083018513, Re=100K
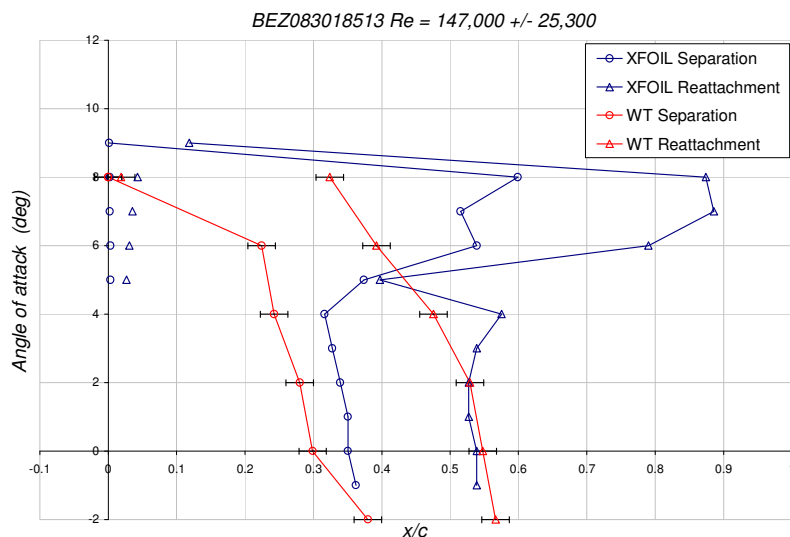
Figure 5.8: Wind Tunnel Results: BEZ083018513, Re=150K

The inability of the higher cambered wind tunnel models to form a leading edge laminar separation bubble is due to the strength of the leading edge bubble. It is thought that a weak leading edge laminar separation bubble is susceptible to collapse with minor changes in flow conditions. The boundary layer shape parameter (H) can be used as an indication of the strength of a laminar separation bubble, with larger H values corresponding to stronger laminar separation bubbles (Drela, Giles 1987). XFOIL predicts leading edge bubbles for both the 3% and 8% camber airfoils at 6° angle of attack, but only the 3% wind tunnel model exhibits a leading edge bubble. The H plot for both airfoils, Figure 5.9, shows that the 3% camber airfoil achieves a maximum H in the leading edge bubble region that is over twice as large as the 8% camber airfoil. The RIT wind tunnel lacks the sophisticated measurement devices required to experimentally verify the shape parameter; however the XFOIL results provide a possible explanation for the poor correlation of the higher cambered test airfoils.
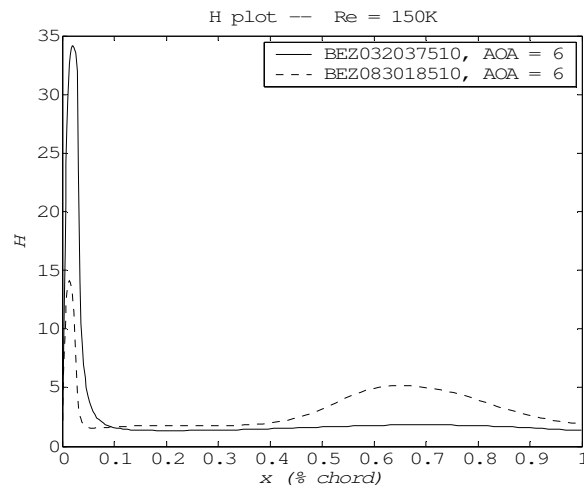
Figure 5.9: H Evaluation, BEZ032037510, BEZ083018510, α=6°

5.5.3 Conclusions

The experimental validation of the E387 airfoil showed no correlation to boundary layer results collected at the LTPT and at the UIUC experimental facilities. The discrepancy is

117

attributed to the difference in flow quality between the two other wind tunnels and the RIT wind tunnel. The turbulence level of the RIT wind tunnel is unknown, but all indicators point to a high turbulence level, which is amplified by poor wind tunnel acoustics. It was determined that any test results gathered from the RIT wind tunnel could not be compared to results gathered at other wind tunnel facilities. XFOIL results for the E387 airfoil, computed at Ncrit = 9 representing a low turbulence level, did accurately predict the boundary layer performance for the other two wind tunnel facilities.

Experimental results for the 5 Bezier experimental airfoils indicate XFOIL can accurately predict boundary layer performance for airfoils with camber values up to 7%, at and above 7% camber the results were inconclusive due to testing inaccuracies. The laminar separation bubble location results for the lower cambered airfoils showed a tendency to transition early, yet maintain a similar bubble size to what was predicted by XFOIL. Streamline curvature caused by circulation and wind tunnel wall effects cause the boundary layer separation location to transition to the leading edge at a lower measured angle of attack. XFOIL predicted the higher cambered airfoils would exhibit weaker leading edge laminar separation bubbles which have a substantial effect on the aft portion of the boundary layer. Fluctuation in freestream velocity and other testing inaccuracies are considered the reason for the absence of the leading edge bubbles for the higher cambered test airfoils. The lack of the leading edge bubble resulted in poor comparison between the test results and XFOIL's predications.

6 Conclusions

This chapter presents a summary of the general conclusions from the results of the analysis and testing in the first section. Conclusions addressing the relation of the various airfoil shape parameters and the airfoil performance are presented in the second section. In the third section conclusions from the wind tunnel testing results are discussed. The final section covers recommendations for future work.

6.1 General Conclusions

Using previous research and a detailed comparison of analytic and experimental results it was concluded that XFOIL is able to predict the relative performance of various low Re number airfoils with accuracy. XFOIL's results proved useful in determining the correlations between changes in airfoil shape parameters and performance characteristics. The boundary layer data provided by XFOIL was effective in determining the underlying cause for differences in airfoil performance for different shape parameters. The results were easily implemented into an airfoil design methodology that focuses on improving a specific airfoil performance characteristic.

The experimental validation showed the RIT wind tunnel was unable to match the flow conditions of other test facilities. The discrepancy in flow characteristics between the RIT wind tunnel and the UIUC and LTPT wind tunnels makes the testing results specific to the RIT wind tunnel. The experimental testing from the RIT wind tunnel indicates that XFOIL, set to model increased freestream turbulence levels, can accurately predict boundary layer behavior for less severely cambered airfoils. For higher cambered airfoils, the wind tunnel results depart from the XFOIL predictions, with the discrepancy attributed to testing inaccuracies.

119

6.2 Conclusions: Analysis

After review of the XFOIL results, several conclusions are drawn.

- It was determined that the discontinuity in the lift curve that appears in the XFOIL results is consistent with the expected boundary layer behavior and is an accurate prediction of airfoil C_l performance.
- The XFOIL solution parameters chosen for the analysis results in a timely solution and an acceptable level (9.5%) of rejected polar files due to unconverged solutions.

The analysis results show a number of trends associated with changes in the airfoil shape parameters of max camber (C), position of max camber (xC), max reflex (R), position of max reflex (xR), and thickness (T) on $C_{l,max}$ and α_{stall}.

- A weak interdependence between C, xC, and xR was found for $C_{l,max}$ and α_{stall}.
- A direct correlation was found between C and both $C_{l,max}$ and α_{stall}, with increases in C causing an increase in $C_{l,max}$ and α_{stall}.
- An indirect correlation was found between xC and both $C_{l,max}$ and α_{stall}, with increases in xC causing an increase in $C_{l,max}$ and α_{stall}.
- An increase in xR results in an increase in $C_{l,max}$ with no effect on α_{stall}.
- Changes in R have no effect on $C_{l,max}$ or α_{stall}.
- Changes in airfoil thickness result in only changes in magnitude of $C_{l,max}$ and α_{stall}. No changes in trends were found.

The analysis results show a number of trends associated with changes in the airfoil shape parameters C, xC, R, xR, and T on $C_l/C_{d,max}$ and $\alpha_{Cl/Cd,max}$.

- A strong interdependence between C, xC, and xR was found for $C_l/C_{d,max}$ and $\alpha_{Cl/Cd,max}$.
- Low C and xC values results in the highest $C_l/C_{d,max}$ values for low xC values.

- An increase in xC shifts the trends associated $C_l/C_{d,max}$ to higher C values, transitioning the airfoils with the lowest $C_l/C_{d,max}$ values to the highest.
- Holding C and xC constant, increasing xR and decreasing R cause increases of similar magnitude in $C_l/C_{d,max}$.
- The results showed a direct correlation between C and $\alpha_{Cl/Cd,max}$.
- An indirect correlation between xC and $\alpha_{Cl/Cd,max}$ was present in the results.

The results provided a measure of the range of performance values associated with changes in airfoil shape parameters.

- Changes in C and xC cause a 40% variation of $C_{l,max}$ and 40% variation of α_{stall}.
- Changes in R and xR cause a 15% variation of $C_{l,max}$ with no significant variation in α_{stall}.
- Changes in C and xC cause a 30% variation of $C_l/C_{d,max}$ and 50% variation of $\alpha_{Cl/Cd,max}$.
- Changes in R and xR cause a 20% variation of $C_l/C_{d,max}$.

The XFOIL analysis provides sufficient data to accurately predict the relative performance of the various combinations of airfoil shape parameters. The boundary layer data provided by XFOIL also provides a foundation for determining why the trends take the form they do. The missing data caused by unconverged XFOIL solutions hade little to no effect on the analysis. The range of airfoil shape parameters provided an accurate portrait of all the possible airfoils with the parameter limits exhibiting degraded boundary layer performance.

6.3 Conclusions: Testing

A number of conclusions are drawn from the results of the surface oil flow visualization validation results. The validation relied on a comparison of the boundary layer behavior on the upper surface of an E387 airfoil between the RIT wind tunnel and data collected in the

University of Illinois at Urbana-Champagne (UIUC) wind tunnel and the low turbulence pressure tunnel (LTPT) at NASA's Langley research center.

- The discrepancy between the flow quality in the RIT wind tunnel and the UIUC and LTPT wind tunnels is considered the primary source for the discrepancy between the location of boundary layer features such as laminar separation and reattachment.
- E387 model inaccuracies, specifically the leading edge radius, account for a portion of the discrepancy between the RIT wind tunnel results and the UIUC and LTPT wind tunnel results.
- The turbulence level of the RIT wind tunnel is unknown, but the results indicate it is higher than the turbulence level reported for the UIUC and LTPT wind tunnels.
- The conclusion of the validation was that boundary layer observations made in the RIT wind tunnel could not be compared to other facilities.
- XFOIL is able to accurately predict boundary layer behavior for the UIUC and LTPT wind tunnels using an Ncrit value of 9.

The results for the location of boundary layer separation and reattachment for a series of five Bezier airfoils provide insight into the ability of XFOIL to predict boundary layer behavior for thin/cambered/reflexed airfoils.

- The wind tunnel results compare well to the XFOIL predictions for the airfoils tested with camber values less than 7%. XFOIL predicts these airfoils will have a strong leading edge laminar separation bubble (relatively high maximum boundary layer shape parameter H over the range of the bubble).
- Results for the tested airfoils with camber values of 7% and greater showed poor correlation to XFOIL predictions attributed to the inability of the wind tunnel model to exhibit leading edge laminar separation bubble formation. XFOIL predicts the leading edge bubbles present at various angles of attack will be weak (relatively low maximum boundary layer shape parameter H over the range of the bubble).

- It is believed that the weak leading edge laminar separation bubbles, which are highly sensitive to changes in freestream conditions, are not able to form in the RIT wind tunnel.
- For the less cambered airfoils, separation occurs a short distance forward of the location predicted by XFOIL. The discrepancy grows with increasing freestream velocity and camber.
- The difference in separation location is caused by streamline curvature which causes the local angle of attack of the freestream and test airfoil to be larger than the measured angle of attack. This is a known result of the interaction of circulation and wind tunnel wall effects.

The large discrepancy between the RIT wind tunnel results for the E387 airfoil and the measured results from the UIUC and LTPT wind tunnels limits the testing results from being applied beyond future RIT wind tunnel tests. The results for less severely cambered Bezier airfoils provide an indication of XFOIL's ability to model boundary layer phenomena.

6.4 Recommendations for Future Work

Future work should focus on developing more detailed wind tunnel testing results. A detailed investigation of the weak laminar separation bubbles predicted by XFOIL would greatly expand the understanding of the foundation of the increased performance present for higher cambered airfoils. Future research would also benefit greatly from the development of a mechanical system that could vary the shape of an airfoil during testing. The mechanism would allow for the development of a control system that could allow for in-flight adaptation of the wing to take advantage of the different performance characteristics found during the current research.

The next important step in improving the aerodynamics of thin/cambered/reflexed airfoils is to improve the lower surface boundary layer performance by designing an optimized leading edge faring. The leading edge faring promotes attached flow over the lower surface of the

airfoil near the leading edge which greatly reduces drag and improved lift at lower angles of attack. A leading edge faring could be applied to any of the airfoil shapes presented in the current research to improve the $C_{l,max}$ and $C_l/C_{d,max}$ performance.

REFERENCES

Albertani, Roberto, Barnswell, Paul, Boria, Frank, Claxton, Clifton, James [2004]. University of Florida Biologically Inspired Micro Air Vehicles. *8th International Micro Air Vehicle Competition*, May 20-21.

Barlow, Jewel, Rea, William, Pope, Alan [1999]. Low-Speed Wind Tunnel Testing. Wiley. New York.

Boreren, Andy, Bragg, Michael [2001]. Unsteady Stalling Characteristics of Thin Airfoils at Low Reynolds Number. Fixed and Flapping Wing Aerodynamics for Micro Air Vehicle Applications, *Progress in Astronautics and Aeronautics*, Vol. 195. Thomas Mueller (Editor).

Brendel, M, Mueller, Thomas J. [1988]. Boundary-Layer Measurements on an Airfoil at Low Reynolds Numbers. *Journal of Aircraft*, Vol. 25, No. 7, pp. 612-617.

Carmichael, B.H. [1981]. Low Reynolds number Airfoil Survey. *NASA Contractor Report*, Vol. I, No. 165803.

Crompton, M.J., Barrett, R.V. [2000]. Investigation of the Separation Bubble Formed Behind the Sharp Leading Edge of a Flat Plate at Incidence. *Proceedings of the Institution of Mechanical Engineers, Part G: Journal of Aerospace Engineering*, Vol. 214, No. 3.

Drela, M [1987] Two-Dimensional Transonic Aerodynamic Design Method. *AIAA Journal*, Vol. 25 No. 8: pp. 199-1206.

Drela, M [1989]. XFOIL: An Analysis and Design System for Low Reynolds Number Airfoils. *Conference on Low Reynolds Number Airfoil Aerodynamics*, University of Notre Dame, June 10-14.

Drela, M [2000] "XFOIL 6.9 User Primer" XFOIL: Subsonic Airfoil Development System. Mark Drela. December 11. Massachusetts Institute of Technology. Aug. 1, 2005. <http://web.mit.edu/drela/Public/web/xfoil/>.

Drela, M, Giles, Michael B [1987]. Viscous-Inviscid Analysis of Transonic and Low Reynolds Number Airfoils. *AIAA Journal*, Vol. 25, No. 10, pp. 1347-1355.

Gopalarathnam, Ashok, Broughton, Benjamin A, McGranahan, Bryan D, Selig, Michael S [2001]. Design of Low Reynolds Number Airfoil with Trips. *19th Applied Aerodynamics Conference*, June 5-6.

Greenblatt, D, Wygnanski, I [2003]. Effect of Leading-Edge Curvature on Airfoil Separation Control. *Journal of Aircraft*, Vol. 40, No. 3, pp. 473-481.

Grundy, T,Keefe, P, Lowson, M [2001]. Effects of Acoustic Disturbances on Low Re Aerofoil Flows. <u>Fixed and Flapping Wing Aerodynamics for Micro Air Vehicle Applications.</u> *Progress in Astronautics and Aeronautics*, Vol. 195. Thomas Mueller (Editor).

Jenkins, D, Shyy, Wei, Sloan, Jason, Klevebring, Fredrik, Nilsson, Mikael [1998]. Airfoil Performance at Low Reynolds Numbers for Micro Air Vehicle Applications. *Thirteenth Bristol International PRV/UAV Conference*, University of Bristol.

Kellogg, Michael [2004]. Parametric Design Study of the Thickness of Airfoils at Reynolds Numbers from 60,000-150,000. *42nd AIAA Aerospace Sciences Meeting and Exhibit*. pp. 6508-6515.

Kreyszig, Erwin [1999]. <u>Advanced Engineering Mathematics</u>. John Wiley & Sons, Inc., 8th Edition. New Jersey.

Levin, Ori, and Shyy, Wei [2001]. Optimization of a Flexible Low Reynolds Number Airfoil. *39th Aerospace Sciences Meeting and Exhibit*, Reno, NV, Jan. 8-11.

Lian, Yongsheng, Shyy, Wei, Viieru, D, Zhang, B [2003]. Membrane Wing Aerodynamics for Micro Air Vehicles. *Progress in Aerospace Sciences*, Vol. 39, No. 6. pp.425-465.

Lyon, Christopher A, Selig, Michael S, Broeren, Andy P [1997]. Boundary Layer Trips on Airfoils at Low Reynolds Numbers. *35th Aerospace Sciences Meeting and Exhibit*, Reno, NV, Jan. 6-9.

Gad-el-Hak, Mohamed [1989]. Control of Low-Reynolds-number Airfoils: A Review. <u>Lecture Notes in Engineering,</u> Vol. 54. Low Reynolds Number Aerodynamics: Proceedings of the Conference, 5-7 June 1989. Ed. Thomas J Mueller. Notre Dame, Indiana, USA: Springer-Verlag. pp. 246-70.

Mueller, Thomas J [1999]. Aerodynamics Measurements at Low Reynolds Numbers for Fixed Wing Micro-Air Vehicles. *RTO AVT/VKI Special Course on Development and Operation of UAVs for Military and Civil Applications*. VKI, Belgium, September 13-17.

Mueller, Thomas J, DeLaurier, J [2003]. Aerodynamics of Small Vehicles. *Annual Review of Fluid Mechanics*, Vol. 35. pp. 89-111.

Nickel, Karl, Wohlfahrt, Michael [1994]. Tailless Aircraft in Theory and Practice. American Institute of Aeronautics and Astronautics, Washington, DC.

Null, W, Shkarayev, S [2004]. Effect of Camber on the Aerodynamics of Adaptive Wing Micro Air Vehicles. *2nd AIAA Flow Control Conference*, Portland Or., June 28-July 1.

Pelletier, Alan, Mueller, Thomas J [2000]. Low Reynolds Number Aerodynamics of Low-Aspect-Ratio Thin/Flat/Cambered-Plate Wings. *Journal of Aircraft*, Vol. 37, No.5. pp. 825-832.

Santhanakrishnan, Arvind, Pern, Nan J, Jacob, Jamey D [2005]. Optimization and Validation of a Variable Camber Airfoil. *46th AIAA/ASME/ASCE/AHS/ASC Structures, Structural Dynamics and Materials Conference*, Apr 18-21.

Scarbrough, William T [1992]. "NACA Four-Digit Airfoil Section Generation Using Cubic Parametric Curve Segments and the Golden Section." Thesis: Rochester Institute of Technology.

Schmidt, Gordon S, Mueller, Thomas J [1989]. Analysis of Low Reynolds Number Separation Bubbles Using Semiempirical Methods. *AIAA Journal*, Vol. 27, No. 8. pp. 993-1001.

Selig, MS, Lyon, CA, Giguère, P, Ninham, CN, and Guglielmo, J [1996]. Summary of Low-Speed Airfoil Data, Vol. 2, SoarTech Publications, Virginia Beach, VA.

Shkarayev, S, Jouse, W, Null, W, Wagner M [2003]. Measurement and Performance Prediction of an Adaptive Wing Micro Air Vehicle. *Society of Optical Engineering*, V5054.

Shreve, Joshua [2005], "Modification of a Longitudinal Wind Tunnel Balance for Identification of Micro Air Vehicle Instabilities." Thesis: Rochester Institute of Technology.

Signh, A, Winoto, S, Shah, D, Lim, K, Goh, R [2000]. A Computational Study on Airfoils at
Low Reynolds Numbers. *Proceedings of the ASME Fluids Engineering Division
(FED)*, Vol. 253. pp. 405-411.

Torres, Gabriel E, Mueller, Thomas J [2004]. Low-Aspect-Ratio Wing Aerodynamics at Low
Reynolds Numbers. *AIAA Journal*, Vol. 42, No.5. pp. 865-873.

Viieru, Dragod, Lain, Yongsheng, Shyy, Wei, Ifju, Peter [2003]. Investigation of Tip
Vortices on Aerodynamic Performance of a Micro Air Vehicle. *33rd Fluid Dynamics
Conference and Exhibit*, Oct. 21-24.

Yarusevych, Serhiy, Sullivan, Pierre E , Kawall, John G [2005]. Airfoil Boundary Layer and
Wake Development at Low Reynolds Numbers. *35th AIAA Fluid Dynamics
Conference and Exhibit*, Toronto, Ontario, June 6-9.

APPENDIX A

THIN/CAMBERED/REFLEXED AIRFOIL DEVELOPMENT FOR MICRO AIR VEHICLE APPLICATIONS AT REYNOLDS NUMBERS OF 60,000 TO 100,000

Michael R. Reid and Dr. Jeffrey Kozak
Rochester Institute of Technology, Rochester, New York

Abstract:

Airfoil development for micro-air vehicle applications is dominated by laminar separation bubble formation. XFOIL, a low Reynolds number airfoil analysis tool is utilized in an effort to understand and document the role camber plays in laminar separation bubble formation, size, and location. In addition, the direct effect camber has in the production of lift and drag is evaluated through assessment of the maximum coefficient of lift and maximum coefficient of lift/coefficient of drag attained by airfoils of varying camber. Camber values of 1, 2, 3, 4, 5, 6, 7, 8, and 9% chord are evaluated at Reynolds numbers of 60,000, 80,000, and 100,000 for angles of attack over a range from 0 to 10 degrees. Results show a direct relationship between the camber and maximum coefficient of lift with a growing dependence on Reynolds number at higher camber values. Maximum coefficient of lift / coefficient of drag showed a peak in performance for mid to high range camber values and a low dependency on Reynolds number.

Nomenclature:

C_l = Coefficient of lift (2-D)
$C_{l,max}$ = Maximum coefficient of lift (2-D)
C_d = Coefficient of drag (2-D)
$C_l/C_{d,max}$ = Coefficient of lift/Coefficient of drag Max
C_f = Coefficient of friction (2-D)
x/c = chord location
Re = Reynolds number
LSB = Laminar separation bubble
MAV = Micro-air vehicle

Introduction/Motivation:

Within the past 10 years a new regime of aircraft has been rapidly immerging as a viable option in short range surveillance and reconnaissance missions. These aircraft, referred to as micro-air vehicles (MAV) are characterized by a maximum linear dimension on the scale of 0.20 to 0.50 m and flight speeds in the range of 5 to 20 m/s. These aircraft experience aerodynamic phenomena dominated by low Reynolds number effects because of their small size and slow flight speed. The exact range of Re numbers that are considered low is a relative measure, but for the purpose of this research values in the range of 60,000 to 100,000 will be addressed. In light of the continual effort to design smaller aircraft, this range was chosen to represent the near future of MAV development. In addition, previous research[1,6] has recognized that Re numbers below 50,000 cause a drastic reduction in airfoil performance.

Technical Background:

Airfoils operating at low Re numbers experience laminar separation bubble (LSB) formation which degrades overall airfoil performance through loss of lift and increased drag. Laminar separation is caused when laminar flow encounters an adverse pressure gradient, generally near or at the start of pressure recovery on the upper surface of the airfoil, and lacks the flow momentum to overcome the gradient[6,7,3]. For the resulting separated flow, transition to turbulent flow and reattachment is highly dependent on Re number, freestream turbulence, surface roughness,

surface curvature, and pressure distribution[6]. If the separated boundary layer reattaches the resulting vortex structure is referred to as a LSB. Do to viscid instability the LSB acts as a natural trip to turbulent flow and the resulting boundary layer flow is able to overcome any additional adverse pressure gradient with less chance of separation. The ideal case for an airfoil with a LSB is when the bubble covers only 2-4% chord, referred to as a short bubble[6]. This structure, unlike a long bubble which covers large portions of an airfoil, has little effect on lift generation while still acting as a laminar to turbulent trip[6].

Initial low Re number airfoil research used traditional airfoils that had been successful at higher Re applications, but results showed low lift generation with high drag. For example, airfoils such as the NACA 0025 show signs of laminar separation at all angles of attack at a Re number of 100,000, whereas the NACA 0012 airfoil only shows signs of trailing edge separation at 10 degrees angle of attack[8]. To address the poor performance of thick airfoils many researchers used thin airfoils with thickness to chord ratios in the range of 2-12%. In a study done by Kellogg[9], 5 airfoils of various thicknesses were tested at Re numbers of 60,000, 100,000, and 150,000. The results of the testing showed for laminar flow the thinner airfoils had 9% higher L/D values and for turbulent conditions thin airfoils had 22% higher L/D values. This not only shows the advantages of thin airfoils but the need for an efficient turbulent trip to ensure the airfoils experience turbulent boundary layer flow. Jenkins[7] also reports similar results for thin airfoils on the order of 6% thickness, out performing thicker airfoils at low Re numbers with the discrepancy between thin and thick airfoil performance becoming greater at very low Re numbers. These studies do not isolate thickness as their only test variable, general airfoil shape varied for the thicknesses tested so an exact correlation between airfoil performance and thickness was not theorized.

In an effort to address and reduce the effects of LSB formation many designers have considered artificial flow trips placed near the leading edge of the airfoil. The intent is to trip the laminar flow so that it can overcome any adverse pressure gradient that it may encounter[10,11]. In both studies tripping the flow did help reduce the size and effects of a LSB, but it was unable to produce a tripped airfoil that performed as well as an airfoil that did not have a large LSB[10].

Camber plays an important role in low Re number airfoil performance. As camber increases lift/drag (L/D) increases while at low Re number performance generally suffers[12]. The foundation of this relationship is the increase in curvature as camber increases. The increased curvature causes greater suction on the upper surface of the airfoil, and consequently greater lift but with an increased pressure gradient causing laminar separation. This trade off suggests an optimum camber for a specific Re number. Null and Shkarayev[12] conducted an investigation of a wing whose airfoil was generated from the top surface of a S5010 airfoil with max camber at 24% chord. Their results showed 3% camber yields the best L/D value while 9% camber produced higher maximum lift with the penalty of greater drag. They also report that stall angle of attack decreases as camber increases. Both results are consistent with LSB phenomena.

Airfoil Development:

In an effort to isolate and examine the effects of camber, a method for creating airfoils based on max camber, position of max camber, max reflex, and position of max reflex values was developed. The method utilizes a Bezier curve to create the mean camber line of the airfoil. Bezier curves were chosen because of their flexibility and reliability in producing a smooth curve. A MATLAB routine solves for the necessary control point locations so that the resulting Bezier curve matches the mean camber line of the desired airfoil as defined by the parameters listed above. An example of a Bezier airfoil with its defining control points is shown in Figure 1.
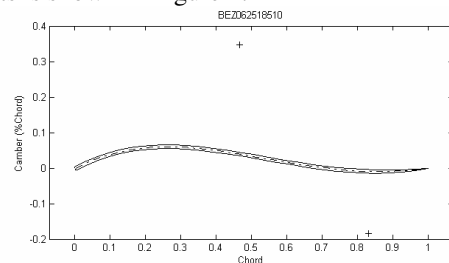
Figure 1

Similar efforts have been pioneered using an nth order polynomial to define an airfoil's mean camber line[14]. The disadvantage of this method is an inability to smoothly connect all possible airfoil parameters without requiring a large number of higher order terms. Each Bezier airfoil is defined by 5 parameters, max camber, position of max camber, max reflex, position of max reflex, and thickness. The thickness distribution is constant with a circular leading edge and a parabolic trailing edge. For simplicity all airfoils generated with a

Bezier function for this research follow the same naming convention, i.e. BEZ062518510. This represents an airfoil that has 6% camber at 25% chord, 1% reflex at 85% chord, and is 1% thick; note that the final value is 10 times the thickness in %chord.

XFOIL:

For low Re number airfoil analysis, previous research[9] has shown XFOIL[13] provides a sufficient tool for modeling LSB formation, as well as providing acceptable results for lift and drag. XFOIL has been reported to over-predict lift and under-predict drag; however this trend has been found consistently and does not affect XFOIL comparison studies[9]. For LSB location, a method suggested by Gaplarathnam[10] relies on where the skin friction coefficient (C_f) is 0 or negative. Regions of negative surface friction are characteristic of LSBs and allow for an easy determination of the start and end of a LSB.

Analytic Results:

Preliminary analysis was conducted using XFOIL on airfoils with max reflex of 1% at 85% chord, thickness of 1% chord, and max camber at 25% chord for camber values of 1% through 9% in 1% chord increments. Data was collected for all camber values at Re numbers of 60,000, 80,000 and 100,000 and angles of attack from -5° to 15° in 0.2° increments. In addition, boundary layer parameters were gathered for angles of attack from 0° to 10° at increments of 2°.

Maximum C_l/C_d results for the various chord and Re number values, presented in Figure 2, show drastic reduction in $C_l/C_{d,max}$ values at camber values greater than 5% camber. The 5% camber airfoil has the highest $C_l/C_{d,max}$ value of 42 for a Re number of 80,000 and a value of 38 for Re numbers of 60,000 and 80,000 which shows only a slight dependency on Re number. 1% thru 3% are notable because of there very low dependency on Re number, though poor $C_l/C_{d,max}$ performers. The 6% camber airfoil shows high dependency on Re number and represents a boundary in performance. For camber values above 6% there is a high dependency on Re number with increased relative performance at higher Re number. Increases performance with increasing Re was expected, however for camber values that produce the highest $C_l/C_{d,max}$ values, 4% and 5% camber, there appear to be a jump in performance for the middle Re number studied.
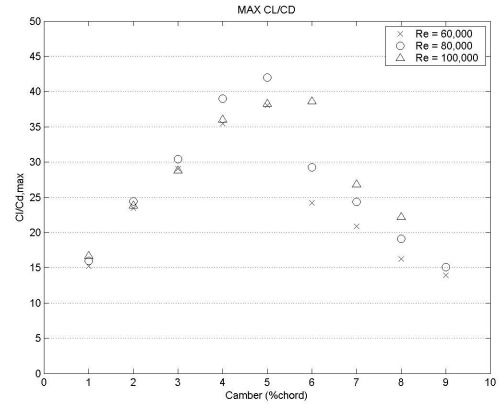
Figure 2

Maximum C_l represents the upper limit of airfoil performance. Figure 3 shows the relationship between camber and $C_{l,max}$. For camber values from 1% to 3% there is only a slight increase in $C_{l,max}$, however over the range of 3% to 7% camber there is a direct correlation between increasing camber and increasing $C_{l,max}$. Above 7% camber the relationship breaks down and 9% camber shows a slight decrease in $C_{l,max}$ from 8% camber. Only the 8% camber airfoil shows a dependency on Re number, the other airfoils show matched performance at all three Re numbers.
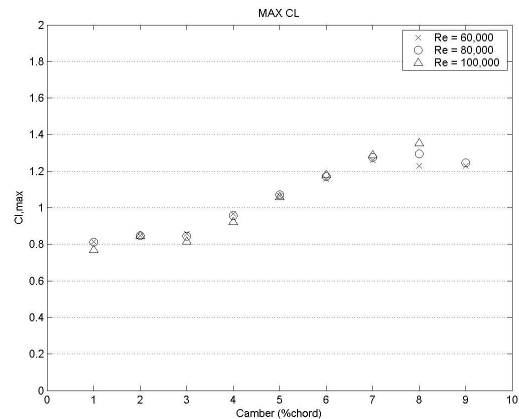
Figure 3

These results represent a range of airfoil options for various performance requirements. Aircraft that need to perform missions that cover long distances would require an airfoil with a camber value around 5% representing the most lift production with smallest drag penalty. High speed missions could be performed by airfoils with camber values of 2% or 3% because of there low drag properties as seen by their high $C_l/C_{d,max}$ values and relatively low $C_{l,max}$ values.

In addition to $C_l/C_{d,max}$, and $C_{l,max}$, LSB location was studied. Utilizing C_f vs. chord location (x) data gathered through XFOIL analysis, LSB location was determined for the 9 camber values at Re numbers of 60,000, 80,000, and 100,000. Figures 4 thru 10 represent the x-location along the airfoil chord of the LSB on the upper surface as a function of camber and Re number. The LSB is found in-between two similar symbols. In cases where the LSB burst and does not reattach, the corresponding symbol is placed at a value of 1, the trailing edge of the airfoil. In cases where a short bubble is formed and another bubble is formed further aft, two sets of symbols are presented.

For angles of attack of 0° and 2° and camber values less than 6%, LSB size is independent of camber while highly dependent on Re number with higher Re values yielding smaller LSBs. In addition the starting location of the LSB moves forward, approaching the max camber point with increasing camber values. Only at the higher camber values does the LSB burst, and fail to reattach. For angles of attack greater than 2° four different types of LSBs are present. LSBs that cover between 20% and 80% of the upper surface of the airfoil, but start aft of the leading edge are referred to as Type I bubbles. Type I are predominant at all camber values for low angles of attack, as seen in figures 4 and 5. Type II, which are characterized by bubbles that start at the leading edge of the airfoil and cover between 20% and 80% characterizes poor flow characteristics. Type III are LSBs that start at the leading edge and cover only a small portion, 5% to 15%, of the upper surface. Type III bubbles are generally known as short bubbles and act as a transition mechanism for laminar flow and represent the best case for a LSB. Type IV bubbles are between 20% and 80% chord and form aft of a type III bubble. In general as angle of attack increases type III bubbles occur at higher camber values. For a given angle of attack camber values above those exhibiting type III bubbles generally have large type I bubbles or separated flow starting just aft of the maximum camber point. At camber values less than those exhibiting type III bubbles, either fully separated flow starting at the leading edge develops or Type II bubbles dominate.

These results explain the behavior of $C_l/C_{d,max}$, and $C_{l,max}$ and again provide insight on which airfoils would perform best in certain missions. The key to top performance is to operate at or near a flight condition where a type III bubble is present. The results show this occurs at low angles of attack for small camber values and higher

angles of attack for larger camber values. This explains the higher $C_l/C_{d,max}$ at lower $C_{l,max}$ exhibited by slightly cambered airfoils, and the higher $C_l/C_{d,max}$ at higher $C_{l,max}$ performance shown by the highly cambered airfoil. It is clear that performance begins to decline at or above 8% camber for all angle of attack because they never achieve a type III LSB.
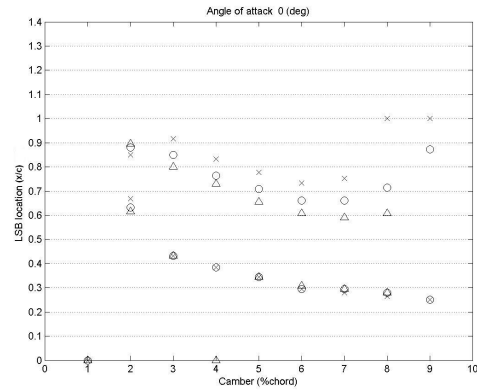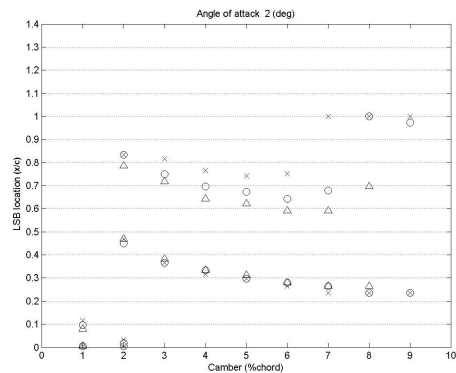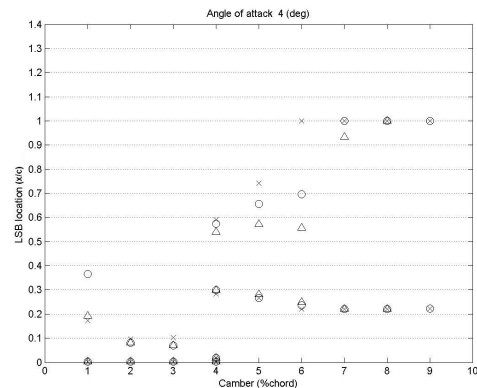

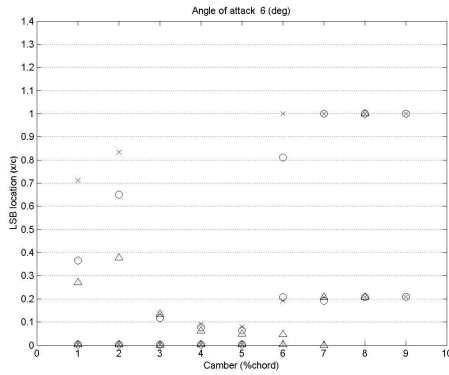*Figure 4*

Figure 5

Figure 7

Figure 8
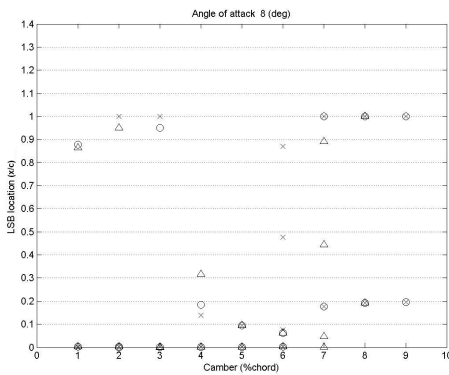
Figure 9
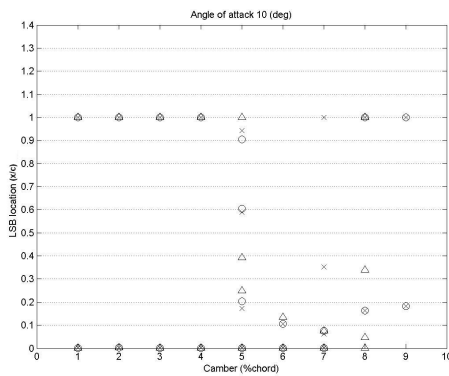
Figure 10

Experimental Results:

In an effort to verify LSB formation and location, surface oil flow visualization was conducted on a BEZ062518510 airfoil model. The model was constructed out of 2 layers of 0°-90° Carbon fiber composite with 0.5 cm grid paper covered with a layer of fiberglass and epoxy on the upper surface. The model has a rectangular planform with a 0.26m span and 0.13m chord. The leading edge, trailing edge, and upper surface were wet sanded, creating a smooth surface finish. With an aspect ratio of 2.00, the model's center section

is not affected by tip vortices at moderate angles of attack and provides similar results to a 2D airfoil case[2]. Dow Corning 200® fluid was mixed with orange pigment in a 10:1 mass ration and applied to the upper surface of the airfoil with a sponge brush. The model was then placed in RIT's closed circuit subsonic wind tunnel, which was quickly brought up to speed. Re numbers of 60,000 and 100,000 were tested at 0, 5, and 10 degrees angle of attack. Tunnel run time necessary to form discernable oil features varied from 5 to 50 minuets depending on the Re number and angle of attack. As described in previous research[11], the laminar separation point is distinguish by a change is surface texture and reattachment by the subtle changes in texture aft of the oil accumulation line (See Figure 11). The grid paper applied to the upper surface was used as a measurement of the separation and reattachment points while the model was still in the test section. This reduces any changes in the oil due to tunnel rundown.
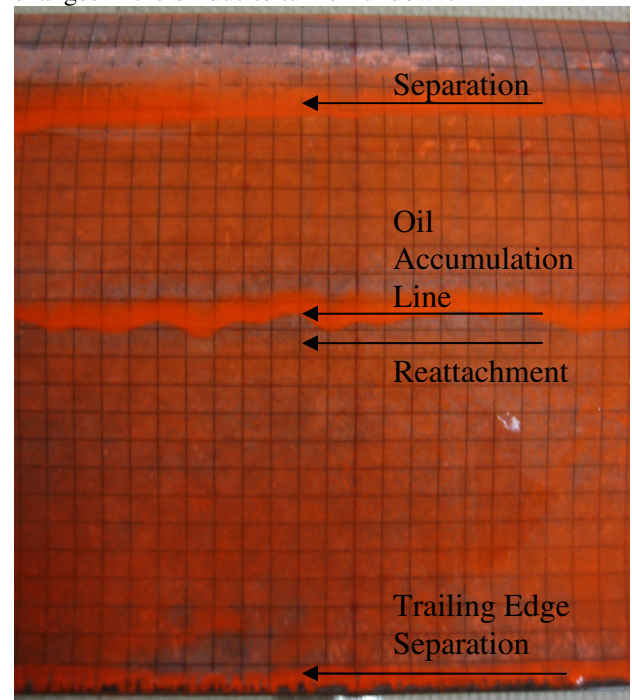
*(Figure 11: Surface Oil Flow Visualization,
Re = 100,000 α = 10°)(Color Photo)*

Initial results show poor agreement with analytical results at angles of attack of 5 and 10 degrees for a Re number of 60,000 and 10 degrees for a Re number of 100,000. In general the LSB seems much less sensitive to changes in angle of attack and Re number than predicted by XFOIL. Tip vortices may not cover the center portion of the wing, but their presence may be causing the poor

133

results, at higher angles of attack. Additional testing with higher aspect ratio wings is necessary to verify effects of tip vortex structure on LSB formation. Figures 12 and 13 represent a comparison between XFOIL results and surface oil flow visualization.

Re = 60,000
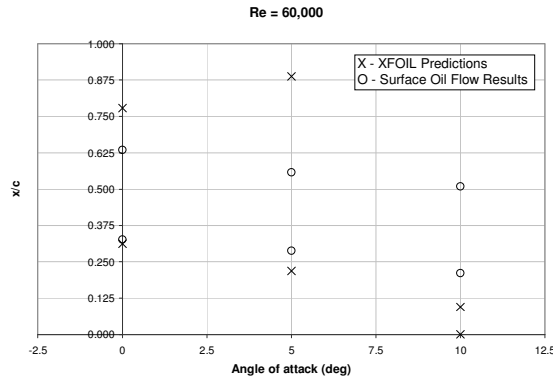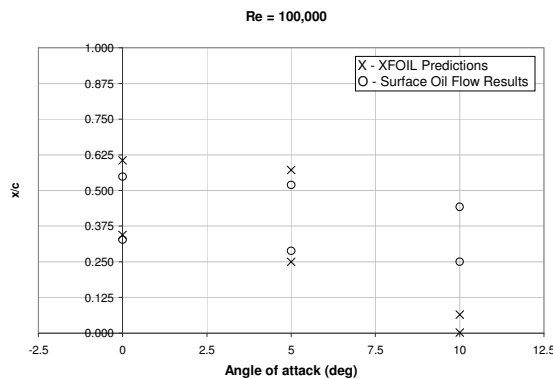
(Figure 12)

Re = 100,000

(Figure 13)

Conclusions:

- 5% camber produced the highest $C_l/C_{d,max}$ of 42 at a Re number of 80,000.
- 8% camber produced the highest C_l of 1.35 at a Re number of 100,000.
- Between 3% and 8% camber there is a direct relationship between camber and $C_{l,max}$.
- Between 1% and 5% camber there is a direct relationship between camber and $C_l/C_{d,max}$.
- Above 5% camber $C_l/C_{d,max}$ has a drastic reduction in performance.

References:

[1] Sathaye, S., Yuan, J., and Olinger, D. "Lift Distributions on Low-Aspect-Ratio Wings at Low Reynolds Numbers for Micro-Air Vehicle Applications." 22nd Applied Aerodynamics Conference and Exhibit, Providence, Rhode Island, Aug. 16-19, 2004.

[2] Lian, Yongsheng, Shyy, Wei, Viieru, Dragos, and Zhang, Baoning. "Membrane Wing Aerodynamics for Micro Air Vehicles." Progress in Aerospace Sciences, Vol. 39 (2003). 426-465.

[3] Levin, Ori, and Shyy, Wei. "Optimization of a flexible low Reynolds number airfoil." Aerospace Sciences Meeting and Exhibit, 39th, Reno, NV, Jan. 8-11, 2001.

[4] Viieru, D., Lian, Y., Shyy, W., and Ifju, P. "Investigation of Tip Vortex on Aerodynamic Performance of a Micro Air Vehicle." 33rd AIAA Fluid Dynamics Conference and Exhibit, Orlando, Florida, June 23-26, 2003.

[5] Nickel, Karl. Tailless Aircraft in Theory and Practice. Washington, DC: American Institute of Aeronautics and Astronautics, 1994.

[6] Gad-el-Hak, M., "Control of Low-Reynolds-number Airfoils: A Review." Lecture Notes in Engineering 54. Low Reynolds Number Aerodynamics: Proceedings of the Conference, 5-7 June 1989. Ed. Thomas J Mueller. Notre Dame, Indiana, USA: Springer-Verlag, 1989. 246-70.

[7] Jenkins D. A., Shyy, W., Sloan J., Klevebring, F., and Nilsson, M., "Airfoil Performance at Low Reynolds Numbers for Micro Air Vehicle Applications," *Thirteenth Bristol International PRV/UAV Conference*, University of Bristol, 1998.

[8] Yarusevych, S., Sullivan, P., and Kawall, K. "Airfoil Boundary Layer and Wake Development at Low Reynolds Numbers." 35th AIAA Fluid Dynamics Conference and Exhibit, Toronto, Ontario, June 6-9, 2005.

[9] Kellogg, and M., Bowman, J. "Parametric Design Study of the Thickness of Airfoils at Reynolds Numbers from 60,000 to 150,000." 42nd AIAA Aerospace Sciences Meeting and Exhibit, Reno, Nevada, Jan. 5-8, 2004.

[10] Gopalarathnam, Ashok, Broughton, Benjamin A., Mcgranahan, Bryan D., and Selig, Michael S. "Design of low Reynolds number airfoils with trips." AIAA Applied Aerodynamics Conference, 19th, Anaheim, CA, June 11-14, 2001.

[11] Lyon, Christopher A., Selig, Michael S., and Broeren, Andy P. "Boundary layer trips on airfoils at low Reynolds numbers." Aerospace Sciences Meeting and Exhibit, 35th, Reno, NV, Jan. 6-9, 1997.

[12] Null, W. and Shkarayev, S. "Effect of Camber on the Aerodynamics of Adaptive Wing Micro Air Vehicles."2nd AIAA Flow Control Conference, Portland, Oregon, June 28-1, 2004.

[13] Drela, M. "XFOIL: An Analysis and Design System for Low Reynolds Number Airfoils." Lecture Notes in Engineering 54. Low Reynolds Number Aerodynamics: Proceedings of the Conference, 5-7 June 1989 . Ed. Thomas J Mueller. Notre Dame, Indiana, USA: Springer-Verlag, 1989. 1-12.

[14] University of Florida, "University of Florida Competition Micro Air Vehicle," 6th International Micro Air Vehicle Competition, Edited by J. Bowman, Brigham Young University, Provo, Utah, Apr. 2002, pp 19-29.

APPENDIX B

Bezier Airfoil Examples:

Airfoil -- BEZ032018510

Airfoil -- BEZ042528010

Airfoil -- BEZ052037510

Airfoil -- BEZ063518510

Airfoil -- BEZ073028510
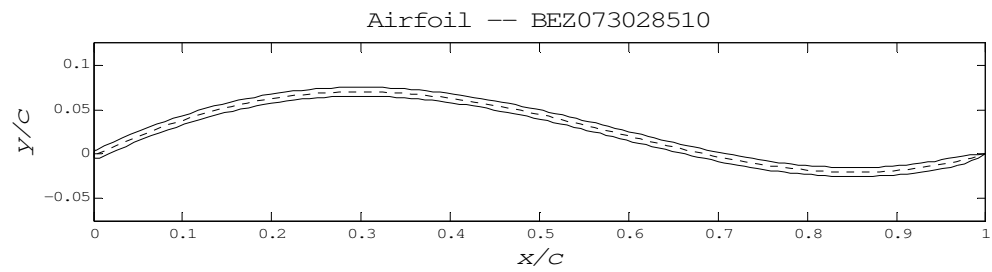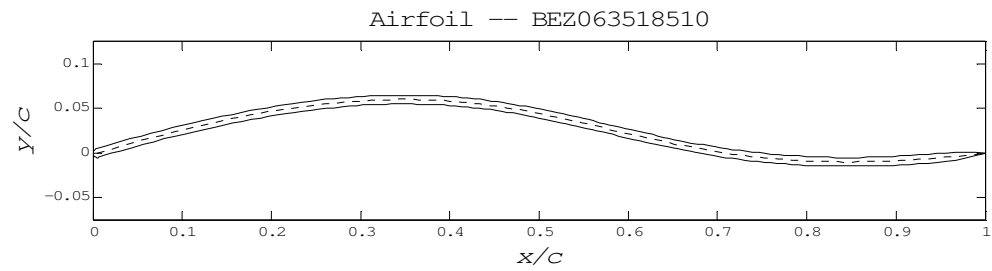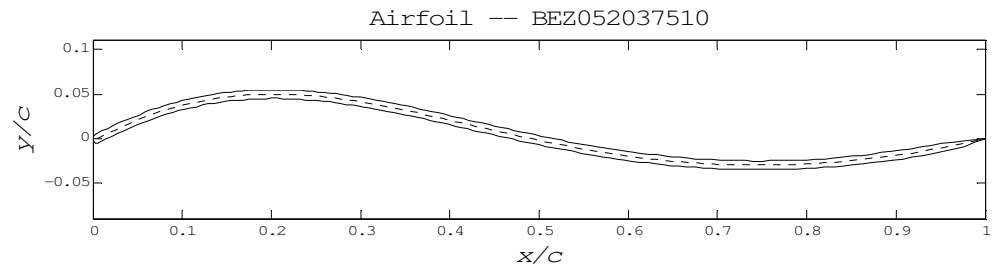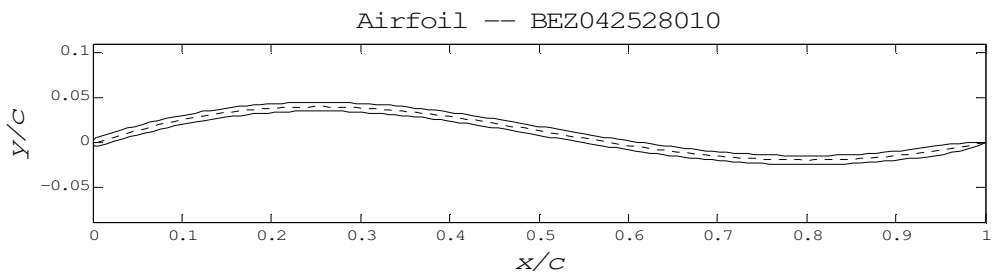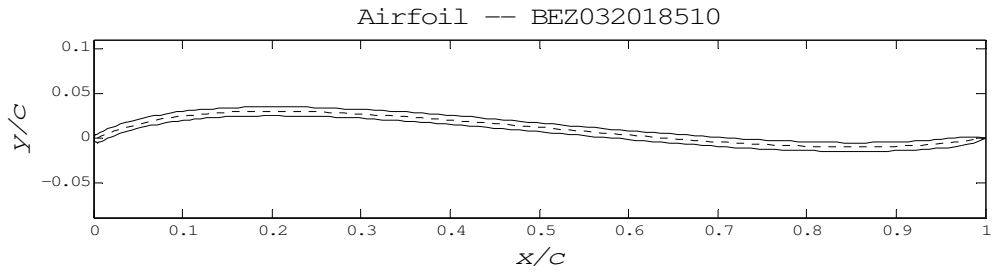
APPENDIX C

C1. EXPECT script for XFOIL Automation

Two major resources were used in developing the following EXPECT code. They are:

Libes, Don. Exploring Expect: A Tcl-Based Toolkit for Automating Interactive Programs. Tim O'Reilly (Editor), O'Reilly & Associates, Ca. 1995.

Raines, Paul, Tranter, Jeff. TCL/TK: In a Nutshell. Andy Oram (Editor), O'Reilly & Associates, Ca. 1999.

Expfoil_V4.tcl

```
###########################################
# Xfoil Expect script Expfoil_V4.tcl  #
# Written by: Michael Reid          #
# On: June 14, 2006               #
# Updated on: July 18, 2006         #
# Validated on : July 19, 2006       #
###########################################

# This script was designed to:
#
# If the option is set:
#   Set the number of panels for every airfoil using the XFOIL default setting
# Run an airfoil through the AOA range initilizing only at failed AOA
# Set N_crit value to be used for all calculations
# Set Vacc, Tgap, blend, iter, and TE_LE for all data collected.
# Improve LE panel density.
# Read in the airfoil names from an outside file to be run
# Save BL, CP, and H data files for specific AOA

# File location:
# cd F:/mike/test\ scripts/
# tclsh Expfoil_V4_lab.tcl

# required for expect
package require Expect

####### Set variables #######

# Folder locations
```

```
set output_folder "Z:/Data/"
set airfoil_folder "Z:/Airfoils/"
set xfoil_dir "E:/xfoil/"

# File names
set airfoil_file Airfoilnames.out

# Airfoil read variables:
set airfoil_read_start 1
set airfoil_read_stop 432
set airfoil_read_size 12
set airfoil_row_size 17

# Analysis Re numbers
set Re {60000 100000 150000}
set Re_name {Re060K Re100K Re150K}

# Analysis AOA range
set AOA_min "0"
set AOA_step ".2"
set AOA_max "12"

# BL, CP, and H record AOA lists
set AOA_BL {0.0 2.0 4.0 6.0 8.0 10.0 12.0 14.0 16.0 18.0}
set AOA_BL_name {00 02 04 06 08 10 12 14 16 18}
set AOA_CP {0.0 2.0 4.0 6.0 8.0 10.0 12.0 14.0 16.0 18.0}
set AOA_CP_name {00 02 04 06 08 10 12 14 16 18}
set AOA_H {0.0 2.0 4.0 6.0 8.0 10.0 12.0 14.0 16.0 18.0}
set AOA_H_name {00 02 04 06 08 10 12 14 16 18}

####### Set XFOIL variables #######

set panel_flag 1
set TE_gap_flag 1
set n 250
set TE_gap 0.001
set blend_dist 0.8
set iter 400
set N_crit 7
set Vacc 0.001
set TE_LE 0.1

####### script variables #######

set timeout 5
set count_airfoil_read $airfoil_read_start
```

####################### Set procedures #########################

```
proc set_current_airfoil {count_airfoil_read} {
 global airfoil_folder airfoil_row_size airfoil_read_size current_airfoil airfoil_file

 set airfoil_ch_id [open "$airfoil_folder$airfoil_file" r]
 set airfoil_loc [expr $airfoil_row_size * ($count_airfoil_read - 1)]
 seek $airfoil_ch_id $airfoil_loc
 set current_airfoil [read $airfoil_ch_id $airfoil_read_size]
 close $airfoil_ch_id
}

proc load_airfoil {current_airfoil} {
 global airfoil_folder

 # load airfoil
 expect "XFOIL   c>" {send "load $airfoil_folder/$current_airfoil.cor\r"}
}

proc panel {n TE_LE} {
 # open panel menu
 expect "XFOIL   c>" {send "ppar\r"}
 # Choose number of panels
 expect "else)   c>" {send "n\r"}
 # Send number of panels
 expect "nodes   i>" {send "$n\r"}
 # Choose TE/LE panel ratio
 expect "else)   c>" {send "t\r"}
 # Send TE/LE panel ratio
 expect "panel density ratio   r>" {send "$TE_LE\r"}
 # No more changes
 expect "else)   c>" {send "\r"}
 # Return to main menu
 expect "else)   c>" {send "\r"}
}

proc set_TE_gap {TE_gap blend_dist} {
 # open geometric design menu
 expect "XFOIL   c>" {send "gdes\r"}
 # Call TE gap sub menu
 expect ".GDES   c>" {send "tgap\r"}
 # Send TE gap value
 expect "Enter new gap   r>" {send "$TE_gap\r"}
 # Send blending distance
 expect "Enter blending distance/c (0..1)   r>" {send "$blend_dist\r"}
```

139

```
  # Return to main menu
  expect ".GDES   c>" {send "\r"}
  # Set buffer airfoil to current airfoil
  expect "XFOIL   c>" {send "pcop\r"}
}

proc iter_set {iter} {
  # call iteration limit prompt
  expect "c>" {send "iter\r"}
  # Send iteration limit
  expect "limit   i>" {send "$iter\r"}
}

proc set_vpar {} {
  global N_crit Vacc

  expect "c>" {send "vpar\r"}
  expect "c>" {send "n\r"}
  expect "r>" {send "$N_crit\r"}
  expect "c>" {send "vacc\r"}
  expect "r>" {send "$Vacc\r"}
  expect "c>" {send "\r"}
}

proc visc_Re {Re count_Re Re_name} {
  global current_Re_name current_Re

  # get Re number for current loop
  set current_Re [lindex $Re $count_Re]
  # get Re number name for current run
  set current_Re_name [lindex $Re_name $count_Re]
  # loop actions:
  # Set viscious solution and Reynolds number
  expect ".OPERi   c>" {send "visc $current_Re\r"}\
      ".OPERv   c>" {send "re $current_Re\r"}
}

proc pacc_on {current_airfoil current_Re_name} {
  global current_output_P_file N_crit output_folder

  # set current output polar file name
  set current_output_P_file "$current_airfoil\_$current_Re_name\_N$N_crit\_X_P.txt"
  # Turn on polar accumulation
  expect "c>" {send "pacc\r"}
  # Send polar save file
  expect "s>" {send "$output_folder$current_output_P_file\r"}
```

140

```
  # Don't set polar dump file
  expect "s>" {send "\r"}
}

proc alfa {current_AOA} {
 global converged_AOA converged_failed failed_reason timeout iter current_airfoil

 set timeout 60
 expect "c>" {send "alfa $current_AOA\r"}
 expect "Point added*c>" {set converged_AOA 1
                 send "cpmn\r"}\
      "VISCAL*c>" {set converged_AOA -1
               set failed_reason "failed AOA: $current_AOA"
               send "init\r"}\
      "STFIND*Continuing" {set converged_failed 1
                  set failed_reason "$current_airfoil\n locked $current_AOA"}\
      "BL array overflow" {set converged_failed 1
                  set failed_reason "$current_airfoil\n BL_array_overflow
$current_AOA"}\
      timeout {set converged_failed 1
            set failed_reason "$current_airfoil\n timeout $current_AOA"}
}

proc set_par {par AOA_par AOA_par_name} {
 global current_AOA AOA_step count_AOA_par converged_AOA current_AOA_par_name

 global current_output_AOA_par_file par_data current_airfoil current_Re_name N_crit

 set count_AOA_par [lsearch $AOA_par [expr $current_AOA - $AOA_step]]
 set par_data -1
 if {$count_AOA_par != -1} {
  set par_data 1
  set current_AOA_par_name [lindex $AOA_par_name $count_AOA_par]
  set current_output_AOA_par_file
"$current_airfoil\_$current_Re_name\_N$N_crit\_$current_AOA_par_name\_X\_$par.txt"
 }
}

proc pacc_off {} {
 # Turn off polar accumulation
 expect "c>" {send "pacc\r"}
 # Remove polar data for this airfoil from RAM
 expect "c>" {send "pdel 0\r"}
}

proc missing_rec {failed_reason missing_file} {
```

```
  global output_folder current_airfoil

  set failed_ch_id [open "$output_folder$missing_file" a]
  puts $failed_ch_id $failed_reason\r
  close $failed_ch_id
}


proc x_reset {} {
  global xfoil_dir airfoil airfoil_folder count_airfoil_read n panel_flag TE_gap blend_dist
TE_gap_flag
  global iter Re count_Re Re_name current_airfoil current_Re_name output_folder TE_LE
Vacc N_crit
  load_airfoil $current_airfoil
  if {$TE_gap_flag == 1} {set_TE_gap $TE_gap $blend_dist}
  if {$panel_flag == 1} {panel $n $TE_LE}
  expect "XFOIL   c>" {send "oper\r"}
  iter_set $iter
  visc_Re $Re $count_Re $Re_name
  set_vpar
  pacc_on $current_airfoil $current_Re_name
}

################# End procedures #################

# Start xfoil
spawn "$xfoil_dir./xfoilP4.exe"

################# Airfoil Loop #################
while {$count_airfoil_read <= $airfoil_read_stop} {

set_current_airfoil $count_airfoil_read

load_airfoil $current_airfoil

if {$TE_gap_flag == 1} {set_TE_gap $TE_gap $blend_dist}

if {$panel_flag == 1} {panel $n $TE_LE}

# Call oper menu
expect "XFOIL   c>" {send "oper\r"}

iter_set $iter

set_vpar
```

```
################## Start of Re number loop ##################
# loop variables:
set count_Re 0

while {$count_Re < [llength $Re]} {

visc_Re $Re $count_Re $Re_name

pacc_on $current_airfoil $current_Re_name

################## Start of AOA loop ##################
# loop variables:
set current_AOA $AOA_min
set converged_AOA -1
set converged_failed -1


while {$current_AOA <= $AOA_max & $converged_failed == -1} {
 while {$converged_AOA == -1 & $converged_failed == -1} {
  #expect "c>" {send "init\r"}
  #expect "assumed*c>" {send "init\r"}\
  #      "will*next*c>" {send "cpmn\r"}
  alfa $current_AOA
  set current_AOA [expr $current_AOA + $AOA_step]
  if {$current_AOA > [expr $AOA_max + $AOA_step]} {
   set converged_failed 1
  }
 }

 if {$converged_AOA == 1} {
  set_par BL $AOA_BL $AOA_BL_name
  if {$par_data == 1} {
   expect "c>" {send "dump $output_folder/BL/$current_output_AOA_par_file\r"}
  }

  set_par H $AOA_H $AOA_H_name
  if {$par_data == 1} {
   expect "c>" {send "vplo\r"}
   expect "c>" {send "h\r"}
   expect "c>" {send "dump $output_folder/H/$current_output_AOA_par_file\r"}
   expect "c>" {send "\r"}
  }

  set_par CP $AOA_CP $AOA_CP_name
  if {$par_data == 1} {
   expect "c>" {send "cpwr $output_folder/CP/$current_output_AOA_par_file\r"}
```

```
    }
  }

  if {$converged_failed == 1} {
    close
    #missing_rec "$current_airfoil\_$current_Re_name\_N$N_crit $failed_reason"
"progress.txt"
    spawn "$xfoil_dir./xfoilP4.exe"
    x_reset
    set converged_failed -1
  }

  set converged_AOA -1
}
################# End of AOA loop #################
set timeout 2
incr count_Re 1

pacc_off

}
################# End of Re number loop #################
incr count_airfoil_read 1

# Return to start up XFOIL   C>
expect "c>" {send "\r"}

}
################# End of airfoil loop #################
```

C2. MATLAB Code: Bezier Airfoil Generation

Load_Airfoil_Variables.m

```
% This script loads variables for Bezier_Airfoil_Generator which calls
% the Bezier function and the Add_thickness script
%
% The number of points on the leading edge is defined in Add_Thickness.m
% The number of points that span the upper and lower surface is defined in
% Bezier.m

outputfolder = 'c:\mike\temp\'; %Fill in folder where airfoil files should be dumped
airfoilnames = 'Airfoilnames.out'; % note that airfoil name file must be in above folder and
be named "Airfoilnames.out"
```

Cv = [0.07];%[0.06 0.07 0.08]; % set of max camber values
XCv = [0.30];%[0.20 0.25 0.30 0.35]; % set of max camber location values
Rv = [0.02];%[0.01 0.02 0.03]; % set of max reflex values
XRv = [0.85];%[0.75 0.80 0.85]; %set of max reflex location values
Tv = [0.01];%[0.01 0.015]; %set of thickness values

global parameters;
global controlpoints;
global checkpoints;
[controlpoints,parameters,checkpoints]=Bezier_Airfoil_Generator(outputfolder,airfoilnames,
Cv,XCv,Rv,XRv,Tv)
max_C_err = max(abs(checkpoints(:,1)-parameters(:,1)))
max_XC_err = max(abs(checkpoints(:,2)-parameters(:,2)))
max_R_err = max(abs(checkpoints(:,3)+parameters(:,3)))
max_XR_err = max(abs(checkpoints(:,4)-parameters(:,4)))

Bezier_Airfoil_Generator.m

function [controlpoints,parameters,checkpoints] = Bezier_Airfoil_Generator
(outputfolder,airfoilnames,Cv,XCv,Rv,XRv,Tv)

% function
[controlpoints,parameters,checkpoints]=Bezier_Airfoil_Generator(outputfolder,airfoilnames,
Cv,XCv,Rv,XRv,Tv)
%
% The function generates the airfoil parameter matrix, bezier control points
% matrix, output airfoil names file, checkpoints matrix for validation, and
% the output airfoil coordinate files.
% The coordinates for each airfoil are saved as its own file from the names
% listed in sequence in the file 'airfoilnames' in the folder 'outputfolder'
%
% Inputs:
% outputfolder = Folder where all files will be dumped
% airfoilnames = File that contains all the airfoil file names
% Cv = Vector of all Max Camber values
% XCv = Vector of all Max Camber location values
% Rv = Vector of all Max Reflex values
% XRv = Vector of all Max Reflex location values
% Tv = Vector of all Thickness values
%
% Outputs:
% controlpoints = Array of all Bezier control points for the corresponding control points
% parameters = Array of all combinations of airfoil parameters

```matlab
[Cvn,Cvm] = size(Cv);
[XCvn,XCvm] = size(XCv);
[Rvn,Rvm] = size(Rv);
[XRvn,XRvm] = size(XRv);
[Tvn,Tvm] = size(Tv);

% Constants outside of loops
n = 0; % acts as counter, n represents the number of the airfoil in the sequence
nn = 0; % acts as counter, nn represents the number of the airfoil in the sequence for the first
loop group

% This section creates the file Airfoilnames.out which contains a list of
% all the airfoil names in the format of the airfoil naming convention
% BEZCvXCvRvXRvTv


% this section generates the matrix that contains all possible parameter combinations
for i = 1:Cvm
    for j = 1:XCvm
        for k = 1:Rvm
            for l = 1:XRvm
                for m = 1:Tvm
                    nn = nn+1; % indicates what airfoil is being calculated!
                    global parameters;
                    parameters(nn,:) = [Cv(i),XCv(j),Rv(k),XRv(l),Tv(m)];
                end
            end
        end
    end
end

% Creates the airfoilnames file
fid = fopen([outputfolder airfoilnames],'a');
var = [parameters(:,1:4)*100 parameters(:,5)*1000]';
fprintf(fid,'BEZ%02.0f%01.0f%01.0f%01.0f%02.0f.cor\n',var); % Set the file extension here
(.cor)
fclose(fid);

for i = 1:Cvm
    for j = 1:XCvm
        for k = 1:Rvm
            for l = 1:XRvm
                for m = 1:Tvm
                    n = n+1; % indicates what airfoil is being calculated!
                    n_prime = nn - n;
```

146

```matlab
                [x1,y1,x2,y2,x,y]=Bezier(Cv(i),XCv(j),Rv(k),XRv(l),Tv(m)); % call bezier
function to generate x1,y1,x2,y2 control points

                global checkpoints
                [C_chk,Cx_chk_num] = max(y);
                [R_chk,Rx_chk_num] = min(y);
                checkpoints(n,:) = [C_chk,x(Cx_chk_num),R_chk,x(Rx_chk_num)];

                global controlpoints;
                controlpoints(n,:) = [x1 y1 x2 y2]; % matrix contains all x1 y1 x2 y2 values
corresponding to the C XC R XR values in

                run Add_Thickness

                % generate a file of the airfoil coordinates
                fid = fopen([outputfolder 'Airfoilnames.out'],'r');
                position = -(16*(n_prime+1)+(n_prime+1));
                fseek(fid, position, 'eof');
                s = fread(fid,16,'16*uchar=>uchar');
                f = char(s');
                fclose(fid);

                % Generates the actual airfoil coordinate file
                fid = fopen([outputfolder f],'w');
                var = [parameters(n,1:4)*100 parameters(n,5)*1000]';
                fprintf(fid,'BEZ%02.0f%01.0f%01.0f%01.0f%02.0f\n',var);
                fprintf(fid,'%-1.6f   % 1.6f\n',airfoilpoints');
                fclose(fid);
            end
        end
    end
  end
end
```

Bezier.m

```matlab
function [x1,y1,x2,y2,x,y]=Bezier(C,XC,R,XR,T)

% [x1,y1,x2,y2,x,y]=Bezier(C,XC,R,XR,T)
%
% Bezier finds the control points x1,y1,x2,y2 so that the resulting curve
% passes through the input points (XC,C) and (XR,-R) and has end points at
% (T/2,0) and (1-T/2,0). Note that the end points are adjusted for the
% thickness of the airfoil so that the chord of the airfoil is still
```

% normalized to 1.
%
% Inputs:
% C = Max Camber value
% XC = Max Camber x location
% R = Max Reflex
% XR = Max Reflex x position
% T = Airfoil thickness
%
% Outputs:
% x1 = x location of the control point for LE
% y1 = y location of the control point for LE
% x2 = x location of the control point for TE
% y2 = y location of the control point for TE
% x = airfoil x coordinates
% y = airfoil y coordinates

% Set constants
x0=0+T/2; % End point adjusted for LE circle
y0=0; % End point
x3=1; % End point
y3=0; % End point

x1 = XC; % First guess to be addressed in x1 loop
y1 = C; % First guess to be addressed in y1 loop
x2 = XR; % First guess to be addressed in x2 loop
y2 = -R; % First guess to be addressed in y2 loop

accuracy = .000001; % set the accuracy to which the curve will converge to the actual values
space = 1/125; % sets the spacing of points, defines the number of points on each surface
(upper and lower)

%c = 2.3;
%b = 0;

%for j = 0:space:1
%   b = b + 1;
%   t(b) = 1/exp(c) * exp(c*j) - 1/exp(c) * (-j + 1); % this set the exponential point
distribution
%end

t = 0:space:1;

% this loop finds the y coordinates of the control points y1 and y2
h=0; % initialize h
for h = 1:10 % iterative loop to account for change in both parameters

```
test = 0; % acts as a catch for while loop
k = 0; % acts as a catch for infinite loop

% loop to find y1 that yields max camber input value
while test == 0
   k = k+1;

   % Calculate Bezier coefficients
   cx = 3*(x1-x0);
   bx = 3*(x2-x1)-cx;
   ax = x3-x0-cx-bx;
   cy = 3*(y1-y0);
   by = 3*(y2-y1)-cy;
   ay = y3-y0-cy-by;

   n=0;
   for m = 1:length(t);
      n=n+1;
      x(n) = ax*t(m)^3+bx*t(m)^2+cx*t(m)+x0;
      y(n) = ay*t(m)^3+by*t(m)^2+cy*t(m)+y0;
   end

   % Adjust guess by 1/2 of the difference of the current max camber
   % value and the desired location
   if abs(max(y)-C) < accuracy;
      test = 1;
   elseif max(y) > C;
      y1 = y1-(max(y)-C)/2;
   elseif max(y) < C;
      y1 = y1+(C-max(y))/2;
   end

   if k > 1000
      test = 1;
      disp('Infinant loop in y1!!!')
   end
end

test = 0; % acts as a catch for while loop
k = 0; % acts as a catch for infinite loop

% Loop to find y2 that yields max reflex input value
while test == 0
   k = k+1;
```

```
% Calculate Bezier coefficients
cx = 3*(x1-x0);
bx = 3*(x2-x1)-cx;
ax = x3-x0-cx-bx;
cy = 3*(y1-y0);
by = 3*(y2-y1)-cy;
ay = y3-y0-cy-by;

n=0;
for m = 1:length(t);
    n=n+1;
    x(n) = ax*t(m)^3+bx*t(m)^2+cx*t(m)+x0;
    y(n) = ay*t(m)^3+by*t(m)^2+cy*t(m)+y0;
end

% Adjust guess by 1/2 of the difference of the current max reflex
% value and the desired location
if abs(R+min(y)) < accuracy;
    test = 1;
elseif min(y) > -R;
    y2 = y2-(min(y)+R)/2;
elseif min(y) < -R;
    y2 = y2+(-R-min(y))/2;
end

if k > 1000
    test = 1;
    disp('Infinite loop in y2!!!')
end
end
end


% This loop find the x coordinates of the control points
h=0; % initialize h
for h = 1:10;

test = 0; % acts as a catch for while loop
k = 0; % acts as a catch for infinite loop
j=0;

% loop to find x1 that yields max camber location input value
while test == 0
    k = k+1;

    % Calculate Bezier coefficients
```

```matlab
    cx = 3*(x1-x0);
    bx = 3*(x2-x1)-cx;
    ax = x3-x0-cx-bx;
    cy = 3*(y1-y0);
    by = 3*(y2-y1)-cy;
    ay = y3-y0-cy-by;

    n=0;
    for m = 1:length(t);
       n=n+1;
       x(n) = ax*t(m)^3+bx*t(m)^2+cx*t(m)+x0;
       y(n) = ay*t(m)^3+by*t(m)^2+cy*t(m)+y0;
    end

    [val,j]=max(y); % Find which element in y is max and take corresponding x value

    % Adjust guess by 1/2 of the difference of the current max camber
    % location and the desired location
    if abs(x(j)-XC) < accuracy;
       test = 1;
    elseif x(j) > XC;
       x1 = x1-(x(j)-XC)/2;
    elseif x(j) < XC;
       x1 = x1+(XC-x(j))/2;
    end

    if k > 1000
       test = 1;
       disp('Infinant loop in x1!!!')
    end
end

test = 0; % acts as a catch for while loop
k = 0; % acts as a catch for infinite loop
i=0;
% Loop to find x2 that yields max reflex location input value
while test == 0
   k = k+1;

   % Calculate Bezier coefficients
   cx = 3*(x1-x0);
   bx = 3*(x2-x1)-cx;
   ax = x3-x0-cx-bx;
   cy = 3*(y1-y0);
   by = 3*(y2-y1)-cy;
   ay = y3-y0-cy-by;
```

```matlab
    n=0;
    for m = 1:length(t);
        n=n+1;
        x(n) = ax*t(m)^3+bx*t(m)^2+cx*t(m)+x0;
        y(n) = ay*t(m)^3+by*t(m)^2+cy*t(m)+y0;
    end

    [val,i]=min(y); % Find which element in y is min and take corresponding x value

    % Adjust guess by 1/2 of the difference of the current max reflex
    % location and the desired location
    if abs(x(i)-XR) < accuracy;
        test = 1;
    elseif x(i) > XR;
        x2 = x2-(x(i)-XR)/2;
    elseif x(i) < XR;
        x2 = x2+(XR-x(i))/2;
    end

    if k > 1000
        test = 1;
        disp('Infinite loop in x2!!!');
    end
end
end
```

Add_Thickness.m

```matlab
% Add thickness script
% at this point the airfoil MCL in defined by (x(t),y(t)) where t is a
% parametric variable.  The density of points increases with curvature, at
% points like the max camber and max reflex points the density of points
% increases. This script also formats the upper and lower surfaces into the
% standard format required by XFLR5.


%maxLEangle = 180 / round(pi * Tv(m) / (2 * (x(2)-x(1)))); % (DEG) maximum
%angle between pannels on leading edge set so that panel size matches upper
%and lower surface
maxLEangle = 12; % (DEG) maximum angle between pannels on leading edge

% Clear all built variables to eliminate double up
clear xletop yletop xlebot ylebot dx dy dydx ty tx xsurtopr ysurtopr
```

```matlab
% This just checks to see if the x and y vectors are the same size
[s,sizey] = size(y);
[s,sizex] = size(x);
if sizey ~= sizex
    disp('ERROR x and y vectors are not the same size!!!');
end

for d = 1:1:sizey; % take the center derative of the y. If end points; use forward or backward
approximation
    if d==sizey
        dy(d)=(y(d)-y(d-1)); % Backwards differentiate zmcl
        dx(d)=(x(d)-x(d-1)); % Backwards differentiate zmcl
    elseif d==1
        dy(d)=(y(d+1)-y(d)); %  Forward differentiate zmcl
        dx(d)=(x(d+1)-x(d)); %  Forward differentiate zmcl
    else
        dy(d)=(y(d+1)-y(d-1)); % Middle differentiate zmcl
        dx(d)=(x(d+1)-x(d-1)); % Middle differentiate zmcl
    end
    dydx(d) = dy(d)/dx(d); % divide dy by dx to get derivative (slope) value dy/dx
end

nptot = round(180/maxLEangle);
np1 = round((((pi/2) - atan(dydx(1))) / (pi)) * nptot); % number of points to define top
portion of the LE circle
np2 = round((((pi/2) + atan(dydx(1))) / (pi)) * nptot); % number of points to define bottom
portion of the LE circle

% this section generates the thickness distribution for the airfoil
% assuming a rounded leading edge and a parabolic trailing edge
T = Tv(m); % This is the thickness of the current airfoil
xTte  = [1:5]; % Defines number of points that are effected at the TE (Note the equation that
appears in next line must be changes if 5 is not used)
Tte = [-T/50*xTte.^2+T/2]; % define thickness distribution over last 5 y points
Tdv = [T/2*ones(1,sizey-5) Tte]; % sets the thickness distribution vector, constant thickness
until the last 5 y values

% this section adjusts the coordinates for thickness distribution
for p = 1:1:sizey
    ty(p) = Tdv(p)*cos(atan(dydx(p))); % adjust y coordinate for slope of MCL
    tx(p) = Tdv(p)*sin(atan(dydx(p))); % adjuste x coordinate for slope of MCL
end

ysurtop = y + ty;
ysurbot = y - ty;
xsurtop = x - tx;
```

```
xsurbot = x + tx;

% Creating the leading edge
theta0le = atan(dydx(1));
thetaletop = (theta0le+pi/2):(pi/2-theta0le)/np1:pi; % counter-cloclwise around the leading
edge to form top
thetalebot = pi:(theta0le+pi/2)/np2:(theta0le+3*pi/2); % counter-clockwise around the
leading edge to form bottom

% top surface of LE (+y)
at=0;
for kt = 2:1:np1+1 % adjusted so that point where circle and upper surface meet is not
defined 2 times but LE point is defined by both the upper and lower surfaces
    at = at+1;
    xletop(at) = T/2+T/2*cos(thetaletop(kt)); % adjusted for LE raidus so that min(x)=0 not a
(-) number
    yletop(at) = T/2*sin(thetaletop(kt));
end
% botom surface of LE (-y)
ab=0;
for kb = 1:1:np2 % adjusted so that point where circle and upper surface meet is not defined
2 times but LE point is defined by both the upper and lower surfaces
    ab = ab+1;
    xlebot(ab) = T/2+T/2*cos(thetalebot(kb)); % adjusted for LE raidus so that min(x)=0 not a
(-) number
    ylebot(ab) = T/2*sin(thetalebot(kb));
end


b=0;
for v = sizey:-1:1; % re-organize xb and zb so that x goes down up not up
    b=b+1;
    xsurtopr(b)=xsurtop(v);
    ysurtopr(b)=ysurtop(v);
end

xout = [xlebot xsurbot]';
yout = [ylebot ysurbot]';
out = [xout yout];
xback = [xsurtopr xletop]';
yback = [ysurtopr yletop]';
back = [xback yback];
airfoilpoints = [back ; out];
```

C3. Data Analysis

Load_variables.m

```
% This script loads the variables for SavePolarData_X
% It is assumed that it will be used only for Bezier Airfoils that follow
% the standard naming convention

% This section matches the section in the Expect script
directory = 'C:\Mike\Thesis\Thin Airfoil Work\Collected Data\Data 12\';
airfoil_dir = 'C:\Mike\Thesis\Thin Airfoil Work\Collected Data\Airfoils\';
airfoil_file = 'Airfoilnames.out';
airfoil_read_start = [1];
airfoil_read_stop = [432];
airfoil_read_size = [12]; % 12 for Bezier Airfoils
airfoil_row_size = [17]; % 17 for Bezier Airfoils, 18 if*
reynolds_nums = ['060';'100';'150'];
reynolds_nums_values = [60 100 150];
AOA_min = [0];
AOA_step = [0.2];
AOA_max = [12];
AOA_BL_range = ['00';'01';'02';'03';'04';'05';'06';'07';'08';'09';'10';'11';'12';'13';'14'];
AOA_CP_range = ['00';'01';'02';'03';'04';'05';'06';'07';'08';'09';'10';'11';'12';'13';'14'];
AOA_H_range = ['00';'01';'02';'03';'04';'05';'06';'07';'08';'09';'10';'11';'12';'13';'14'];
Ncrit = ['7'];

%%%%%%%%%%%%%%%%%%%%%%%%%%%%%%%%%%%%%%%%%%%
% This section pulls the information from Airfoilnames.out to use in
% opening data files
i = 0;
[fid] = fopen([airfoil_dir airfoil_file],'r');
for count_airfoil_read = airfoil_read_start:airfoil_read_stop
    i = i+1;
    fseek(fid,[airfoil_row_size * (count_airfoil_read - 1)],'bof');
    airfoilnames(i,:) = char(fread(fid,12,'12*uchar=>uchar'));
    airfoilnumbers(i,:) = count_airfoil_read;
end
fclose(fid);

% this section collects the camber, Xcamber, reflex, Xreflex, and Thickness values
% from the airfoilnames.out file and saves them to the data_parameters matrix
i = 0;
[fid] = fopen([airfoil_dir airfoil_file],'r');
for count_airfoil_read = airfoil_read_start:airfoil_read_stop
    i = i+1;
```

```
    fseek(fid,[airfoil_row_size * (count_airfoil_read - 1) + 3],'bof');
    saved_par_char(i,:) = (fread(fid,9,'int8=>int8'));
    data_parameters(i,1) = char_convert(saved_par_char(i,1:2)); % Camber
    data_parameters(i,2) = char_convert(saved_par_char(i,3:4)); % Xcamber
    data_parameters(i,3) = char_convert(saved_par_char(i,5)); % Reflex
    data_parameters(i,4) = char_convert(saved_par_char(i,6:7)); % Xreflex
    data_parameters(i,5) = char_convert(saved_par_char(i,8:9)); % Thickness
end
fclose(fid);
%%%%%%%%%%%%%%%%%%%%%%%%%%%%%%%%%%%%%%%%

[Name_Polar_Data,Missing_Polar_Files,
Missing_Polar_Files_num,data_eval]=SavePolarData_x_v3(directory, airfoilnames,
airfoilnumbers, data_parameters, reynolds_nums, reynolds_nums_values, Ncrit)
[P_data_matrix]=RetrevePolarData_X(directory, airfoilnames, airfoilnumbers,
data_parameters, AOA_min, AOA_step, AOA_max, reynolds_nums, reynolds_nums_values,
Ncrit, data_eval)

[Name_BL_Data, Missing_BL_Files, Missing_BL_Files_num]=SaveBLData_X(directory,
airfoilnames, airfoilnumbers, AOA_BL_range, reynolds_nums, Ncrit)
[BL_data_matrix]=RetreveBLData_X(directory, airfoilnames, airfoilnumbers,
data_parameters, AOA_BL_range, reynolds_nums, reynolds_nums_values, Ncrit,
Missing_BL_Files)

[Name_CP_Data, Missing_CP_Files]=SaveCPData_X(directory,
airfoilnames,airfoilnumbers, AOA_CP_range, reynolds_nums, Ncrit)
[Name_H_Data, Missing_H_Files]=SaveHData_X(directory, airfoilnames, airfoilnumbers,
AOA_H_range, reynolds_nums, Ncrit)
```

SavePolarData_X_v3.m

```
function [Name_Polar_Data,Missing_Polar_Files, Missing_Polar_Files_num,
data_eval]=SavePolarData_X(directory, airfoilnames, airfoilnumbers, data_parameters,
reynolds_nums, reynolds_nums_values, Ncrit)


% [Name_Polar_Data,Missing_Polar_Files,
% Missing_Polar_Files_num]=SavePolarData_X(directory, airfoilnames, airfoilnumbers,
% data_parameters, reynolds_nums, reynolds_nums_values, Ncrit)
%
% This function takes the imput matricies airfoilnames,,
% reynolds_nums, and Ncrit to form filenames that correspond to
% polar files in the given directory.  The data is then
% evaluated for quality and a quality file is created
%
```

% Note that all polar files should follow the standard naming format:
% i.e. BEZ032518510_Re060K_N7_X_P.txt or airfoilname_ReZZZK_NY_X_P.txt
% Reynolds number must be displayed as 3 digits
% The N7 shows the Ncrit value used
% The X means the data was collected with XFOIL
% the P means it is a polar file
% Data files generated will have a D after the X to read XD to note that it
% is a data file.
%
% Inputs:
% directory = location of the polar data files
% airfoilnames = A column vector that contains all the airfoil names that have polars
% reynolds_num = A column vector that contains all the reynolds numbers tested
% Ncrit = N value for run
%
% Outputs:
% Name_Polar_Data = contains names of the polar files, each row has the name of
%   corresponding column's data in the other variables.
% Missing_Polar_Files = List of missing Polar files

% Constants
i = 0; % counter
position = 0; % current location in the file
hit = 0; % flag for successful find
count = 0; %counter for where the data is going in
mfcount = 0; %counter for missed files
no_data_count = 0; %counter for empty data files

fclose('all');

[j,z] = size(airfoilnames);
[k,z] = size(reynolds_nums);

for airfoilnum = 1:j
    for ren_num = 1:k

        count = count+1;
        filename = [airfoilnames(airfoilnum,:) '_Re' reynolds_nums(ren_num,:) 'K_N' Ncrit
'_X_P.txt'];
        [fid] = fopen([directory filename],'r');

        if fid == -1
            mfcount = mfcount+1;
            Missing_Polar_Files(mfcount,:) = [airfoilnames(airfoilnum,:) '_Re'
reynolds_nums(ren_num,:) 'K_X_P.txt'];
            Missing_Polar_Files_num(mfcount,:) = [airfoilnumbers(airfoilnum,:)];
```

157

```
        data_eval(count,:) = [data_parameters(airfoilnum,:) reynolds_nums_values(ren_num)
0 0 0 0 0 0 0];
    end

    if fid ~= -1 % All of the following code will be skipped if the file does not open
properly and there will be a column of 0's it it's place.


%%%%%%%%%%%%%%%%%%%%%%%%%%%%%%%%%%%%%
        % Search for airfoil name from Polar file %

%%%%%%%%%%%%%%%%%%%%%%%%%%%%%%%%%%%%%

        position = 1;
        i = 0;
        hit = 0;
        while hit < 1
            position = position+1;
            fseek(fid, position, 'bof');
            chnameseek(1) = fread(fid,1,'1*uchar=>uchar');
            fseek(fid, position+1, 'bof');
            chnameseek(2) = fread(fid,1,'1*uchar=>uchar');
            fseek(fid, position+2, 'bof');
            chnameseek(3) = fread(fid,1,'1*uchar=>uchar');
            if chnameseek == [114 58 32] % find the position in the file that corresponds to the
sequence 'r: '
                hit = 1;
            end
        end

        %%%%%%%%%%%%%%%%%%%%%%%%%%%%%%%%%%
        % Get airfoil name from Polar file %
        %%%%%%%%%%%%%%%%%%%%%%%%%%%%%%%%%%

        i = 0;
        hit = 0;
        position = position+2; % adjust the position found above to correspond to the start of
the airfoil name
        while hit < 1
            i = i+1;
            fseek(fid, position+i, 'bof');
            chaf(i,:) = fread(fid,1,'1*uchar=>uchar');
            if chaf(i,:) == [32]; % copy letters for the airfoil name until there is 3 spaces in a
row
                hit = 1;
            end
```

```
        if chaf(i,:)~= [32];
            airfoilname(i) = char(chaf(i,1)');
        end
    end


%%%%%%%%%%%%%%%%%%%%%%%%%%%%%%%%%%%%%%%%
      % Search for Reynolds number from Polar file %

%%%%%%%%%%%%%%%%%%%%%%%%%%%%%%%%%%%%%%%%%%
      position = 1;
      i = 0;
      hit = 0;
      while hit < 1
        position = position+1;
        fseek(fid, position, 'bof');
        chreseek(1) = fread(fid,1,'1*uchar=>uchar');
        fseek(fid, position+1, 'bof');
        chreseek(2) = fread(fid,1,'1*uchar=>uchar');
        fseek(fid, position+2, 'bof');
        chreseek(3) = fread(fid,1,'1*uchar=>uchar');
        if chreseek == [82 101 32] % find the position in the file that corresponds to the
sequence 'Re '
            hit = 1;
        end
      end

        %%%%%%%%%%%%%%%%%%%%%%%%%%%%%%%%%%%%%%%
        % Get Reynolds number from Polar file %
        %%%%%%%%%%%%%%%%%%%%%%%%%%%%%%%%%%%%%%%

      position = position+11; % adjust the position found above to correspond to the start
of the Reynolds number
      i = 0;
      hit = 0;
      while hit < 1
        fseek(fid, position+i, 'bof');
        i = i+1;
        chre(i) = fread(fid,1,'1*uchar=>uchar');
        if chre(i) == 32;
            hit = 1;
        end
        if chre(i) ~= 32;
            renumber(i) = char(chre(i));
        end
      end
```

```
        renumberout = ['_Re' renumber 'K'];


%%%%%%%%%%%%%%%%%%%%%%%%%%%%%%%%%%%%%%
        % Search for Ncrit number from Polar file %

%%%%%%%%%%%%%%%%%%%%%%%%%%%%%%%%%%%%%%%%%
        position = 1;
        i = 0;
        hit = 0;
        while hit < 1
           position = position+1;
           fseek(fid, position, 'bof');
           chNseek(1) = fread(fid,1,'1*uchar=>uchar');
           fseek(fid, position+1, 'bof');
           chNseek(2) = fread(fid,1,'1*uchar=>uchar');
           fseek(fid, position+2, 'bof');
           chNseek(3) = fread(fid,1,'1*uchar=>uchar');
           if chNseek == [78 99 114] % find the position in the file that corresponds to the
sequence 'Re '
               hit = 1;
           end
        end


        %%%%%%%%%%%%%%%%%%%%%%%%%%%%%%%%%%%%
        % Get Reynolds number from Polar file %
        %%%%%%%%%%%%%%%%%%%%%%%%%%%%%%%%%%%%%

        position = position+10; % adjust the position found above to correspond to the start
of the Reynolds number
        i = 0;
        hit = 0;
        while hit < 1
           fseek(fid, position+i, 'bof');
           i = i+1;
           chN(i) = fread(fid,1,'1*uchar=>uchar');
           if chN(i) == 46;
              hit = 1;
           end
           if chN(i) ~= 46;
              Nnumber(i) = char(chN(i));
           end
        end
        Ncritout = ['_N' Nnumber];
```

%%%%%%%%%%%%%%%%%%%%%%%%%%%%%%%%%%%%%%
        % Get Polar data to output to data file from Polar file %

%%%%%%%%%%%%%%%%%%%%%%%%%%%%%%%%%%%%%%

        position = 1;
        i = 0;hit = 0;
        while hit < 1
            position = position+1;
            fseek(fid, position, 'bof');
            datastart(1) = fread(fid,1,'1*uchar=>uchar');
            fseek(fid, position+1, 'bof');
            datastart(2) = fread(fid,1,'1*uchar=>uchar');
            fseek(fid, position+2, 'bof');
            datastart(3) = fread(fid,1,'1*uchar=>uchar');
            if datastart == [45 45 13] % Search for the start of the data which comes after the
last '--(new line)'
                hit = 1;
            end
        end

        % This gets all the data from the file
        fseek(fid, position+4, 'bof');
        polardata = char(fread(fid, 50000, 'uchar')');
        fclose(fid);

        % This section creates the easy to read txt file
        filename = [directory 'Data Files\' airfoilname renumberout Ncritout '_XD_P.txt']; %
Creates the file name from the airfoil name and the reynolds number.
        fid = fopen(filename,'w');
        fwrite(fid, polardata, 'uchar');
        fclose(fid);

%%%%%%%%%%%%%%%%%%%%%%%%%%%%%%%%%%%%%%

        % This section analyzes the data and creates data_eval and
        % finds the stall point, stall behavior, Cl_max, Cl_Cd_max

        [data]=load(filename);% Get polar data from file
        AOA = data(:,1);
        Cl = data(:,2);
        Cd = data(:,3);
        Cl_Cd = Cl./Cd;
        [max_AOA_gap,AOA_n] = max(diff(AOA));

```
stall_catch = 0;
i = 0;

m = find(diff(sign(diff(Cl)))<0)+1;

if length(find(sign(diff(Cl))>0))==(length(diff(Cl)))
    m = 1;
end

%plot(AOA,Cl,'.',AOA(m),Cl(m),'x')

while stall_catch == 0
    i = i+1;

    low_range = min(m(i) - round(0.5*m(i)))+1;
    high_range = max(m(i) + round(0.5*(length(AOA)-m(i))));


%plot(AOA(low_range:high_range),Cl(low_range:high_range),'.',AOA(m(i)),Cl(m(i)),'x')

        if max(Cl(low_range:high_range)) == Cl(m(i))
            stall_catch = 1;
            max_Cl = Cl(m(i));
            max_Cl_AOA = AOA(m(i));
            max_Cl_AOA_error = AOA(m(i)+1)-AOA(m(i)-1);

            [Cl_Cd_max,q] = max(Cl./Cd);
            Cl_Cd_max_AOA = AOA(q);
            Cl_CD_AOA_error = AOA(q+1)-AOA(q-1);

        elseif i == length(m)
            stall_catch = 1; %no stall point!!!

            max_Cl = 0;
            max_Cl_AOA = 0;
            max_Cl_AOA_error = 0;

            Cl_Cd_max = 0;
            Cl_Cd_max_AOA = 0;
            Cl_CD_AOA_error = 0;

        end
end
```

```matlab
    if max_AOA_gap > 2 & AOA(AOA_n-1) < max_Cl_AOA

        max_Cl = 0;
        max_Cl_AOA = 0;
        max_Cl_AOA_error = 0;

        Cl_Cd_max = 0;
        Cl_Cd_max_AOA = 0;
        Cl_CD_AOA_error = 0;
    end


        %figure(1)
        %plot(AOA,Cl,'.',max_Cl_AOA,max_Cl,'x')
        %figure(2)
        %plot(Cd,Cl,'.',Cd(nn(i)),Cl(nn(i)),'x')
        data_eval(count,:) = [data_parameters(airfoilnum,:) reynolds_nums_values(ren_num)
1 max_Cl_AOA max_Cl max_Cl_AOA_error Cl_Cd_max_AOA Cl_Cd_max
Cl_CD_AOA_error];

        % Creates a check variable to compair with to be sure correct data was collected
        Name_Polar_Data(count,:) = [airfoilname renumberout Ncritout '_XD_P.txt'];
    end
  end
end

if mfcount == 0
   Missing_Polar_Files = ['No missing files!'];
   Missing_Polar_Files_num = [0];
end

% Generate list of airfoils to rerun in xfoil
% camber_values = [3 4 5 6 7 8];
% camber_char = ['03';'04';'05';'06';'07';'08'];
% for i = 1:length(camber_values)
%    var = data_eval(find(data_eval(:,7)==0 & data_eval(:,1)==camber_values(i) &
data_eval(:,6)==60),1:5)';
%    fid = fopen(['C:\Mike\temp\Missing Airfoils\' 'Missing_Airfoils_C' camber_char(i,:)
'K.out'],'w');
%    fprintf(fid,'BEZ%02.0f%01.0f%01.0f%01.0f%02.0f.cor\n',var); % Set the file extension
here (.cor)
%    fclose(fid);
% end

%Generate list of airfoils to rerun in xfoil
% for i = 1:length(reynolds_nums_values)
```

```
%     var = data_eval(find(data_eval(:,8)==0 &
data_eval(:,6)==reynolds_nums_values(i)),1:5)';
%     fid = fopen(['C:\Mike\temp\Missing Airfoils\' 'Mising_Airfoils_Re' reynolds_nums(i,:)
'K.out'],'w');
%     fprintf(fid,'BEZ%02.0f%01.0f%01.0f%01.0f%02.0f.cor\n',var); % Set the file extension
here (.cor)
%     fclose(fid);
% end
```

APPENDIX D

D1. Surface Oil Flow Visualization Results

BEZ032037516

BEZ032037516 Re = 99,500 +/- 24,800
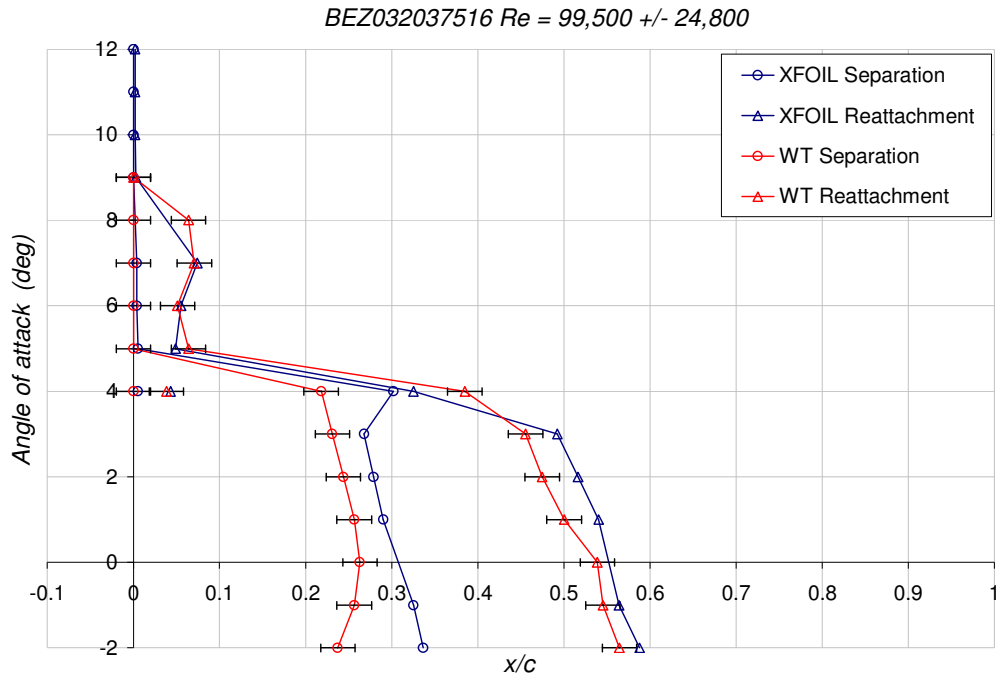
BEZ032037516 Re = 151,000 +/- 25,400

166
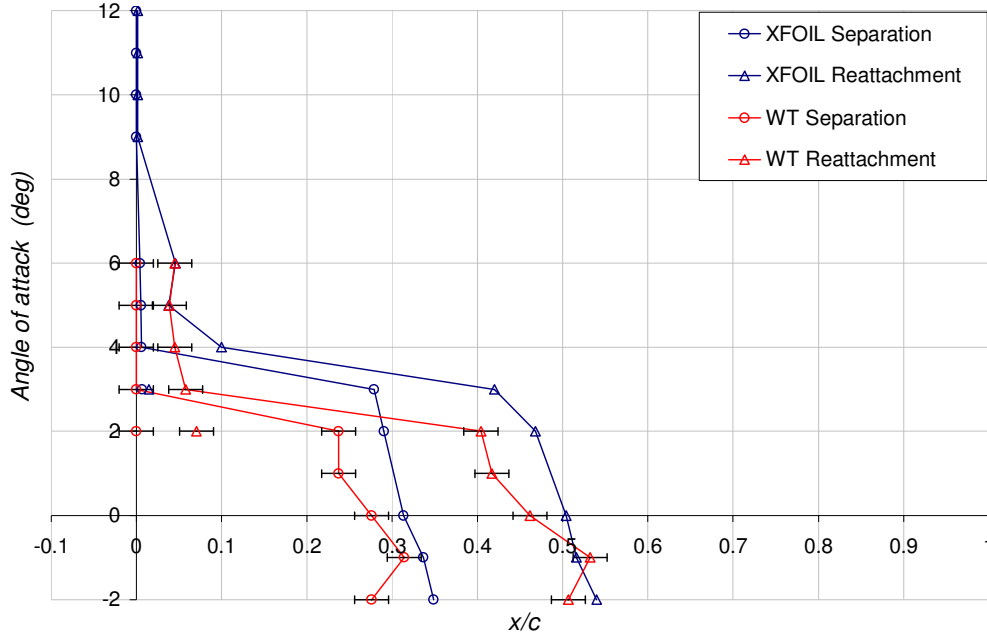
BEZ053018513

BEZ053018513 Re = 98,100 +/- 26,700
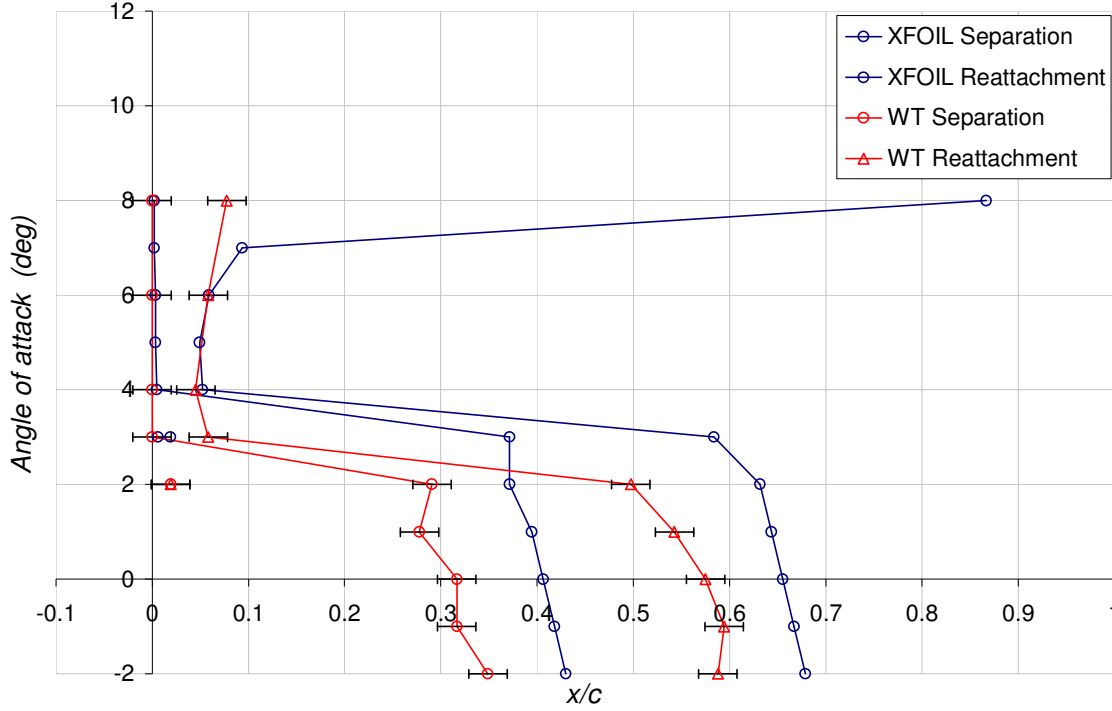
BEZ053018513 Re = 150,000 +/- 27,900
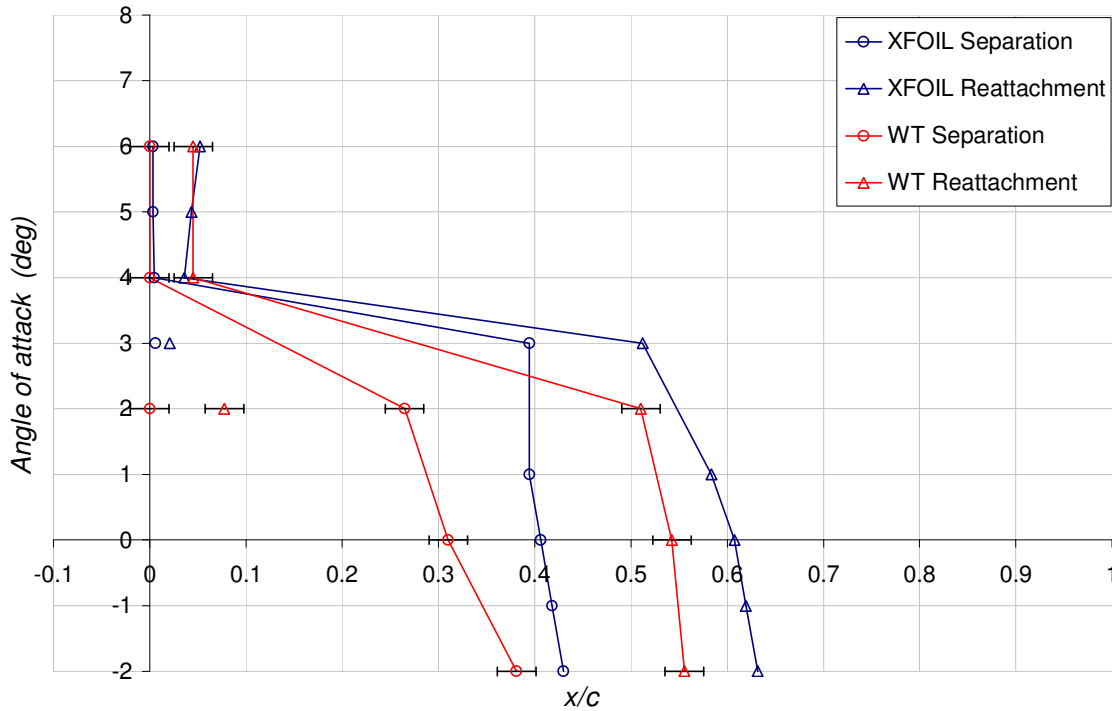
BEZ062518513

BEZ062518513 Re = 98,600 +/- 24,300
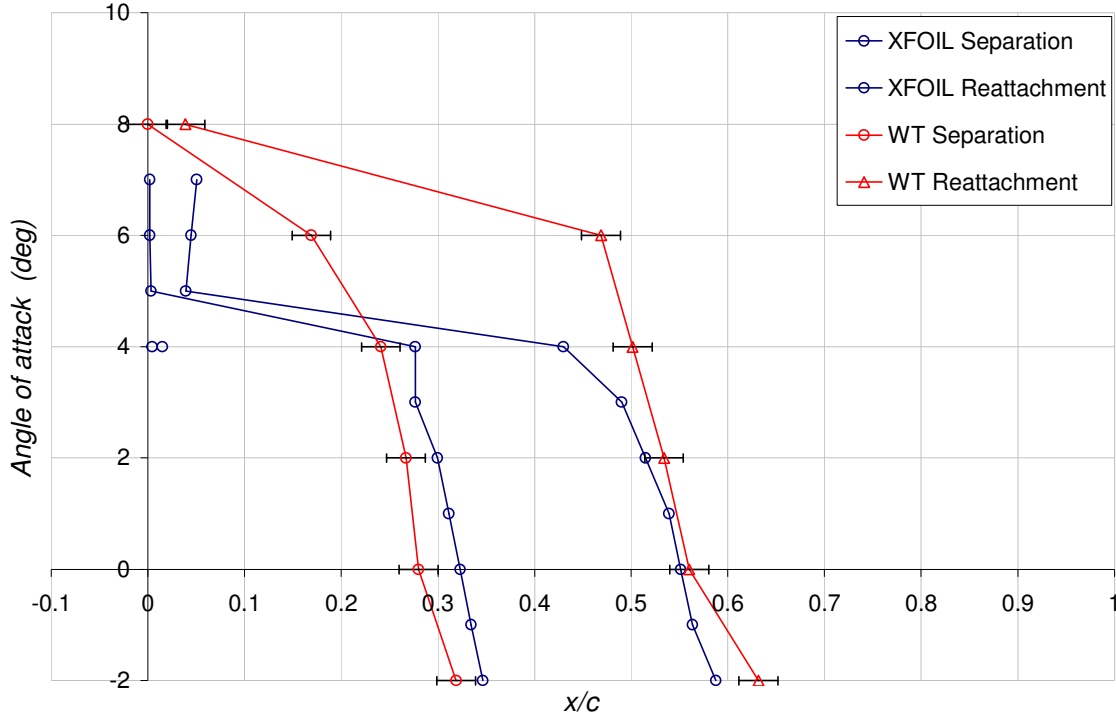
BEZ062518513 Re = 153,000 +/- 25,600
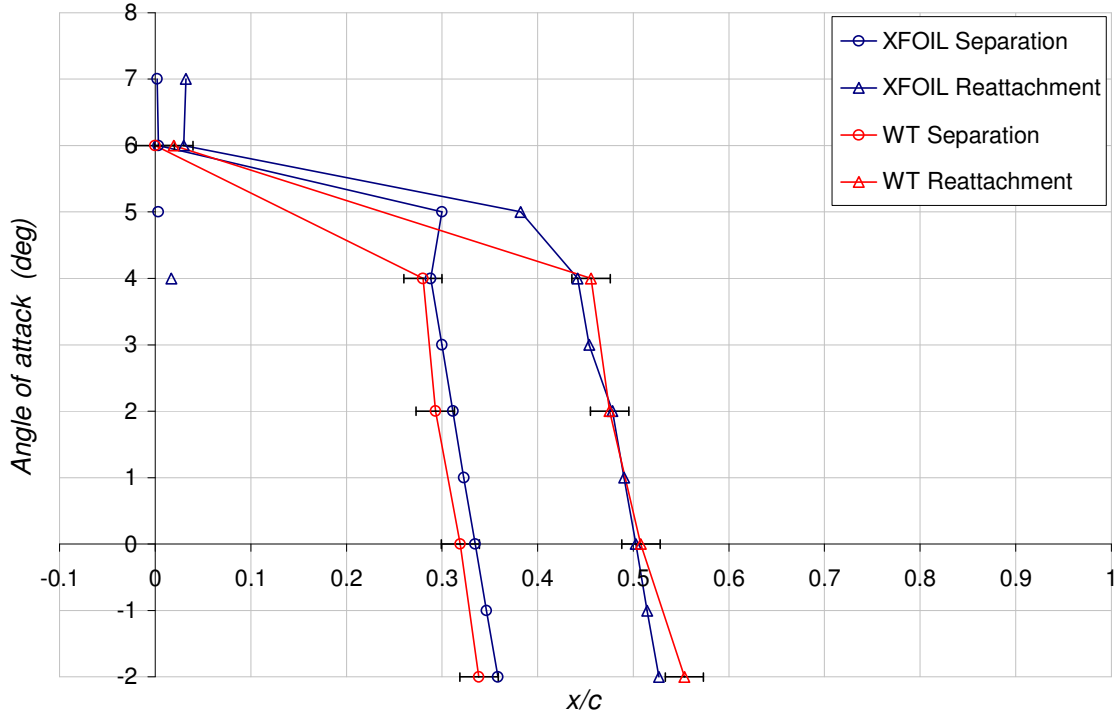
BEZ072018013

BEZ072018013 Re = 100,000 +/- 24,000

- XFOIL Separation
- XFOIL Reattachment
- WT Separation
- WT Reattachment
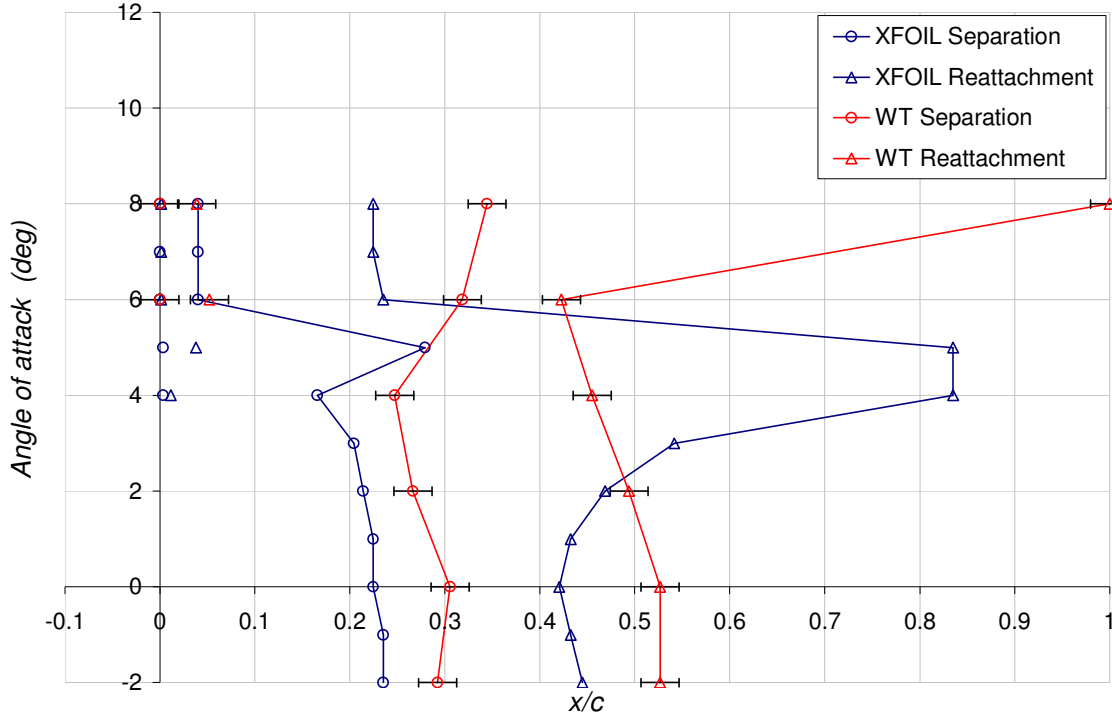
BEZ072018013 Re = 150,000 +/- 27,100

- XFOIL Separation
- XFOIL Reattachment
- WT Separation
- WT Reattachment
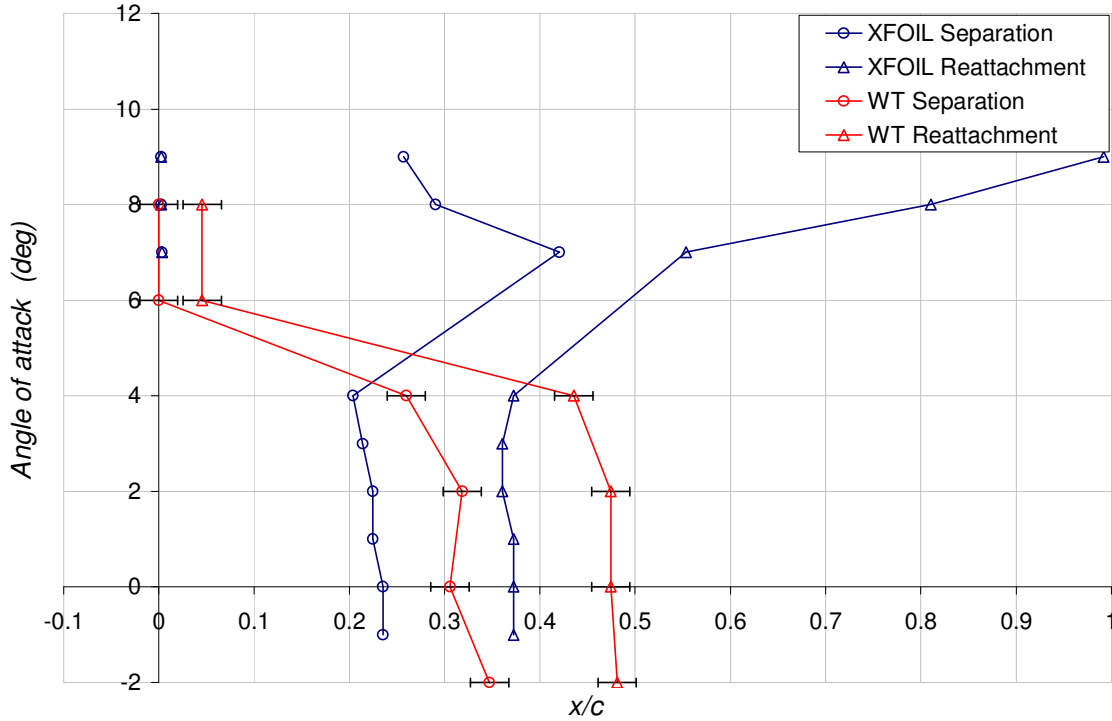
BEZ083018513

BEZ083018513 Re = 103,000 +/- 24,300
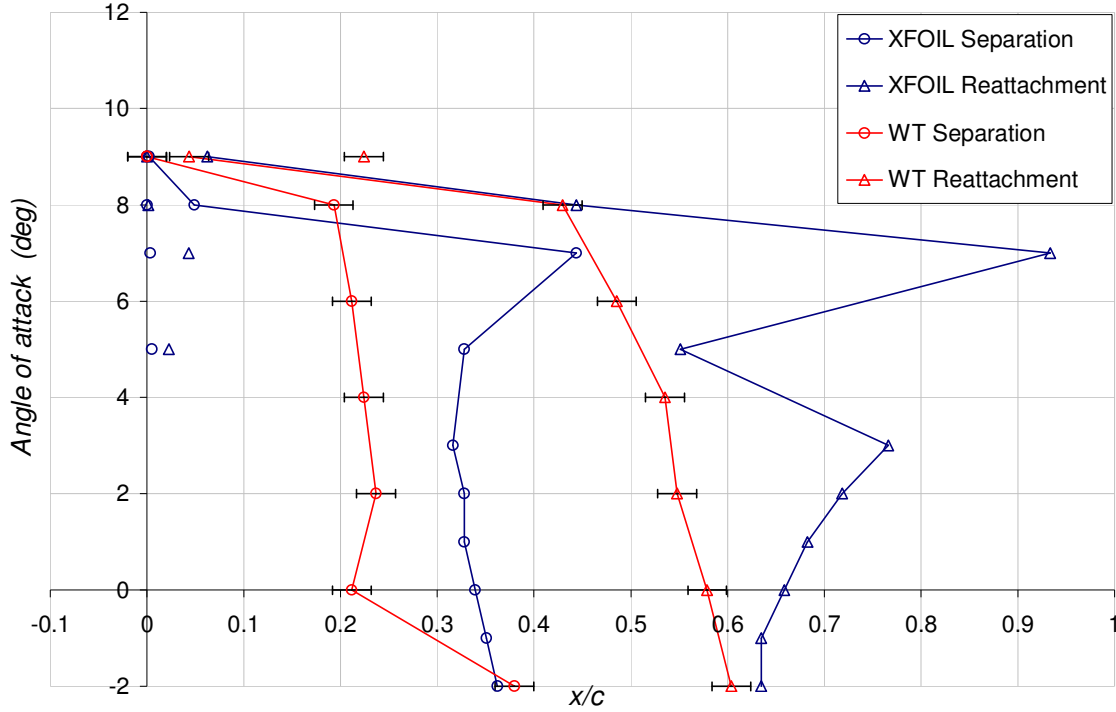
BEZ083018513 Re = 147,000 +/- 25,300

170
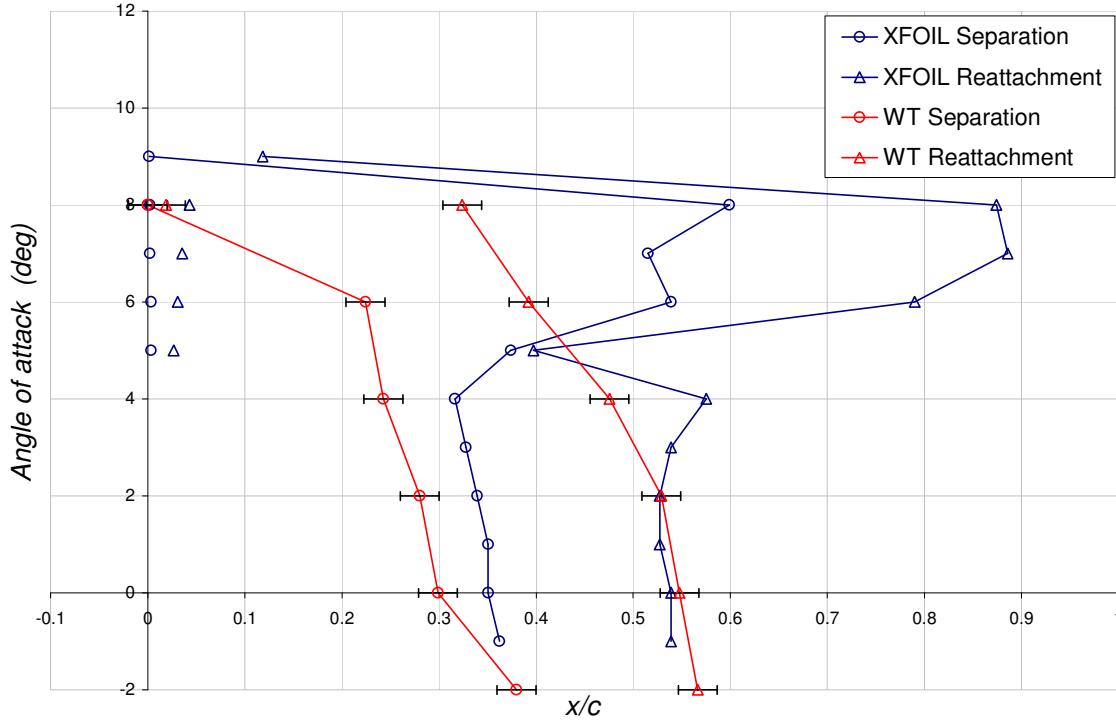
D2. Surface Oil Flow Visualization Photographs

The following sequence of photographs shows the development of the surface oil features during a wind tunnel test of a BEZ062518513 airfoil at Re = 150 and 0° angle of attack. The test duration was 6 minutes.
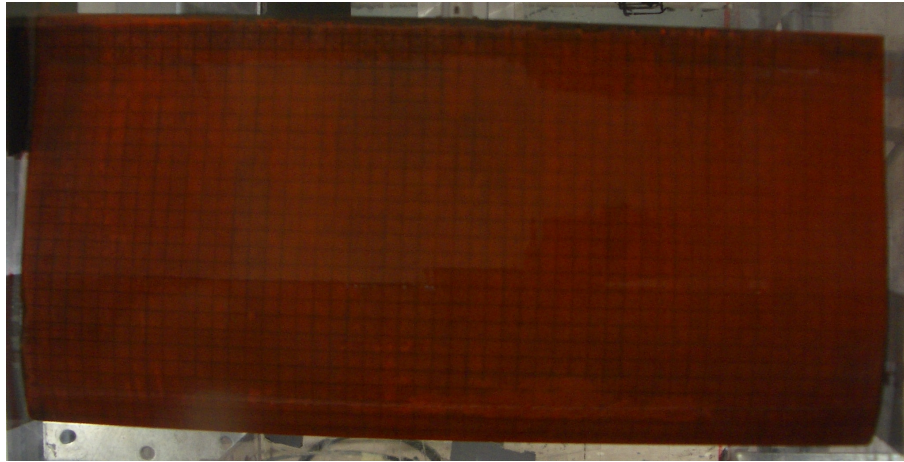
T = 0 min.
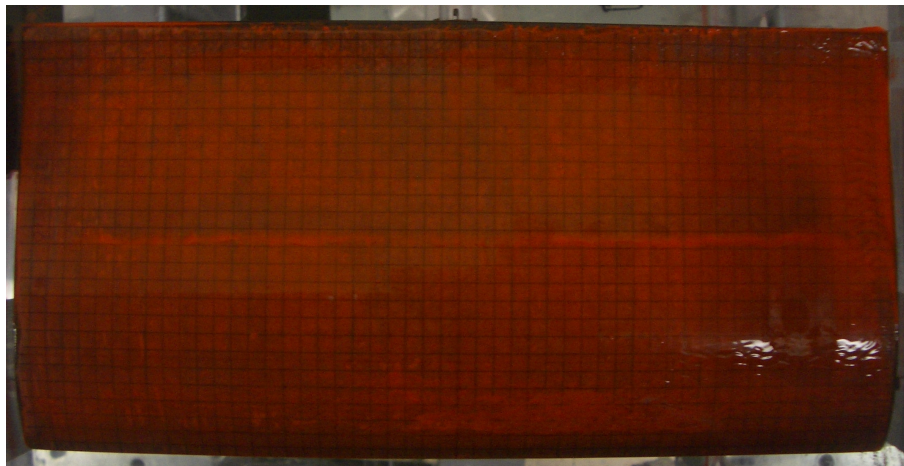
T = 1 min.
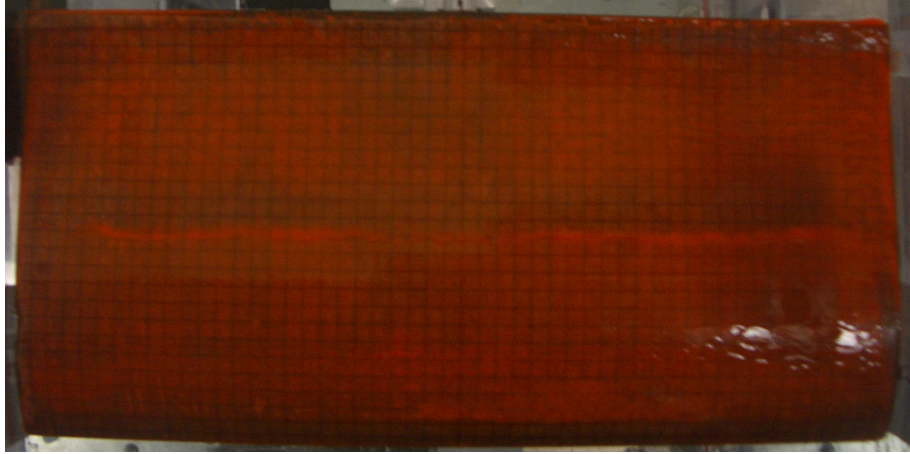
T = 2 min.

T = 3 min.

T = 4 min.

T = 5 min.

T = 6 min